

OTR FILE COPY

Naval Research Laboratory

Washington, DC 20375-5000

2



NRL Memorandum Report 6538

AD-A213 491

Review of Quasi-Optical Gyrotron Development

A.W. FLIFLET, T.A. HARGREAVES*, R.P. FISCHER,
W.M. MANHEIMER AND P. SRANGLE

*Beam Physics Branch
Plasma Physics Division*

**Mission Research Corporation
Newington, VA 22122*

October 18, 1989

2

Approved for public release; distribution unlimited.

89 10 18 052

REPORT DOCUMENTATION PAGE				Form Approved OMB No. 0704-0188	
1a. REPORT SECURITY CLASSIFICATION UNCLASSIFIED			1b. RESTRICTIVE MARKINGS		
2a. SECURITY CLASSIFICATION AUTHORITY			3. DISTRIBUTION / AVAILABILITY OF REPORT Approved for public release; distribution unlimited.		
2b. DECLASSIFICATION / DOWNGRADING SCHEDULE					
4. PERFORMING ORGANIZATION REPORT NUMBER(S) NRL Memorandum Report 6538			5. MONITORING ORGANIZATION REPORT NUMBER(S)		
6a. NAME OF PERFORMING ORGANIZATION Naval Research Laboratory		6b. OFFICE SYMBOL (If applicable) Code 4794		7a. NAME OF MONITORING ORGANIZATION	
6c. ADDRESS (City, State, and ZIP Code) Washington, DC 20375-5000			7b. ADDRESS (City, State, and ZIP Code)		
8a. NAME OF FUNDING / SPONSORING ORGANIZATION Department of Energy		8b. OFFICE SYMBOL (If applicable)		9. PROCUREMENT INSTRUMENT IDENTIFICATION NUMBER	
8c. ADDRESS (City, State, and ZIP Code) Washington, DC 20545			10. SOURCE OF FUNDING NUMBERS		
			PROGRAM ELEMENT NO.	PROJECT NO.	TASK NO.
			WORK UNIT ACCESSION NO. DN780-307		
11. TITLE (Include Security Classification) Review of Quasi-Optical Gyrotron Development					
12. PERSONAL AUTHOR(S) Fliflet, A.W., Hargreaves*, T.A., Fischer, R.P., Manheimer, W.M. and Sprangle, P.					
13a. TYPE OF REPORT Memorandum		13b. TIME COVERED FROM _____ TO _____		14. DATE OF REPORT (Year, Month, Day) 1989 October 18	
				15. PAGE COUNT 96	
16. SUPPLEMENTARY NOTATION *Mission Research Corp., Newington, VA 22122					
17. COSATI CODES			18. SUBJECT TERMS (Continue on reverse if necessary and identify by block number)		
FIELD	GROUP	SUB-GROUP	Quasi-optical gyrotron Gyrotron QOG		
19. ABSTRACT (Continue on reverse if necessary and identify by block number) <p>There is currently a need for megawatt average power sources of 100-600 GHz radiation for electron cyclotron heating of fusion plasmas. One of the leading candidates for such a source, the conventional waveguide cavity gyrotron,⁽¹⁾ has produced impressive output powers and efficiencies at frequencies up to about 300 GHz. However, this gyrotron configuration is limited at high frequencies by high ohmic heating and problems with transverse mode competition due to the highly overmoded configuration, and with beam collection, since the beam must be collected along a section of the output waveguide. The quasi-optical gyrotron (QOG), first proposed in 1980 by Sprangle, Vomvoridis and Manheimer,⁽³⁾ features an open resonator formed by a pair of spherical mirrors instead of a waveguide resonator and has the potential for overcoming each of these limitations. The resonator mirrors can be well removed from the beam-wave interaction region, allowing a large volume for the interaction and low ohmic heating densities at the mirrors. The beam direction is transverse to the resonator so that beam collection is separate from the output waveguide. This</p> <p style="text-align: right;">(Continues)</p>					
20. DISTRIBUTION / AVAILABILITY OF ABSTRACT <input checked="" type="checkbox"/> UNCLASSIFIED / UNLIMITED <input type="checkbox"/> SAME AS RPT. <input type="checkbox"/> DTIC USERS			21. ABSTRACT SECURITY CLASSIFICATION UNCLASSIFIED		
22a. NAME OF RESPONSIBLE INDIVIDUAL Arne W. Fliflet			22b. TELEPHONE (Include Area Code) (202) 767-2469		22c. OFFICE SYMBOL Code 4794

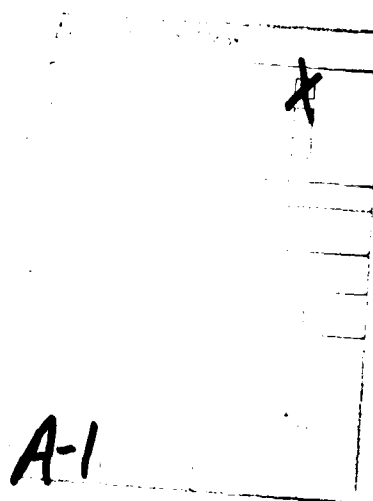
3. DISTRIBUTION/AVAILABILITY OF REPORT

19. ABSTRACT (Continued)

geometry is particularly well suited to the use of a depressed collector for electron beam energy recovery. The QOG operates in the lowest-order transverse (TEM_{001}) Gaussian mode of the resonator, higher-order transverse modes being effectively suppressed by higher diffraction losses. This paper reviews recent progress toward the development of high-power quasi-optical gyrotrons for ECRH of fusion plasmas. It includes an overview of gyrotron theory in terms of normalized variables as they apply to the quasi-optical gyrotron for operation both in the fundamental and the higher harmonics. Scaling equations for the output power and resonator mirror heating by the RF are given. The design tradeoffs between annular and sheet electron beams are discussed as is the issue of beam space-charge depression in the open resonator. Recent advances in the analysis and design of QOG configurations capable of efficient and stable single-mode operation are discussed, showing the possibility of achieving 50% transverse efficiency in highly overmoded resonators. The application of a depressed collector is discussed as a means of recovering the energy in the axial motion of the spent electron beam and, thus, raising the output efficiency to near the transverse electronic efficiency. The problem of high field magnet design is addressed, for both fundamental and higher harmonic operation, the latter being necessary at very high frequencies. The design equations and tradeoffs are applied to the design of 1 MW, CW quasi-optical gyrotrons operating at 120 GHz, in the first and second harmonic at 280 GHz and in the second harmonic at 560 GHz. The output coupling for these 1 MW designs is 5-7% showing the potential for even higher powers per tube if sheet-beam electron guns can be developed. The estimated electronic efficiency of the fundamental harmonic designs is 23%, which leads to an output efficiency of 47% with the use of a depressed collector with a modest collection efficiency. The peak ohmic heating density is 500 kW/cm² in all the designs. This leads to resonator mirror separations ranging from 58 cm for the 120 GHz design, to 116 cm for the 560 GHz, second harmonic design. Finally, a simple output system composed of elliptical and parabolic mirrors is described that converts the output radiation from the resonator into a parallel, quasi-gaussian beam. Experimental programs are reviewed as well, including the recent experiment at the Naval Research Laboratory that produced frequencies ranging from 95-130 GHz and powers up to 150 kW. Operation in a single mode was observed at powers up to 125 kW despite the resonator being highly overmoded. Comparison is made with the theoretically predicted region of single-mode operation. Recent progress in the experimental characterization of QOG resonators is summarized.

CONTENTS

I. INTRODUCTION	1
II. THEORY	6
III. EXPERIMENTAL RESULTS	23
IV. COLD TEST STUDIES	31
V. CURRENT NRL EXPERIMENT	35
VI. 1-MW CW QOG DESIGNS	38
VII. CONCLUSIONS	42
VIII. ACKNOWLEDGEMENTS	45
REFERENCES	46
DISTRIBUTION LIST	83



REVIEW OF QUASI-OPTICAL GYROTRON DEVELOPMENT

I. Introduction

There is currently a need for megawatt average power sources of 100–600 GHz radiation for electron cyclotron heating of fusion plasmas. One of the leading candidates for such a source, the conventional waveguide cavity gyrotron,⁽¹⁾ has produced output powers of 765 kW and efficiencies of 30% at 148 GHz in a CW-relevant configuration.⁽²⁾ As waveguide cavity gyrotrons are driven to higher frequencies and power levels, a number of major obstacles arise. These include, among others, wall heating, mode competition, and collection of the spent electron beam. The quasi-optical gyrotron (QOG) configuration is an attempt to overcome, to varying degrees, many of the limitations generic to conventional gyrotrons.

The QOG was first proposed and analyzed in 1980 by Sprangle, Vomvoridis, and Manheimer⁽³⁾ at the Naval Research Laboratory (NRL). It is a coherent radiation source which has the potential of going to higher frequencies and power levels than conventional closed cavity gyrotrons. The QOG is based on an electron cyclotron interaction as are the gyrotrons and cyclotron autoresonance masers (CARMs), but it utilizes an open Fabry-Perot type resonator instead of a closed cavity configuration.

The basic structure of the quasi-optical gyrotron, shown in Figure 1, consists of an open resonator containing a beam of electrons gyrating about, as well as streaming parallel to, an applied magnetic field. The magnetic field is directed transverse to the axis of the open resonator, which consists of two or more appropriately curved mirrors.

As a coherent radiation source the QOG has a number of very attractive features. These features include:

- i) low voltage operation (~ 100 keV);
- ii) transverse mode selection, which is achieved in an open resonator through diffraction effects;
- iii) low wall heating, which is accomplished by increasing the separation between the resonator mirrors, thus lowering the stored power density;

- iv) high frequency capability and tunability, which are possible since the resonator dimensions are not related to the radiation wavelength;
- v) high efficiency operation ($\sim 50\%$);
- vi) simplified electron beam collection and use of a depressed collector, since the radiation and electron beam propagate at right angles to each other;
- vii) efficient operation at higher cyclotron harmonics;
- viii) low electron beam power density with large beam power ;
- ix) independent variability of the resonator quality factor (Q).

Both the closed cavity gyrotron and the quasi-optical maser have the advantage that they can operate efficiently at low voltages (< 100 keV). Low voltage operation allows for more compact and less expensive power supplies. In addition, x-ray shielding becomes less of a problem at these low voltages and a depressed collector can be used to provide higher overall efficiencies. Since the QOG utilizes an open resonator and thus, can have a large interaction volume, the input electron beam power can be extremely high while the power density can be kept fairly low. The usual limitations on beam power imposed by space charge effects can therefore be substantially eliminated. The wave-particle interaction can be efficient ($\sim 50\%$) similarly to the conventional gyrotron. In addition, the operating frequency is limited solely by the external magnetic field and is independent of the dimensions of any physical structure. Efficient coupling between the electrons and radiation field can occur near harmonics of the relativistic cyclotron frequency allowing harmonic operation. A QOG has many modes which, in principle, can experience gain, producing a multimode output signal. The fundamental transverse Gaussian resonator mode (TEM_{001}) can be preferentially excited in the open resonator. If the mirrors in the open resonator are made large enough to intercept a large fraction of the electromagnetic flux in the fundamental mode, we may expect this mode to have a large Q . The higher order transverse modes can be expected to have substantially smaller Q factors since they suffer from larger diffraction

losses. This is an advantage over a closed cavity, where all transverse modes would have comparable values of Q . Output coupling is via diffraction around the mirrors and can be varied independently of other interaction parameters. The axial mode separation is small compared to the interaction bandwidth in CW-relevant configurations so that a number of longitudinal modes within the resonator can undergo gain and produce a multimode output signal, unless they are suppressed. Longitudinal mode selection can be achieved by nonlinear gain suppression of competing modes by the dominant mode or by employing a mode selective structure in the resonator such as a diffraction grating. The theory of multimode operation was developed by Bondeson, Manheimer and Ott.⁽⁴⁾ The theory of quasi-optical gyrokystrons and of operation at the harmonics of the electron cyclotron frequency has also been examined.^(5,6) New theoretical work shows that single longitudinal mode equilibria are possible and can be efficient.⁽⁷⁾

In this article we present a review of the QOG work performed at the Naval Research Laboratory (NRL), as well as the progress made at other institutions. The theory of the QOG, as well as conventional gyrotrons, can be easily understood in terms of three normalized variables: F , the normalized electric field; μ , the normalized interaction length; and δ , the normalized interaction phase-slip parameter. These parameters can be used to predict regions where the QOG will stably operate in a single mode.⁽⁷⁾ Single-mode operation is important for many applications and might be unexpected in the QOG due to the fact that several (> 10) different longitudinal modes may be excited within the bandwidth of the beam-wave interaction. Significant regions of single-mode operation are found, particularly if the axis of the mirror resonator is tilted by a small amount ($\sim 2^\circ$) from the direction perpendicular to the travel of the electron beam.⁽⁷⁾ Indeed, the peak efficiency region can also be within the region of single-mode stability for some designs. Further, increasing the mode density by moving the resonator mirrors apart (which is done to reduce the peak ohmic heating levels on the mirrors) has little effect on the single-mode stability region of a CW device, with the largest effect occurring at very low currents.

Heating of the resonator mirrors by the RF fields is an important issue for a CW

device. The peak heating density occurs at the center of each mirror and can be reduced to arbitrarily low values by moving the resonator mirrors sufficiently far apart. Moreover, the peak heating density is independent of the output coupling fraction (and therefore the resonator output power), and the total power dissipated on the mirrors actually decreases as the output coupling (and power) increase. Scaling equations for both the output power and the resonator mirror heating have been derived in terms of the normalized parameters, a practice which facilitates the design optimization process. Similar equations have been applied to the design of multi-megawatt QOGs by Tran *et al.*⁽⁸⁾

When the electron beam passes through the QOG resonator, it is necessarily far from any ground reference. In annular beam configurations the beam charge density is relatively high, making space charge depression of the beam in the resonator important. Two methods to overcome this effect are proposed, the first being the application of a longitudinal electrostatic field. Ultimately, an electron gun producing a sheet electron beam is desirable. This type of beam is fundamentally better matched to the QOG due to its low charge density, high total current, and the fact that the electrons can be concentrated near the resonator axis.

Current and past QOG experiments have been limited to approximately 120 GHz, due to the availability of high field magnets with the crossbore necessary for the transversely oriented resonator. Magnets capable of extending operation to 280 GHz are potentially available; however, to reach 560 GHz, harmonic operation is essential. It is well known that the nonlinear efficiency is not seriously degraded by operating at the second harmonic, and again, design equations are presented using the normalized variables.

The first QOG experiment was carried out in 1984 by Hargreaves *et al.*⁽⁹⁾ The results of these initial experiments, as well as work carried out at other laboratories, will be reviewed. More recent experiments at NRL by Fliflet *et al.*^(10,11) have demonstrated reasonably good agreement with the available theories and are discussed in more detail. In particular, single-mode operation at high output power was observed.

The characteristics of the RF output mode are critical if the radiation is to be trans-

ported over the long distances necessary for heating a fusion plasma. To investigate different output coupling methods and to measure various resonator parameters, a cold-test setup has been assembled at NRL. This has allowed the testing of resonator sensitivity to alignment, verification of resonator design codes, and characterization of the output radiation.

Based on what has been learned to date, a new experiment has been designed and assembled at NRL. The design of this pulsed experiment is described in some detail due to its relevance to the design of megawatt CW devices. Point designs for several CW devices with frequencies of 120, 280, and 560 GHz are presented. Both first and second harmonic designs are given for operation at 280 GHz, while the design for 560 GHz assumes operation at the second harmonic. Design limitations and strengths are discussed.

The remainder of this paper is organized as follows. Section 2 presents a summary of QOG theory. Section 3 reviews recent QOG experimental results and Section 4 discusses cold-test studies of QOG resonators. Section 5 discusses the design of a new high power QOG experiment which has been set up at NRL. Section 6 summarizes the prescription for designing CW 120, 280, and 560 GHz QOGs with 1 MW output power and includes point designs. Conclusions are given in Section 7.

II. Theory

II.A. Quasi-Optical Resonator Modes

The quasi-optical gyrotron concept involves the application of optical techniques to gyrotron devices. Specifically, it involves the use of a Fabry-Perot-type open mirror resonator to confine the radiation. The basic configuration is shown in Figure 1. The electron beam propagates perpendicularly to the paper along a magnetic field. The figure shows both the annular beam and double sheet beam cross sectional geometries. The radiation bounces back and forth across the distance d between the mirrors in one or more TEM_{00l} modes of the resonator and interacts with the electron beam via the conventional gyrotron mechanism.⁽¹²⁾ The mode structure of the resonator is determined primarily by the separation, d , and radius of curvature, R_c , of the mirrors. The radiation beam waist radius of the TEM_{00} mode in the Gaussian approximation is given by:

$$w_0 \approx \left(\frac{d\lambda}{2\pi} \right)^{1/2} \left(\frac{1+g}{1-g} \right)^{1/4} \quad (1)$$

where λ is the free-space wavelength of the radiation and $g = 1 - d/R_c$. The parameter regimes corresponding to stable resonator configurations are indicated in Figure 2. Near concentric resonators ($d \approx 2R_c$) have the lowest peak ohmic loading of the mirror surfaces. Radiation is taken out of the resonator by diffraction around the edges of the mirrors. This type of output coupling effectively discriminates against higher order transverse modes of the resonator. In most analyses and experiments to date, the resonator axis has been perpendicular to the electron beam as in Figure 1, i.e., oriented in the y -direction; but recent theoretical work by Antonsen, Levush and Manheimer⁽⁷⁾ indicates that the efficiency and the stability of single-mode operation may be enhanced by tilting the resonator axis by a small angle $\theta \sim 2^\circ$ with respect to the y -axis. The theory of the QOG with an oblique angle between the resonator and electron beam axes has also been considered by Levush et al.,⁽⁶⁾ Kreischer et al.,⁽¹³⁾ and Wang et al.⁽¹⁴⁾ In the configuration shown in Fig. 1, a moderate voltage ($V \sim 100$ kV) gyrating electron beam will interact primarily with the x -component

of the resonator RF electric field. The resonator fields are periodic with a period $t_b = 2d/c$ where c is the speed of light. The RF electric field excited in the resonator by the electron beam can be expressed as a superposition of TEM_{00l} modes of the form:

$$E_x(y, z, t) = \frac{1}{2} e^{-x^2/w_0^2} \sum_l E_l(t) \cos[k(y - \theta z) - l\pi/2] e^{-i\omega_l t} + \text{c.c.} \quad (2)$$

where k is the wave number, E_l is a complex mode amplitude, and

$$\omega_l = \omega_0 + \pi(l - l_0)c/d \quad (3)$$

is the cold resonator mode frequency where ω_0 is the frequency of an arbitrary reference mode with index l_0 . The number of modes included in the summation should be sufficient to span the interaction bandwidth

$$\Delta\omega_{\text{int}} \approx \omega/(sN_c) \quad (4)$$

where N_c is the number of cyclotron orbits occurring during the interaction, ω is the wave angular frequency, and s is the harmonic number of the interaction. In configurations with low mirror ohmic heating densities the mode frequency separation $\Delta\omega_l = \pi c/d \ll \Delta\omega_{\text{int}}$. Since the interaction involves only a few radiation wavelengths, the mode dependence of the wave number can be neglected.

II.B. Slow-Time-Scale Equations of Motion

The linear and nonlinear theory of quasi-optical and waveguide gyrotrons has received considerable attention.^(3,4,5,15) The use of normalized variables to reduce the gyrotron equations of motion to equations for the transverse momentum involving a small number of parameters has proven extremely useful for gyrotron design optimization. The slow-time-scale equations of motion (averaged with respect to the cyclotron period) for the interaction with a single resonator mode, and perpendicular electron beam and mirror axes, are known as the pendulum equations and are given by:

$$\frac{dp_{\perp}}{d\zeta} = -F_s \cos(ky_g - s\pi/2) e^{-(2\zeta/\mu)^2} p_{\perp}^{s-1} \sin \vartheta \quad (5)$$

$$\frac{d\vartheta}{d\zeta} = -(\Delta + p_{\perp}^2 - 1) - sF_s \cos(ky_g - s\pi/2) e^{-(2\zeta/\mu)^2} p_{\perp}^{s-2} \cos \vartheta \quad (6)$$

where $p_{\perp} = \gamma\beta_{\perp}/\gamma_0\beta_{\perp 0}$ is the normalized transverse momentum and ϑ is the slow-time-scale phase. The (initial) relativistic mass factor is denoted by γ (γ_0), β_{\perp} ($\beta_{\perp 0}$) is the transverse velocity normalized to c , and y_g is the guiding center of the electron gyration. The independent variable is the normalized axial coordinate:

$$\zeta = \frac{\pi\beta_{\perp 0}^2 z}{\beta_{\parallel 0} \lambda} \quad (7)$$

where $\beta_{\parallel 0}$ is the axial velocity normalized to c . The pendulum equations are characterized by the normalized wave amplitude F_s , the interaction length μ , and the detuning parameter Δ . As shown by Tran et al.⁽¹⁶⁾, for the QOG these parameters can be expressed as follows (in MKS units):

$$F_s = \frac{E_c \beta_{\perp 0}^{s-4} s^{s-1}}{B_0 c 2^{s-1} s!} \quad (8)$$

$$\mu = 2\pi \frac{\beta_{\perp 0}^2 w_0}{\beta_{\parallel 0} \lambda} \quad (9)$$

$$\Delta = \frac{2}{\beta_{\perp 0}^2} \left(1 - \frac{s\Omega/\gamma_0}{\omega} \right) \quad (10)$$

where E_c is the RF electric field at the beam, B_0 is the applied axial magnetic field, and Ω is the (nonrelativistic) electron gyrofrequency. The transverse electron efficiency is obtained by integration of the pendulum equations averaged over the initial phase angle (ϑ_0) and orbit guiding centers (y_g) of the electrons and is given by:

$$\eta_{\perp} = 1 - \left\langle p_{\perp}^2 (\zeta_{out}, \vartheta_0) \right\rangle_{\vartheta_0, y_g} \quad (11)$$

neglecting velocity spread, a good approximation for the gyrotron. The transverse efficiency is related to the interaction's electronic efficiency (η) according to:

$$\eta = \beta_{\perp 0}^2 \eta_{\perp} / \left[2 \left(1 - \gamma_0^{-1} \right) \right]. \quad (12)$$

In gyrotrons with a sparse enough spectrum of interacting modes that only one mode falls within the interaction bandwidth, the detuning parameter can be chosen to optimize the transverse efficiency of the interaction. The efficiency potential of gyrotrons of this type can be expressed in terms of F - μ plots⁽¹⁷⁾ in which the contours of constant transverse

efficiency (η_{\perp}) are plotted as a function of the normalized wave amplitude and interaction length for optimized resonance detuning. The maximum transverse efficiency obtained in this manner is over 60% for a pencil beam, $\mu = 10-20$ and $F = 0.8-1.6$. In gyrotrons with a high density of interacting modes such as the QOG, operation at optimum detuning may be prevented by mode competition. In this case operation may be single or multimoded and the frequency and detuning are determined by the start-up conditions and the interaction itself.

II.C. Oscillation Threshold Current

The starting current for oscillations, an important parameter in QOG design, can be obtained from a small signal analysis of the pendulum equations. The resulting expression for perpendicular radiation and electron beam axes (using MKS units) is:

$$I_{st} = \frac{2\pi^4 m_e c}{\mu_0 e} \frac{\gamma \beta_{\perp}^{2(3-s)}}{Q} \frac{d}{\lambda} \left(\frac{w_0}{\lambda} \right)^2 \left(\frac{2^{s-1} s!}{s^s} \right)^2 \frac{2}{1 \pm J_0(2kr_b)} \hat{I}_{st}(s, \Delta, \mu) \quad (13)$$

where m_e and e are the mass and charge (magnitude) of an electron, μ_0 is the free space permeability, Q is the resonator quality factor, and J_0 is a regular Bessel function. The normalized threshold current \hat{I} is given by⁽¹⁶⁾

$$\hat{I}_{st}(s, \Delta, \mu) = \frac{8}{\pi \mu^2} \frac{e^{\delta^2/2}}{\mu \delta - 2s} \quad (14)$$

where $\delta = \mu \Delta / 2$ is the kinematic phase-slip angle of the electrons transiting the resonator. The factor $2 / (1 \pm J_0(2kr_b))$ in Equation (13) accounts for the annular beam geometry⁽¹⁸⁾ and is omitted for a pencil beam. The $+$ ($-$) sign corresponds to placing the electron beam axis on a maximum (null) of the wave field. In a high mode density resonator, the first mode to achieve large amplitude oscillations will be the mode with a detuning corresponding to the highest linear growth rate or, equivalently, the lowest oscillation threshold current, which is given by: $\hat{I}_{st}^{\min} = \hat{I}_{st}(s, \Delta_{\min}, \mu)$ where $\Delta_{\min} = 2\delta_0/\mu$ and $\delta_0 = s/\mu + \sqrt{s^2/\mu^2 + 1}$.

II.D. Single-mode Efficiency and Stability

The single-mode stability and efficiency potential of the QOG has recently been investigated by Antonsen et al.⁽⁷⁾ and an outline of their formulation is included here. For a given interaction length μ , the single-mode efficiency can be expressed as a function of RF electric field parameter, $\epsilon = F_s \mu$, and the kinematic phase-slip parameter, $\delta = \mu \Delta/2$, which for the fundamental harmonic interaction are also given by:

$$\delta = \frac{2\pi}{\beta_{\parallel}} \left(1 - \frac{\Omega}{\omega \gamma_0} \right) \frac{w_0}{\lambda} \quad (15)$$

$$\epsilon = \frac{8\pi}{B_0 \lambda} \frac{(1 + \alpha^2)}{(1 - \gamma^{-2}) \alpha} \sqrt{\frac{Z_0 P}{\pi c^2 T}}, \quad (16)$$

where P is the diffraction output power, $Z_0 = 377$ ohms, T is the resonator output coupling coefficient, and $\alpha = v_{\perp 0}/v_{\parallel 0}$ is the initial beam velocity (or momentum) pitch ratio. Consider first the case of an idealized pencil beam and a normalized interaction length $\mu = 10$. A contour plot of η_{\perp} in $\epsilon - \delta$ space calculated by Antonsen et al.⁽⁷⁾ is shown in Figure 3. A peak transverse efficiency of ~ 0.6 is obtained at a normalized field amplitude of $\epsilon = 1.6$ and a phase-slip parameter of $\delta = 2.8$. This corresponds, for example, to an electronic efficiency of 30% for a beam with pitch ratio $\alpha = 1$. Contours of constant normalized threshold current, $\chi = I/I_{st}^{\min}$ are also shown. Optimum efficiency is obtained for currents of 8–12 times the minimum threshold current. The linear gain is maximum for $\delta \sim 1.1$ which corresponds to a lower efficiency of $\eta_{\perp} \sim 0.3$ for $\chi = 8$. The mode frequency separation in high average power quasi-optical gyrotrons is such that $\Delta\delta = \delta_{l+1} - \delta_l \leq 0.5$. Thus, it is necessary to determine whether an efficient single-mode equilibrium is stable and accessible. Antonsen et al. find that the stability of single-mode equilibria depends primarily on the stability of the nearest neighbor mode pairs in the presence of the desired operating mode. Coupling occurs between these modes via the resonance condition: $|2\omega_l - \omega_{l+1} - \omega_{l-1}| \approx 0$. The region of stable operation corresponds to the area enclosed by the heavy solid curve in Figure 3. The stable region includes both the high-efficiency regime and the high-gain regime. The high-efficiency regime can be accessed during CW operation, in principle, by suitably programming the start-up conditions of the gyrotron.

The stable region denoted by the heavy solid line corresponds to an axial mode density characterized by the ratio $\xi = t_b/t_t = 10$, where t_t is the electron transit time in the resonator. The heavy dashed line shows the effect of increasing the mode density by a factor of 5. Thus, the boundary of the high efficiency region is insensitive to the mode density.

II.E. Effect of Annular Electron Beam

The effect of replacing the pencil beam by an annular electron beam — used in all QOG experiments to date — is shown in Figure 4. The figure shows results from Antonsen et al.⁽⁷⁾ and indicates a reduction in the peak transverse efficiency from ~ 0.6 to ~ 0.4 as well as a significant reduction in the region of stable single-mode equilibria. The reduction in peak efficiency associated with an annular beam is well known, but the effect on single-mode stability has only recently been appreciated. As pointed out by Antonsen et al., the neighboring modes are less effectively suppressed by the main mode in the annular beam case. This is because, unlike the pencil beam case, the neighboring modes have opposite parity to the main mode and weaker coupling to the beam due to the shift in the position of the field maxima of these modes. This leads to higher starting currents for the satellite modes, but gain can occur at the currents needed for high nonlinear efficiency of the main mode. Since the electrons which contribute most to the gain of the satellite modes pass through a null of the main mode, the effectiveness of the nonlinear gain suppression mechanism is reduced. The reduction in the stable region further reduces the maximum single-mode efficiency to $\eta_{\perp} \sim 0.3$ and limits the maximum stable current to about $4I_{st}^{\min}$. Interestingly, the work of Antonsen et al. shows that both the stable region and the efficiency can be increased by tilting the mirror axis relative to the axis of the magnetic field by a small angle from the usual perpendicular orientation. An angle of $\theta \approx 2^\circ$ is sufficient to equalize the coupling to even and odd parity modes. The resulting plot of single-mode efficiency and the stable region as calculated by Antonsen et al. are shown in Figure 5. The calculations correspond to a normalized tilt angle $\theta' = kw_0\theta = 1$. The stable

region is similar in extent to the pencil beam case and the peak transverse efficiency is over 50%. The theory also predicts that the size of the stable region is relatively unaffected by increased mode density in the case of CW operation.

II.F. Output Power and Ohmic Heating Scaling

The output power of the quasi-optical gyrotron scales as:⁽¹⁹⁾

$$P_{\text{out}} (\text{W}) = \frac{\pi m_e^2 c^4}{16 Z_0 e^2} \gamma_0^2 \beta_{\parallel 0}^2 \beta_{\perp 0}^{4-2s} \mu^2 F_s^2 T \left(\frac{2^{s-1} s!}{s^s} \right)^2 \quad (17)$$

in MKS units, where T is the resonator total output coupling. Choosing μ and F_s to optimize efficiency and single-mode stability specifies T for given output power and beam parameters. Typical parameters for efficient, stable operation are $\mu = 10$ and $F = 0.2$.

The peak ohmic heating density on the resonator mirrors may be expressed in the form:

$$\rho_{\text{peak}} (\text{W/m}^2) = \frac{1}{16\sqrt{2}} \left(\frac{c}{Z_0} \right)^{\frac{1}{2}} \left(\frac{m_e}{e} \right)^2 \sigma^{-1/2} \omega^{5/2} \gamma_0^2 \beta_{\perp 0}^{4-2s} (1+g) F_s^2 \left(\frac{2^{s-1} s!}{s^s} \right)^2 \quad (18)$$

where σ is the mirror conductivity which is taken to be 3.6×10^7 siemens/m for OFHC copper at 200°C. For a given frequency, F_s , beam parameters, and output coupling, mirror heating depends on g . The peak ohmic heating density occurs at the center of the mirror and is related to the average heating density according to (for symmetric cavities): $\rho_{\text{peak}} = \ln(2/T) \rho_{\text{av}}$, which shows that the difference between the peak and average heating can be minimized by maximizing the mirror output coupling. As shown in Figure 2 the parameter g can vary from 1 (planar mirrors) to -1 (concentric mirrors) at which point the resonator becomes unstable. As the frequency is increased, peak and average ohmic heating densities can be controlled by choosing g close enough to -1. Since the radiation beam waist is determined by optimum interaction length, the mirror separation increases as g approaches -1. Thus the price for reduced ohmic heating density is increased axial mode density and increased sensitivity of the the resonator modes to mirror alignment. However, the total ohmic power dissipated by each resonator mirror is independent of g :

$$P_{\text{ohmic}} (\text{W}) = \frac{\pi}{16} \left(\frac{c^7}{2Z_0^3} \right)^{\frac{1}{2}} \left(\frac{m_e}{e} \right)^2 \left(\frac{\omega}{\sigma} \right)^{\frac{1}{2}} \gamma^2 \beta_{\parallel 0}^2 \beta_{\perp 0}^{4-2s} F_s^2 \mu^2 (1 - T/2) \left(\frac{2^{s-1} s!}{s^s} \right)^2 \quad (19)$$

This power is a sensitive function of the harmonic number for constant beam and RF parameters. For a given frequency and electron beam parameters, a constraint on average heating density leads to a trade-off between g and T . Note that for a given output power and μ , F_s is also determined by T .

II.G. Superconducting Magnet Design

The fact that the QOG resonator is transverse to the path of the electron beam forces the superconducting magnet to have an open crossbore and effectively requires a "cold-bore" configuration. The crossbore limits the magnet to a Helmholtz-type design. Separating the two magnet coils further than the one diameter separation of a true Helmholtz pair (to allow more room for the resonator) produces a local minimum in the magnetic field in the interaction region. This minimum has two effects. First, the electron beam must pass through the peak magnetic field before it reaches the resonator, and it is at this peak where the beam will have its greatest chance of being magnetically mirrored. Thus, by the time the beam reaches the resonator, some of its perpendicular energy has been converted back into energy parallel to the magnetic field and is unavailable to the RF interaction. Second, some of the electrons will enter the interaction region with phases such that they gain a net amount of energy from the RF fields in the resonator. This energy gained is deposited as perpendicular energy in the electron. This occurs in all gyrotrons, however, here the electron beam must again pass through a second maximum of the magnetic field. If the electron has gained a sufficient amount of transverse energy, it will be magnetically mirrored and return to the electron beam-resonator interaction region. Thus, it is possible to build up a volume of space charge near the interaction region which would affect both the interaction and the propagation of the electron beam itself. Therefore, it is desirable to minimize the separation of the magnet coils.

The minimum necessary diameter of the crossbore is set by the envelope of the radiation of the TEM₀₀ mode in the resonator. The fields in this mode are Gaussian and fall to $1/e$

of their axial value in a distance

$$w(y) = \left[\frac{\pi^2 w_0^4 + \lambda^2 y^2}{\pi^2 w_0^2} \right]^{1/2} \quad (20)$$

where y is the distance from the axis of the magnetic field. To ensure that the crossbore structure does not interfere with the radiation, it should have an inner diameter of $\sim 6w(y)$.

A similar restriction may be placed on the axial bore, which must be large enough to allow the electron beam to pass from the electron gun through the interaction region and into the collector. The variation of the electron beam guiding center radius ($r_e(z)$) with position along the magnetic axis is given for a cylindrical MIG-type electron gun by

$$r_e(z) \approx r_c \left[\frac{B_c}{B(z)} \right]^{1/2} \quad (21)$$

where $B(z)$ is the magnetic field at position z along the magnetic field axis, r_c is the cathode radius, and B_c is the cathode magnetic field. The width of a sheet beam would vary linearly with magnetic field in a configuration with planar geometry. It is evident from these equations that both the axial bore and the crossbore may be tapered, with their diameters increasing with distance from the interaction region.

To maximize the space available in the crossbore, a cold-bore magnet in which the electron beam shares a common vacuum enclosure with the superconducting magnet dewar is necessary. This prevents the implementation of the usual CW gyrotron assembly procedure of sealing and conditioning the electron gun and microwave circuit prior to insertion in the magnet bore. Instead, critical components such as the gun, collector, and mirrors must be baked-out prior to assembly to the system. This procedure has been successfully used in high average power RF-accelerators but requires considerable care since clean surfaces are critical for CW operation. An advantage of the cold-bore magnet configuration is that the cold surfaces of the dewar act as a powerful vacuum pump; however, further work is needed on assembly and conditioning techniques for ultra-clean cold-bore systems. The dissipation of small amounts of RF power which may leak into the magnet bore is another area of concern because the inner surfaces of the bore are inherently thermally isolated. One approach is to insert a piece of RF absorber into the bore to act as a load using the

same principle as a microwave oven. Since the walls of the bore are cold and have a good surface finish, they are highly reflective and will direct most of the RF power leaking into the bore to the absorber.

II.H. Harmonic Operation

As the operating frequency (and thus the magnetic field) of the gyrotron is raised, magnet design becomes more difficult and eventually impossible. At this point operation of the resonator at a harmonic of the fundamental is desirable. Presently, magnets allowing operation in the fundamental mode are potentially available for frequencies up to ~ 280 GHz, but frequencies approaching 560 GHz will necessarily involve devices operating in at least the second harmonic.

Harmonic operation of cavity and quasi-optical gyrotrons has been studied by several investigators^(6,17,19) who have found that, in general, the efficiency of operation at the second harmonic can approach that of the fundamental. The problem that must be overcome is the suppression of the fundamental mode while allowing the second harmonic fields to grow to the large amplitudes necessary for efficient operation. The easiest method available is simply to take advantage of the optical characteristics of the resonator modes which have a waist radius dependent on the radiation wavelength as shown in Eq. (1). Assuming a particular mirror configuration and a purely Gaussian mode at the resonator mirrors, the output couplings of harmonics m and n are related by:

$$T_m = T_n^{m/n} \quad (22)$$

and the normalized interaction lengths are related by:

$$\frac{\mu_m}{\mu_n} = \sqrt{\frac{m}{n}}. \quad (23)$$

These relationships favor the harmonic interactions but they are compensated by the fact that the harmonic interactions become increasingly weaker with increasing harmonic number (for weakly relativistic electron beams). The ratio of minimum starting currents for

different harmonic interactions in a resonator is given within an accuracy of about 20% by:

$$\frac{I_{st}^{(n)}}{I_{st}^{(m)}} = \beta_{10}^{-2(n-m)} T_1^{n-m} \sqrt{\frac{m}{n}} \left[2^{n-m} \frac{m^m n!}{n^n m!} \right]^2. \quad (24)$$

As an example, consider a QOG with an 80 kV, $\alpha = 1.5$ electron beam and $T_1 = 10\%$ diffractive output coupling for the fundamental harmonic interaction. Then, from Eq. (22) the output coupling for the second harmonic is $T_2 = 1\%$, and $I_{st}^{(1)}/I_{st}^{(2)} = 2.5$, i.e., the starting current for the fundamental harmonic is a factor of two higher than that of the second harmonic interaction. Thus, harmonic operation appears feasible at currents near the oscillation threshold, but additional means of suppressing oscillation in the fundamental mode may be needed for high-efficiency harmonic operation since this requires currents many times higher than the threshold current. One possibility is to replace one of the mirrors by a grating designed to reflect only the harmonic frequency of interest. Operation in the gyrokystron mode through the addition of a prebunching resonator may also stabilize operation in the second harmonic. This scheme may utilize either an injected external signal or a portion of the output radiation that has been filtered to pass only the desired frequency.

II.I. Space-charge Effects

In the QOG the electron beam experiences space-charge effects in the drift-tube between the gun and the resonator and in the open region between the end of the beam drift-tube and the collector. An estimate for the space-charge limited current for an annular beam in the drift-tube is^(20,21,8)

$$I_{max} [A] = 1.71 \times 10^4 \frac{\gamma_0 \left[1 - (1 - \beta_{10}^2)^{1/3} \right]^{3/2}}{G(r_e, R_d, \Delta_e)} \quad (25)$$

where the geometrical factor G is given by:

$$G = \frac{3\Delta_e}{4r_e} + 2 \ln \left(\frac{R_d/r_e}{1 + \Delta_e/r_e} \right) \quad (26)$$

and depends on the beam radius r_e and thickness Δ_e , and the drift-tube wall radius R_d . The space-charge depression of the beam voltage in the drift-tube for currents less than

I_{\max} is given by^(20,21):

$$\Delta V_{sc} [V] = 30 \frac{I}{\beta_{||0}} G(r_e, R_d, \Delta_e). \quad (27)$$

For a thin annular beam with an energy of 80 keV, $\alpha = 1.5$, and $r_e = 0.75 R_d$; $I_{\max} = 149$ A. This is several times the current needed for a megawatt device. The voltage depression when the current is 50 A is $\Delta V_{sc} = 3$ kV. Thus, propagation of an annular beam in the drift tube does not appear to be a problem for a MW device but is an issue for multi-megawatt power levels.

Space-charge effects are also an issue for beam propagation across the open resonator. An accurate calculation of space-charge depression of the beam in the region between the drift-tube and the collector involves two-dimensional effects, but a simple estimate for the space-charge effects in this region can be obtained from the above equations by replacing the drift-tube wall radius in Eqs. (25) and (27) by half the separation between the drift-tube and the collector. Although this choice is somewhat arbitrary, and should be considered a temporary replacement for more accurate calculations, the result depends only logarithmically on the separation. In addition, this estimate has been used successfully to interpret experimental results as discussed in Section 3.3. The collector and drift-tube are separated by 5 cm and the beam radius is 0.6 cm in the current NRL experiment at 120 GHz. The drift-tube-collector separation corresponds to two radiation waist diameters. Cold tests have shown that at this separation the presence of the beam guiding structures has no measurable effect on the resonator Q . This configuration leads to a space-charge-limited current in the resonator of ~ 30 A for an 80 kV beam with $\alpha = 1.5$ and 65 A for a beam with $\alpha = 1$. It is clear that space charge limits the propagation of high α annular beams in the resonator. An approach to neutralizing space-charge effects in the resonator involving the application of a positive DC potential between the drift-tube and the collector tip is under investigation at NRL (see Section V.).

II.J. Depressed Collector

The space-charge limitation on the propagation of electron beams with high values of α in the QOG resonator results in a reduction of the electronic efficiency obtainable at high beam powers, as can be seen from Eq. (12). However, the beam energy that is transferred to the radiation is extracted mainly from the electron motion perpendicular to the magnetic field, while the presence of the space charge affects the electron motion parallel to the magnetic field. Since the parallel energy of the electrons is relatively unaffected by the beam-wave interaction, it may be reclaimed by biasing the collector to a depressed voltage. Indeed, as the electrons travel into the collector, the magnetic field decreases, resulting in most of the electron's residual perpendicular energy being converted into parallel energy (via adiabatic decompression), yielding more energy available for recovery by a depressed collector. Thus, the output efficiency may be increased by at least the initial ratio of parallel to perpendicular energy of the beam. For example, the output efficiency could be double the electronic efficiency by simply recovering the parallel energy in an $\alpha = 1$ beam.

Depressed collectors have been proposed for use in gyrotrons and gyroklystrons.⁽²²⁾ The QOG is ideally suited to the incorporation of a depressed collector due to the natural separation of the electron beam from the RF system. Application of a depressed collector to a conventional gyrotron, on the other hand, must first address the difficult problem of separating the radiation from the electron beam without excessive losses and while maintaining high output RF mode purity.

II.K. Sheet Beam Electron Gun

To date, all QOG experiments have utilized the annular electron beams produced by MIG-type guns. Methods used to design these electron guns are well developed and understood, due in part to the problem being two-dimensional. Annular beams are not ideally suited to the QOG; however, the QOG is relatively insensitive to many of the electron beam parameters. The QOG is, of course, sensitive to the perpendicular momentum of the electrons, since that is where the RF energy is mainly derived, but it is not very sensitive

to spreads in the parallel momentum of the electrons due to the fact that the RF fields propagate in a direction normal to the direction of electron beam propagation.

Since the QOG electron beam-RF wave interaction is averaged over more than a half wavelength of the standing wave pattern in the resonator, the interaction is necessarily insensitive to the electron beam thickness and diameter, provided the diameter is somewhat smaller than the radiation beam waist diameter. This is a fundamental limitation on the use of annular beams in the QOG since the radiation waist diameter is effectively proportional to the wavelength of the radiation. However, the diameter of an annular beam has been shown⁽²³⁾ to scale as the cube root of the wavelength. Thus, it becomes progressively more difficult to keep the electron beam diameter small compared to the radiation waist as the operating frequency is increased. Space-charge effects associated with propagation in the open resonator place a second limitation on the use of annular beams in high-power, high-frequency devices, as described in Section II.I.

The solution to these limitations is to use a sheet electron beam. Such a beam can overcome the space charge problem by spreading the current over a length of the resonator axis much larger than the radiation waist. This is possible since the Rayleigh length is large in the QOG's designed for low mirror loading. The cross section of a double sheet beam is shown in Figure 1. The double sheet beam appears advantageous because of its reflection symmetry with respect to the $y - z$ plane, strong correlation with the cylindrical MIG-type gun, and its effective doubling of the total current for a given transverse dimension. Design tradeoff equations for planar MIG-type guns showing the feasibility of generating a sheet electron beam for the QOG have been developed by Manheimer et al.⁽²³⁾ The design of sheet beam electron guns for the QOG has also been investigated by Read et al.⁽²⁴⁾

The major drawback to the development of a sheet electron beam has been that the problem is inherently three-dimensional. The design approach which has been adopted at NRL⁽²³⁾ involves analyzing the beam in two-dimensional planar geometry and then correcting for edge effects. This allows a prescription to be developed for obtaining a laminar flow beam - a desirable property for minimizing beam velocity spread - based on a planar

MIG-type gun geometry. The basic configuration of the gun is shown in Figure 6. The gun is symmetric with respect to the gun axis in the figure. Good approximations to the electrode shapes needed to obtain a laminar flow beam are obtained by the electrode synthesis approach.⁽²³⁾ Two types of synthesized electrodes can be used. The main electrodes which control the flow of the body of the beam are synthesized for a planar, relativistic, temperature-limited flow beam.^(23,25) This type of synthesis is analogous to the electrode synthesis approach for cylindrical MIG guns.^(26,27) The design of these electrodes can be refined using the Herrmannsfeldt Electron Trajectory Code.⁽²⁸⁾

The synthesis method can also be used to design electrodes which compensate for beam edge effects.⁽²³⁾ Near the beam there is an electric field in the y -direction due to space charge. This field causes an $\vec{E} \times \vec{B}$ drift in the x -direction for electrons near the beam edge. The beam edge with positive y will drift up and the beam edge with negative y will drift down, so the beam edges will tend to curl in opposite directions as the beam propagates. The synthesis method solves for the positions and potentials of focusing electrodes near the beam edge. These electrodes insure that the electrons near the edge of the beam see the same fields as for an infinitely extended beam.

Magnet design is more complicated for a sheet beam gun than for cylindrical guns. The main superconducting coils at the crossbore are circular and produce a roughly uniform field in the beam intersection region of the crossbore, and can be viewed as having either planar or cylindrical symmetry. The fringe fields have cylindrical symmetry, however, the beam compression region is assumed to have planar symmetry. This means a complicated three-dimensional design for the trim magnets in order to compensate as much as possible for the fringe fields of the main magnet. Fortunately, computer codes which can be used to design arbitrary 3-D magnet systems have been developed and are available.⁽²⁹⁾

II.L. Output Coupling Schemes

Efficient transportation of the output radiation of an RF source is important for most applications and is essential for plasma heating due to the large path length between the

source and the plasma. At the frequencies of interest, this transportation is most often accomplished via a quasi-optical transport system. The QOG is naturally matched to such a system, requiring only that the radiation be extracted from the vacuum of the resonator in the event that a windowless design is undesirable. To take advantage of the frequency tunability of the QOG, this requires a wide bandwidth ($\pm 20\%$) window design. Short pulse experiments at NRL⁽¹⁰⁾ have utilized thin ($t \leq 0.1\lambda$) mylar windows, but it is unclear how well the window will withstand the stresses of CW operation. However, the output radiation of the QOG is naturally expanding as it emerges from the resonator, so that the power density at the window could (at least in principle) be reduced to very low values.

A conceptual design of an output coupling scheme that converts the QOG output into a hollow, parallel beam is shown in Figure 7. For reflectors located at distances greater than the Rayleigh length

$$z_0 = \frac{1}{2} (d(2R_c - d))^{1/2} \quad (28)$$

from the resonator waist, the radiation appears to have originated from a point source at the center of the radiation waist, and ray optics may be used to analyze the reflected waves. This approach clearly ignores diffraction effects which should be included in a more exact analysis, but does aid in understanding the basic design. Thus, the output coupling structure of Figure 7 may be understood as follows. The radiation that is diffracted out of the resonator is incident upon an elliptical reflector that has one focus at the center of the resonator (the point source of the output radiation), and the other focus somewhere outside the vacuum window. The radiation is reflected by the elliptical mirror through the vacuum window and focused outside the vacuum. This focus is also a focus of the second reflector which has a parabolic shape. Therefore, the rays now emerging from the focus of the parabolic reflector are reflected to form a parallel beam.

Several points are worth noting in this design. First, RF power density at the vacuum window may be reduced simply by expanding the diameter of the elliptical reflector. Second, the parallel beam emerging from the parabolic reflector will be hollow in the ray optic limit, but diffraction effects may be expected to fill in the beam as shown schematically in the

figure. Also, since the total output from one mirror is focused to a point outside the vacuum, steps may be necessary to prevent breakdown of the atmosphere there. Finally, this design is presented here as an example; several other designs are possible and may be better suited for a given situation.

III. Experimental Results

The QOG is currently under investigation by several different groups. The first QOG experiment was carried out in 1984 by Hargreaves et al.⁽⁹⁾ at NRL and used a resonator with a 4-cm mirror separation. Consistent with the relatively low axial mode density of this resonator, single-mode operation was observed at powers up to 80 kW at a frequency of 110 GHz and an efficiency of 11%. The first experiment with large mirror separation (81 cm) was also conducted at NRL in 1986 by Read et al.⁽³⁰⁾ and achieved an output power of 50 kW at a frequency of 115 GHz and an efficiency of 7%. Alternate resonator configurations have been proposed and analyzed by Zhonghai, Shenggang and Kongyi of the People's Republic of China,^(31,32) and an experimental study of different output structures has been performed by Morse and Pyle.⁽³³⁾ Itoh et al. have utilized yet another resonator design to produce 20 kW of RF power at an efficiency of 16% and a frequency of 120 GHz.⁽³⁴⁾ This experiment utilized a relatively low-power electron beam ($V = 30$ kV, $I = 3.5$ A). Experiments similar to those described here are being performed by Tran et al.⁽³⁵⁾ With limited experimental time, powers and efficiencies as high as 85 kW and 10% have been observed from a resonator with a mirror separation of 34 cm.

A consequence of the use of a spherical mirror resonator with diffraction output coupling is that the output coupling can be a sensitive function of the mirror separation while the gyrotron interaction length, which depends on the radiation beam waist, remains approximately constant. This feature has been exploited for the first time in a recent experiment at NRL⁽¹⁰⁾ by using mirror holders which are adjustable over a wide range. The ability to vary the separation of the resonator mirrors from 20 to 28 cm allowed the resonator output coupling to be optimized with respect to the electron beam power. It also permitted new tests of the gyrotron scaling theory. The coupling of the annular electron beam to the standing-wave radiation in the resonator could be varied by translating the resonator transversely to the electron beam. Finally, precise mirror alignment - needed for optimum resonator Q - was easily maintained.

This section presents results from a thorough and extensive experimental study of the

first QOG to operate at powers over 100 kW using a CW-relevant resonator. The QOG was tunable from 95–130 GHz and operated at powers up to 148 kW and output efficiencies up to 12%. The peak electronic efficiency is estimated to be $16 \pm 2\%$. The main effect responsible for the difference between the output and electronic efficiency is ohmic heating of the mirrors which can be a significant fraction of the total output at low output coupling. This effect becomes small at MW output power levels due to larger output coupling. Single-mode operation was observed at powers up to 125 kW. Conditions for single-mode operation in the highly overmoded system have been characterized and compared with theoretical predictions. Efficiency optimization by variation of output coupling and by tapering the magnetic field have been demonstrated. These results point the way to the realization of megawatt level devices with output efficiencies of $\sim 20\%$.

A schematic diagram of the experiment is shown in Figure 8. The gyrating electron beam is generated by the MIG-type electron gun at the bottom of the superconducting magnet and propagates up through the drift-tube and resonator before being absorbed in the collector. The microwave fields interact with the electron beam between the collector and drift-tube where electrostatic space charge depression can affect the beam electrons' energy. The microwave power diffracted around each mirror is collected as output and propagated through thin (0.013 cm thick) mylar windows out of the vacuum. These windows are essentially transparent over the frequency range of the experiment. The parameters of the experiment are presented in Table I.

III.A. Multimode Power and Efficiency Measurements

Output power measurements were carried out as a function of beam current and mirror separation. A preliminary investigation of output power and efficiency showed that for currents less than 8 A, output power was a decreasing function of mirror separation. Power measurements for a gun voltage of 66.7 kV and a current of 8 A at three mirror separations are shown by the solid square data points in Figure 9. Consequently, initial power and efficiency measurements were taken at the minimum mirror separation of 20 cm. This

minimizes the output coupling and so leads to the optimum saturated efficiency at the lowest current where beam quality should be highest. Mirror alignment and translation were optimized by minimizing the threshold current for a magnetic field of 50 kG and a beam voltage of 66.7 kV. A minimum threshold current of 0.25 A at a frequency of 125.8 GHz was obtained. For these conditions the calculated total resonator Q factor is 215,000, and the theoretical minimum threshold current for $\alpha = 1.5$ is 0.10 A, less than half the measured value. This discrepancy suggests that the experimental resonator Q factor may be $\sim 80,000$, however, the calculated minimum threshold current depends on α which is not well characterized in the experiment. Using the Q value inferred from the threshold measurement and the theoretical ohmic Q leads to an estimate of the diffraction Q of 96,000. The calculated diffraction Q is 395,000.

The output power was obtained by multiplying the calorimeter power measurement by two, dividing by the repetition rate and the pulse width, and correcting for the absorption efficiency of the calorimeter. The radiation pulse width was found (to a good approximation) to be equal to the beam voltage flat-top pulse width of 13 μsec under most conditions, and this pulse width was used in the peak power calculation. The power output through the two windows was checked and found to be equal within measurement accuracy. The calorimeter absorptivity was measured to be 94% at 120 GHz and to decrease with decreasing frequency to $\sim 60\%$ at 90 GHz.

The output power as a function of beam current is shown in Figure 10 for magnetic fields of 44, 47 and 50 kG and a constant gun voltage of 71.5 kV. A calorimeter efficiency of 95% was used in the output power computations for the magnetic fields of 47 and 50 kG, and an efficiency of 88% was used for the 44 kG results. The corresponding output efficiency is shown in Figure 11. The observed maximum output efficiencies for these magnetic fields and conditions was 12% at 50 kG, 11.9% at 47 kG, and 11% at 44 kG. In obtaining this data no attempt was made to promote single-mode operation and, consequently, operation was generally multimoded. Typical multimode frequency spectra are shown in Figures 12(a)-(c). The spectra correspond to magnetic fields of 44, 47 and 50 kG, respectively, and a

gun voltage of 71.5 kV. The beam current in Figures 12(a) and (c) is 8 A and is 14 A in Figure 12(b).

To obtain the electronic efficiency for a given output efficiency it is necessary to correct for ohmic heating losses according to

$$\eta_{el} = (1 + Q_d/Q_o)\eta_{out} \quad (29)$$

where η_{el} and η_{out} are the electronic and output efficiencies, and Q_d and Q_o are the diffraction and ohmic quality factors.

As discussed above, the ratio Q_d/Q_o depends sensitively on the diffraction Q factor, which has not been directly measured. For operation at 50 kG, $Q_d/Q_o = 0.2$ based on Q_d inferred from the threshold current measurement, whereas $Q_d/Q_o = 0.84$ based on Q_d calculated using scalar diffraction theory. The corresponding electronic efficiencies are plotted as functions of IQ/d in Figure 13. Using the value of Q_d inferred from the threshold current measurement leads to a maximum electronic efficiency of 14%; using the value of Q_d calculated with scalar diffraction theory leads to a maximum electronic efficiency of 21%. The figure also shows theoretical results based on a nonlinear, multimode simulation⁽⁴⁾ using parameters corresponding to the 50 kG data and assuming $\alpha = 1$. These calculations yield a maximum efficiency of 17.7%. The theoretical optimum value of $QI/d \approx 2.0 \times 10^6$ is in good agreement with the experimental results based on the Q factor inferred from the threshold current measurement but not with the results obtained using the theoretical Q factor.

The electronic efficiency was not corrected for the space-charge depression of the beam voltage, because the free energy for the interaction is associated mainly with the transverse momentum of the electrons which is not greatly affected by the presence of space-charge. However, space-charge does limit the maximum beam power which can be propagated in the resonator and reduces the achievable velocity pitch ratio.

As shown in Figure 11, for a magnetic field of 50 kG and a mirror separation of 20 cm, the output efficiency decreases as the current is increased beyond 6 A. This effect of over-driving the resonator is well known from cavity gyrotrons. Increased power and efficiency

at currents above 6 A can be obtained in the QOG by increasing the output coupling by increasing the mirror separation until the optimum RF field amplitude is re-established in the resonator. This effect is illustrated by the solid data in Figure 9 which shows output power optimization by variation of the mirror separation for a constant beam current of 13.5 A and a constant gun voltage of 71.5 kV.

The output power and efficiency as a function of beam current for a magnetic field of 50 kG, gun voltage in the range 71–75 kV, and beam currents up to 24 A are shown in Figure 14. Operation was generally multimoded with 4–6 modes being excited. The frequency of the strongest modes was ~ 125 GHz. The data indicated by the squares corresponds to the minimum mirror separation of 20 cm and a gun voltage of 71.5 kV. The calculated diffractive output coupling at this separation is 0.4% for 125 GHz radiation. The data indicated by the triangles and dots corresponds to a mirror separation of 23 cm and a calculated 0.8% diffraction output coupling. The highest measured power, shown by the solid dots, was 148 kW and was obtained at a mirror separation of 23 cm, a beam voltage and current of 78 kV and 24 A, and a negative taper in the magnetic field of 2% across the interaction region. This current is estimated to be near the space-charge limit for this voltage and $\alpha = 1$. No evidence of oscillation in higher order transverse modes was observed from the frequency measurements at 50 kG or other magnetic fields.

III.B. Frequency Tuning Measurements

In the QOG the operating frequency is approximately Ω/γ , the relativistic electron cyclotron frequency, so that the operating frequency can be tuned by varying either the magnetic field or the gun voltage. Figure 15 presents frequency and power measurements for magnetic fields from 38 to 50 kG with fixed gun voltage (66.7 kV) and current (~ 12 A). Operation was usually multimoded as indicated in the figure which shows frequency variation from 95 to 130 GHz. Significantly, the power varied by < 3 dB for this frequency variation. The QOG could have operated at still lower frequencies (at lower magnetic fields), but such frequencies were below the cutoff frequency of the waveguide used in the

heterodyne frequency diagnostic.

Frequency variation with electron gun voltage was also investigated. Frequency measurements were obtained at several voltages between 43 and 72 kV for a magnetic field of 50 kG and a current of ~ 10 A. As shown in Figure 16, a 4% frequency increase was measured for this variation in gun voltage. A disadvantage of this method of frequency tuning is that the power scales strongly with voltage and decreased from 70 to 25 kW as the voltage was decreased.

III.C. Studies of Near-Single-Mode Operation

Since the longitudinal mode density of the QOG resonator is high, it might be expected that the device is inherently multimoded, but this is not the case. The operating parameter space was characterized by regions of stable, single-mode or near-single-mode operation. Single-mode operation was most common at lower output powers but was also observed at powers up to 125 kW. At a current near threshold, the single mode having the highest growth rate can be excited. It was found that if the current was then increased, holding the magnetic field and gun voltage fixed, the resonator would oscillate in a sequence of higher frequency modes as shown in Figure 17. The data plotted in this figure was obtained for a gun voltage of 71.5 kV, a mirror separation of 23 cm, and a magnetic field of 47 kG in the middle of the interaction region. The magnetic field had a negative 2% taper across the interaction region. Alternatively, it was possible to vary the voltage while increasing the current (keeping the magnetic field fixed) so as to maintain single-mode operation in the mode initially excited. Figure 18 shows a region of single-mode operation in $V-I$ space obtained using the latter procedure. An untapered magnetic field of 47 kG was used to obtain this data at an operating frequency of 119 GHz. The area of single-mode operation is denoted approximately by the line thickness; voltage changes of ~ 0.5 kV led to observable changes in the mode spectrum. The maximum power of the data in this figure is 55 kW. Figure 19 shows the output power obtained during single-mode or near-single-mode operation for mirror separations of 23, 25.5 and 28 cm. The magnetic field was

47 kG and the oscillation frequency was 119–120 GHz in all cases. Here, output powers as high as 125 kW were obtained while maintaining nearly-single-mode operation. At least 90% of the output power was in a single mode with most of the remaining power in the two adjacent modes. Relative mode power was measured using the amplitude response of the heterodyne frequency diagnostic.

As the current was increased above threshold, it was found that single-mode operation corresponded to progressively higher resonance frequency mismatches $(\omega - \Omega_c/\gamma)$. Figure 20(a) shows frequency mismatch uncorrected for the space-charge effect versus the beam current normalized to the oscillation threshold current for the data shown in Figure 19. Figure 20(b) shows the frequency mismatch obtained by correcting the electron cyclotron frequency for space-charge depression of the beam as discussed in Section II.I.

To compare the theoretically predicted stable, single-mode operating regime⁽⁷⁾ with the experimental data, it is convenient to express the data in terms of the normalized RF electric field amplitude, ϵ , and the kinematic phase-slip parameter for the interaction, δ defined in Eqs. (15) and (16). An advantage of these new parameters is their relative insensitivity to α , which is not well determined in the experiment. Theoretically, the stable operating regime for a fixed μ corresponds to an area in ϵ - δ space. Uncertainty in the beam velocity pitch ratio α leads to a range of possible μ values from 5–10. The region of stable single-mode operation predicted by theory corresponds to the area bounded by the solid curves in Figures 21(a) and (b) which were obtained assuming $\alpha = 0.65$ ($\mu = 5$) and $\alpha = 1$ ($\mu = 10$), respectively. These plots were made for an annular beam of radius 1.6 mm centered on the electric field maximum of the equilibrium mode. Equilibria with values of ϵ , δ outside the stable region are unstable with respect to the growth of neighboring modes (sidebands). The use of an annular beam configuration has an important effect on the size and shape of the stability boundary.⁽⁷⁾ In particular, the stable region for an annular beam is much smaller than that for a pencil beam. This reduction occurs because, unlike the pencil beam, an annular beam couples to both the odd and even symmetry modes of the resonator. If beam-RF coupling is optimized for the desired operating mode, coupling

to the two adjacent modes, which have opposite symmetry, will be weaker. The weaker coupling of the principal competing modes inhibits saturation of their gain by the main mode, an important factor in determining the region of stable operation. Comparison of the Figures 21(a) and (b) shows that the predicted stable area is smaller for $\mu = 10$ than for $\mu = 5$. The reduction in stable region with increase in μ is a general feature of the theory for both pencil and annular beams. The experimental single-mode data for mirror separations of 23, 25.5 and 28 cm, assuming either $\alpha = 0.65$ or 1, is also shown in Figures 21(a) and (b). The data indicates single-mode operation occurs for $\epsilon \leq 2$. This is consistent with the theoretical results for $\mu = 5$ but not $\mu = 10$. However, nonlinear, time dependent, multimode simulations for $\mu = 10$ show that the unstable sidebands saturate at a sufficiently low level that the resulting equilibrium appears single-moded within the resolution of the experimental data (90% of power in main mode). Thus, the theoretical results regarding single-mode operation are not inconsistent with a value of $\mu = 10$ ($\alpha = 1$) in the experiment. The experimental data is primarily limited to the lower halves of the stable regions, whereas theory predicts that all points should be accessible. Simulations modeling the finite rise time of the voltage pulse indicate that this is not a factor which limits the accessible region. The inability to tune the gyrotron within the stable region without loss of single-modedness is not understood, but may be related to the 4% ripple of the voltage pulse which corresponds to a variation in the detuning parameter δ .

The measured electronic efficiency corrected for ohmic effects is compared in Figures 22(a) and (b) with the theoretical annular beam single-mode efficiency for $\mu = 5$ and 10 and using the measured detuning. The agreement is much better for $\mu = 5$ than 10. The calculated efficiency for $\mu = 10$ is about 60% greater than the measured efficiency. In addition, the calculated efficiency peaks at a value of ϵ lower than that suggested by the data. The calculated efficiency for $\mu = 5$ ($\alpha = 0.65$) is in better agreement with the data both in maximum value and dependence on ϵ .

IV. Cold Test Studies

The quality factor of a resonator relates the energy stored in a resonator to the resonator's various losses. The Q for a Fabry-Perot-type resonator can be very large, with quality factors on the order of 100,000 being typical for resonators used in recent experiments at NRL. Since the balance between ohmic effects and diffraction is very important in the QOG, detailed experimental studies have been performed at NRL.⁽³⁶⁾

Fabry-Perot resonators have been used for several years to measure the microwave properties of solids, liquids, and gasses.⁽³⁷⁾ For permittivity and loss measurements, the design goal is to make the Q as large as possible. This is accomplished by making the resonator mirror diameters large so that diffraction losses are negligible. Energy is typically coupled into the resonator through coupling holes in one of the mirrors or by means of a dielectric beam splitter.

Meaningful, nonperturbing cold tests of gyrotron cavities are difficult to perform in practice. Most cold-test schemes involve drilling coupling holes into the resonator walls,⁽³⁸⁾ which may perturb the resonator mode severely. It is also often difficult to couple efficiently to the mode of interest, which is frequently a high-order mode. Woskoboinikow et al.⁽³⁹⁾ utilized a nonperturbing method in which they radiated their conventional gyrotron cavities in the far field and analyzed the reflected signal. This technique also has the advantage of being nondestructive to the gyrotron cavity, allowing cold testing of the identical cavity used in the hot test. It is difficult to test a QOG resonator with this technique due to the small amount of energy that is coupled into the desired resonator mode.

In the QOG the resonator operates in the fundamental Gaussian mode making coupling to the correct mode relatively easy. The NRL experiments used the method of Perrenoud et al.⁽⁴⁰⁾ where a small hole through the center of one of the resonator mirrors was used to couple energy into the resonator, with part of the power diffracted around the outside edge of the mirror being collected by a standard gain horn as output. This technique has the advantage that there is little background radiation to affect the measurement, increasing its accuracy. Extensive measurements were made of the variation of resonator Q with

separation. Several cavities were studied, and good agreement was obtained between the measured values and calculations based on scalar diffraction theory. The effect of slightly misaligning the resonator mirrors was also examined.

IV.A. Quasi-Optical Resonators

The Q of a Fabry-Perot-type resonator can be written

$$Q = \frac{4\pi d}{\lambda T} \quad (30)$$

where T is the fractional round-trip loss. In practice, this loss factor includes losses due to ohmic and diffraction effects as well as losses due to any coupling holes. All three of these loss mechanisms are important for the cavities examined in this study. The total Q of the resonator can be expressed as

$$\frac{1}{Q} = \frac{1}{Q_o} + \frac{1}{Q_{d,c}} \quad (31)$$

where Q_o is the ohmic Q and $Q_{d,c}$ is the Q due to diffraction and coupling losses. The ohmic Q may be calculated using the formula

$$Q_o = \frac{d}{2}(f\pi\mu_0\sigma)^{\frac{1}{2}}. \quad (32)$$

Silver- and gold-coated resonator mirrors were used in these tests, with conductivities 6.15×10^7 and 4.5×10^7 siemens/m, respectively. Note that the ohmic Q increases linearly with separation due to the fact that the energy stored in the resonator increases linearly with mirror separation.

The diffraction/coupling Q is best calculated (separately from the ohmic Q) through the use of a computer code based on a scalar Huygen's formulation.⁽⁴¹⁾ This code may be used to model cavities with nonidentical mirrors, with or without coupling holes. The diffraction and coupling Q factors are each calculated for the TEM₀₀ mode as well as higher order modes and may then be combined with the ohmic Q ; yielding the total calculated resonator Q .

A chief obstacle to performing cold tests of millimeter-wave resonators is coupling power into the resonator without perturbing the Q too seriously. In this study, a small coupling

hole was drilled through the center of one mirror. The size of the hole was chosen to minimize degradation of Q while coupling a measurable amount of power into the resonator. The radius of the coupling hole used here was 0.38 mm, which had the effect shown in Figure 23. As can be seen from the figure, for separations greater than 20 cm, the added coupling hole (not present in the hot test resonator) had essentially no effect. The resonator mirror separation in the hot test could be varied between 20 and 28 cm, making this cold test resonator a good model of the experiment. For mirror separations less than 20 cm, any change in the round-trip losses results in a large change in the total Q due to the small output coupling. Figure 24 shows the calculated round-trip transmission loss due to diffraction as a function of separation for the resonator analyzed in Figure 23. The transmission increases from 2.5% to 6% in the range of interest.

IV.B. Cold Test Results

A schematic diagram of the experimental setup is shown in Figure 25 and is similar to that adopted by Perenoud et al.⁽⁴⁰⁾ The entire arrangement was located on an optical table, with the QOG resonator mirrors mounted on six-inch diameter optical mounts translatable by hand. Instrument calibration was accomplished using the interferometer shown in Figure 25, which was comprised of two six-inch diameter mirrors and had a Q of approximately 70,000.

Figure 26 shows measured and calculated values of Q versus separation for a resonator with 4.5-cm diameter mirrors. The coupling hole was 0.76 mm in diameter and the frequency was 120 GHz. The radius of curvature was 38.7 cm for each of the mirrors used. Agreement between data and theory is quite good for separations greater than 20 cm, which is the region of operation of the QOG. Measured values are somewhat higher than predicted by the code at smaller mirror separations, a discrepancy which may be due to the presence of the coupling hole.

Figure 27 shows data obtained with the 4.5-cm diameter mirrors measured at 94 GHz. The values for Q are much lower due to increased diffraction losses at the lower frequency.

A Q of 7,000 corresponds to a round-trip transmission coefficient of 18%, measured at a resonator mirror separation of 26 cm.

Several different resonator configurations were studied in the cold tests performed at NRL⁽³⁶⁾ including asymmetric and misaligned cavities. In general, it was found that the alignment precision available on the hot test was sufficient to easily maximize the resonator Q . The Q values measured in the cold tests were estimated to be accurate to $\pm 10\%$.

V. Current NRL Experiment

Based on results obtained from the experiment described in Section 3, a new QOG experiment designed to produce 500 kW - 1 MW at a frequency of 120 GHz has been assembled at NRL and is shown schematically in Figure 28. The major differences from the experiment shown schematically in Figure 8 are the physically larger, higher current electron gun and a resonator with correspondingly larger output coupling. To accommodate the higher power gun, which also produces a larger diameter electron beam, several of the components of the experiment have been upgraded.

The electron gun used in this experiment is the Varian VUW-8144 which was originally designed for and used in the MIT gyrotron program.⁽²⁾ It produces an annular beam which has a diameter of 1 cm in the resonator. This electron gun is expected to produce a beam with a momentum pitch ratio (α) approaching 1.5, which should allow operation at efficiencies approaching 20%. The gun is capable of operation at voltages in excess of 90 kV which is the limit of the driving modulator. Currents up to 50 A are possible, although this may be limited by space-charge depression of the beam as it passes through the resonator, as discussed in Section II.I. Provision has been made to allow the application of an accelerating electric field across the resonator to offset the space-charge depression, and its effect will be tested experimentally. The approach involves applying a voltage of ~ 10 kV to the collector tip via a high voltage vacuum feedthrough as indicated in Figure 28. In the absence of the accelerating axial electrostatic field, electron currents up to ~ 30 A for $\alpha = 1.5$ and ~ 65 A for $\alpha = 1$ can be propagated.

The electron gun's emitter is placed in the fringing field of the superconducting magnet at a position calculated to produce an average beam momentum pitch ratio (α) of 1.5. This value may be tuned by varying the voltage on the gun's intermediate anode, which is a somewhat tedious task in the current experimental setup. Additional tuning of the electron beam parameters may be gained by adding a trim coil to modify the magnetic field in the region of the emitter and is planned for a later stage of the experiment.

As added protection of the electron gun from vacuum failure of the RF output windows,

a double-window design has been implemented in this experiment. As shown schematically in Figure 28, each window is composed of two layers of 0.013-cm thick mylar with the region between the two layers filled with an inert gas at low pressure. Interlocks are attached that turn the experiment off in the event that the pressure between the two mylar layers changes appreciably. This window design also has the desirable feature of being essentially transparent over the frequency range of interest in the experiment (i.e. 90–130 GHz).

Due to the larger diameter electron beam produced, the beam transport system used in the previous experiment was necessarily replaced. This included the drift-tube as well as the uptaper that transports the beam from the resonator to the collector. Each of these components now has several holes or slots designed both to load any gyrotron modes that might exist in the transport system and to allow better vacuum pumping. The electron beam is now collected above the superconducting magnet dewar, allowing easy access to the collector for cooling. To ensure that the beam is transported to the collector before impinging on the wall of the transport system, a trim coil has been added at the top of the superconducting magnet dewar. The collector is also isolated electrically and thermally, permitting it to be easily modified for depressed operation in future experiments. The thermal isolation enables the collector surface to be baked-out at temperatures up to 400° C after assembly. This has led to a noticeable reduction in the pressure build-up due to collector outgassing during initial operation compared to previous experiments.

To maintain efficient beam-wave coupling in the presence of larger currents, the resonator has been redesigned with correspondingly larger output coupling values. Still maintained is the ability to vary the mirror separation and effectively alter the output coupling while the system is under vacuum. The resonator design parameters are shown in Table II, showing that the output coupling can be varied from 2.2–6.0% by changing the resonator mirror separation from 20–28 cm. This resonator has been extensively studied, both numerically and in cold test, as described in Section IV. The calculated round-trip output coupling of the resonator is plotted as a function of mirror separation in Figure 24. Calculated and measured resonator Q factors for frequencies of 120 and 94 GHz are shown in

Figures 26 and 27 respectively.

VI. 1-MW CW QOG Designs

It is a relatively straightforward task to design high average power QOGs using the equations developed in Section II. The starting point is the specification of the desired output power and operating frequency, the electron beam voltage and velocity pitch ratio (α), and the peak ohmic heating density on the resonator mirrors. The normalized interaction length (μ) and electric field (F) are then chosen from the stability plots (Figure 5) to ensure single-mode, high-efficiency operation. With these parameters specified, the radiation waist radius (w_0), transmission coefficient (T), resonator mirror radius of curvature (R_c) and separation (d) may each be calculated. The resonator mirror diameter ($2a$) (which determines the output coupling) is then best calculated using a resonator code based on scalar diffraction theory,⁽⁴¹⁾ but is estimated here by assuming that the resonator fields are purely Gaussian:

$$a = w_0 \left(\frac{2 \ln(2/T)}{1 + g} \right)^{\frac{1}{2}}. \quad (33)$$

Also easily calculated is the total power (P_{ohmic}) absorbed by each resonator mirror through ohmic heating. If the resonator designed in this manner is compatible with a magnet design, the process is completed.

The value of μ depends both on the electron beam α and the radiation waist radius w_0 . Large values of α (≈ 1.5 – 2) are necessary for high electronic efficiencies and for $\mu = 10$ the corresponding radiation waist radius is $w_0 = 2.5\lambda$. Such a small radiation waist in the interaction region causes the radiation to expand rapidly as it travels away from the interaction region, as can be seen from Eq. (20) which shows that, for $y \gg w_0$, $w(y) \sim \lambda y / (\pi w_0)$. A reasonable estimate for the minimum crossbore radius is three radiation waist radii. This estimate is plotted in Figure 29 for 120 and 280 GHz configurations with $w_0/\lambda = 4.5$ and for 280 GHz with $w_0/\lambda = 2.5$. Note that the radiation waist is approximately independent of λ for $y \gg w_0$. Also shown in this figure is the position of the superconducting coil of the NRL 5 T magnet. This field is large enough to allow operation in the second harmonic at frequencies up to 240 GHz. It is probable that operation in

the fundamental harmonic at 280 GHz will necessitate the use of a magnet whose coils are somewhat closer together. Figure 29 shows that the crossbore radius for $w_0/\lambda = 2.5$ extends into the region occupied by the coils in the NRL magnet, resulting in a conflict between the magnet dewar and the radiation fields. One method to ease the problem is to allow the electron beam α to be lowered to a value of 1. To maintain $\mu = 10$, needed for high perpendicular efficiency and single-mode stability, the waist radius must then be increased to $w_0 = 4.5\lambda$. This causes the radiation to expand more slowly, as shown in Figure 29; however, operation at $\alpha = 1$ requires the use of a depressed collector to obtain high output efficiencies. The envelope of the radiation at 560 GHz (not shown) changes significantly from the 280 GHz case only near the radiation waist. Unfortunately, a value of $\alpha = 1$ is undesirable for second harmonic operation, since the amount of ohmic power dissipated on the resonator mirrors increases rapidly as α decreases. To alleviate this problem at the expense of transverse efficiency, the value of μ may be raised to 18. This corresponds to $\alpha = 1.5$ and $w_0/\lambda = 4.5$ and should allow single-mode operation at normalized fields of $F = 0.07$ at a transverse efficiency of $\sim 40\%$.

Utilizing the above prescription, designs have been produced for 1 MW QOGs operating in the first harmonic at 120 and 280 GHz and in the second harmonic at 280 and 560 GHz. The electron beam parameters chosen were 80 kV and $\alpha = 1.0$ for the first harmonic designs, while $\alpha = 1.5$ was used for the second harmonic designs. The peak ohmic heating density (at the center of each mirror for the TEM₀₀ mode) was limited to 500 kW/cm² and essentially determined the mirror separation. The total power dissipated by each mirror is independent of the peak heating density chosen. The values of $\mu = 10$ and $F = 0.22$ were chosen by inspection from Figure 5 for the first harmonic resonator design. As discussed above, $\mu = 18$ and $F = 0.07$ were necessary to limit the ohmic losses and prevent excessive spreading of the radiation in the magnet crossbore in the second harmonic cases. Although these choices are based essentially on calculations for the fundamental harmonic, the second harmonic interaction is not expected to differ significantly. Thus, the perpendicular efficiency (which determines the electron beam current) is estimated at 50% for for the fundamental and

40% for the second harmonic designs. A better estimate of the efficiency and the region of single-mode stability will be possible when the calculations leading to Figure 5 are solved for second harmonic operation. Design parameters for a 1 MW, 150 GHz QOG have been obtained by Tran *et al.*⁽⁸⁾

The presence of a moderately efficient depressed collector was assumed that could recover the energy in the beam electrons motion parallel to the magnetic field as they pass through the resonator (i.e., 50% of the energy in an $\alpha = 1$ beam). This is a relatively conservative assumption, due to the facts that the parallel motion of the electrons is relatively unperturbed by the beam-wave interaction and that much of the beams transverse energy is converted to parallel energy via magnetic decompression prior to being collected. With these parameters specified, the remainder of the resonator parameters were calculated and are shown in Table III.

There are several points of interest to note in these designs. Firstly, the output couplings of the different cavities are fairly low (7.1 and 4.9%). This implies that the output power can be raised simply by reducing the diameter of the resonator mirrors (which increases the output coupling without affecting the other resonator parameters). Of course, it would be necessary to correspondingly increase the electron beam current, which would probably require a sheet electron beam.

Secondly, the number of interacting modes, which is given by

$$N_{\text{modes}} = \frac{\beta_{||0} d}{w_0}, \quad (34)$$

becomes quite large for the 280 and 560 GHz cavities. This number has been estimated by dividing the resonator longitudinal mode spacing ($\Delta f/f$) into the interaction bandwidth [Eq. (4)] with N_c given by the number of cyclotron orbits that an electron makes as it travels a distance of 2 radiation waist diameters (i.e. $4w_0$). It should be stressed that the large number of interacting modes does not alter the single-frequency stability region in the high-efficiency area of interest, and thus high-efficiency operation should not be affected for CW operation although the time required to establish the single-mode state may increase.⁽⁷⁾

The power lost to ohmic heating is higher for the second harmonic designs due to the somewhat weaker beam-wave coupling compared to the fundamental interaction. As can be seen from Eq. (19), this power depends strongly on the frequency but also depends somewhat on the output coupling. The ohmic power does not depend on g as do the peak and average heating densities, resulting in the fact that the heating densities may be reduced by moving the resonator mirrors apart, but the same amount of total ohmic power must still be dissipated.

VII. Conclusions

This paper has reviewed recent progress toward the development of high-power quasi-optical gyrotrons for ECRH of fusion plasmas. There has clearly been significant experimental and theoretical progress in the QOG since its invention a decade ago. Its outstanding feature is an open resonator formed by a pair of spherical mirrors instead of a waveguide resonator as in conventional gyrotrons. This configuration has the potential for overcoming conventional gyrotron limitations at high frequencies associated with high ohmic heating and problems with transverse mode competition due to the highly overmoded configuration, and with beam collection, since the beam must be collected along a section of the output waveguide. The QOG resonator mirrors can be well removed from the beam-wave interaction region, allowing a large volume for the interaction and low ohmic heating densities at the mirrors. The beam direction is transverse to the resonator so that beam collection is separate from the output waveguide. This geometry is particularly well suited to the use of a depressed collector for electron beam energy recovery. The QOG operates in the lowest-order transverse (TEM_{001}) Gaussian mode of the resonator, higher-order transverse modes being effectively suppressed by higher diffraction losses.

Proof-of-principle experiments have been carried out which have demonstrated the key advantages of the QOG concept, including low ohmic losses in the resonator, tunability, and separation of the electron and radiation beam. Powers up to 148 kW have been achieved at efficiencies up to 12%, and tunability from 95 to 130 GHz has been demonstrated. It is expected that pulsed QOG performance will be extended to the 0.5–1 MW power level and 20% efficiency level by a new device recently set up at NRL. These experiments are providing a data base for the development of multimewatt, 120 GHz CW QOGs for ITER and the development of 1 MW, 280 and 560 GHz CW QOGs for the Compact Ignition Tokamak.

An overview of QOG theory has been given which has shown the effectiveness of using normalized variables to characterize operation both in the fundamental and at higher harmonics of the cyclotron frequency. A highlight of recent theoretical work has been the

development of a theory predicting stable single-mode operating regimes for fundamental harmonic operation with highly overmoded resonators. The application of this theory to harmonic operation is of considerable interest and is currently underway. A substantial improvement in efficiency—transverse efficiencies up to 50%—and single-mode stability has recently been predicted when the resonator and electron beam axes are tilted a few degrees from perpendicular and an early experimental test is planned.

Scaling equations for the output power and ohmic heating of resonator mirrors have been given. The design tradeoffs between annular and sheet electron beams have been discussed as has the issue of beam space charge depression in the open resonator. The application of a depressed collector has been discussed as a means of recovering the energy in the axial motion of the spent electron beam and, thus, raising the output efficiency to near the transverse electronic efficiency. The problem of high field magnet design has been addressed, for both fundamental and higher harmonic operation, the latter being necessary to achieve frequencies above 300 GHz. The design equations and tradeoffs have been applied to the design of 1 MW, CW quasi-optical gyrotrons operating in the fundamental harmonic at 120 GHz, in the first and second harmonic at 280 GHz, and in the second harmonic at 560 GHz. The output coupling for these 1 MW designs is 5–7% showing the potential for even higher powers per tube if sheet-beam electron guns can be developed. The estimated electronic efficiency of the fundamental harmonic designs is 23%, which leads to an output efficiency of 47% through the use of a depressed collector with a modest collection efficiency. The peak ohmic heating density is 500 W/cm^2 in all designs. This leads to resonator mirror separations ranging from 127 cm for 120 GHz design, to 232 cm for the 560 GHz, second harmonic design. Finally, a simple output system composed of an elliptical and a parabolic mirror has been described that converts the output radiation from the resonator into a parallel, quasi-Gaussian beam.

Experimental programs have been reviewed, especially the recent experiment at the Naval Research Laboratory that produced frequencies ranging from 95–130 GHz and powers up to 150 kW. A highlight of this experiment was the demonstration of operation in a

single mode at powers up to 125 kW despite the resonator being highly overmoded. Comparison with the theoretically predicted region of single-mode operation showed reasonable agreement between theory and experiment. Recent progress in the experimental characterization of QOG resonators has been summarized. Previous QOG experiments have utilized resonator configurations which have emphasized the flexible variation of parameters. Future investigations at NRL will develop coolable mirror configurations and output coupling systems for producing a linearly polarized Gaussian beam.

VIII. Acknowledgements

We thank Drs. B. Levush and T. Antonsen for several helpful discussions during the completion of this work. This work was supported by the Office of Fusion Energy of the Department of Energy and by the Office of Naval Research.

References

1. K. Felch, R. Bier, L.J. Cragi, H. Huey, L. Ives, H. Jory, N. Lopez, and S. Spang, *Int. J. Elec.* **61**, 701 (1986).
2. K.E. Kreischer and R.J. Temkin, *Phys. Rev. Lett.* **59**, 547 (1987); K.E. Kreischer, *Bull. Amer. Phys. Soc.* **33**, 1913 (1988).
3. P. Sprangle, J. Vomvoridis and W.M. Manheimer, *Appl. Phys. Lett.* **38**, 310 (1981) and *Phys. Rev. A* **23**, 3127 (1981).
4. A. Bondeson, W.M. Manheimer and E. Ott, *Infrared and Millimeter Waves* (Academic Press, 1983), ed. by K.J. Button, Vol. 9, Chapter 7.
5. B. Levush and W.M. Manheimer, *Int. J. Infrared and Millimeter Waves* **4**, 877 (1983).
6. B. Levush, A. Bondeson, W.M. Manheimer, and E. Ott, *Int. J. Elec.* **54**, 749 (1983).
7. T. Antonsen, B. Levush and W.M. Manheimer, submitted to *Phys. Fluids*.
8. T.M. Tran, M.Q. Tran, S. Alberti, J.P. Hogge, B. Isaak, P. Muggli, and A. Perrenoud, *IEEE Trans. Elect. Dev.* **36**, 1983 (1989).
9. T.A. Hargreaves, K.J. Kim, J.H. McAdoo, S.Y. Park, R.D. Seeley, and M.E. Read, *Int. J. Elec.* **57**, 977 (1984).
10. A.W. Fliflet, T.A. Hargreaves, W.M. Manheimer, R.P. Fischer, and M.L. Barsanti, *Phys. Rev. Lett.* **62**, 2664 (1989).
11. A.W. Fliflet, T.A. Hargreaves, W.M. Manheimer, R.P. Fischer, M.L. Barsanti, B. Levush, and T. Antonsen, submitted to *Phys. Fluids*.
12. P. Sprangle and A.T. Drobot, *IEEE Trans. Microwave Th. and Tech.*, MTT **25**, 528 (1977).

13. K.E. Kreischer and R.J. Temkin, *Infrared and Millimeter Waves*(Academic Press, New York, 1983), ed. by K.J. Button, Vol. 7, Ch. 8.
14. Ch.-Y. Wang, K.E. Kreischer, and R.J. Temkin, *IEEE Trans. on Electron Devices* **35**, 1166 (1988).
15. A. Bondeson, W.M. Manheimer and E. Ott, *Phys. Fluids* **26**, 285 (1983).
16. T.M. Tran, B.G. Danly, K.E. Kreischer, J.B. Schutkeker, and R.J. Temkin, *Phys. Fluids* **29**, 1274 (1986).
17. B.G. Danly and R.J. Temkin, *Phys. Fluids* **29**, 561 (1986).
18. M.Q. Tran, A. Bondeson, A. Perrenoud, S. Alberti, B. Isaak, and P. Muggli, *Int. J. Elec.* **61**, 1029 (1986).
19. W.M. Manheimer, A.W. Fliflet, J. Burke, and T.A. Hargreaves, *Naval Research Laboratory Memorandum Report* 6165 (1988).
20. K.E. Kreischer, B.G. Danly, J.B. Schutkeker, and R.J. Temkin, *IEEE Trans. on Plasma Science* **PS-13**, 364 (1985).
21. A.K. Ganguly and K.R. Chu, *Int. J. Infrared and Millimeter Waves* **5**, 103 (1984).
22. M.E. Read, A.J. Dudas, W. Lawson, and A. Singh, *Thirteenth International Conference on Infrared and Millimeter Waves*, Richard J. Temkin, Editor, SPIE Vol. 1039, 181 (1988).
23. W.M. Manheimer, A.W. Fliflet and R.C. Lee, to be published in *IEEE Trans. on Electron Devices*, Vol. II (1989).
24. M.E. Read, A.J. Dudas, J.J. Petillo, and A. Drobot, *Thirteenth International Conference on Infrared and Millimeter Waves*, Richard J. Temkin, Editor, SPIE Vol. 1039, 279 (1988).

25. J.M. Finn, A.W. Fliflet, and W.M. Manheimer, *Int. J. Electronics* **61**, 985 (1986).
26. S.E. Tsimring, *Radiophysics and Quantum Electronics* **20**, 1550 (1972).
27. A.W. Fliflet, A.J. Dudas, M.E. Read, and J.M. Baird, Jr., *Int. J. Electronics* **53**, 743 (1982).
28. W.B. Herrmannsfeldt, *SLAC Report* 226, Stanford Linear Accelerator Center, Stanford, CA (1979).
29. S. Pissanetsky, *Computational Electromagnetics* (1986).
30. M.E. Read, M.Q. Tran, J. McAdoo, and M. Barsanti, *Int. J. Elec.* **65**, 309 (1988).
31. Y. Zhonghai and L. Shenggang, *Int. J. Elec.* **57**, 1003 (1984).
32. X. Kongyi and L. Shenggang, *Int. J. Elec.* **57**, 1019 (1984).
33. E.C. Morse and R.V. Pyle, *J. Vacuum Sci. and Tech. A* **3**, 1239 (1985).
34. Y. Itoh, M. Komuro, K. Hayashi, and T. Sugawara, *Thirteenth International Conference on Infrared and Millimeter Waves*, Richard J. Temkin, Editor, SPIE Vol. 1039, 277 (1988).
35. Presented at the Thirteenth International Conference on Infrared and Millimeter Waves, Honolulu, HI (December 1988).
36. R.P. Fischer, T.A. Hargreaves, and A.W. Fliflet, *Naval Research Laboratory Memorandum Report* 6531 (1989).
37. R.N. Clark and C.B. Rosenberg, *J. Phys. E* **15**, 9 (1982).
38. H. Derler, T.J. Grant, and D.S. Stone, *IEEE Trans. Electron Devices*, **ED-29**, 1917 (1982).
39. P. P. Woskoboinikow and W. J. Mulligan, *IEEE Trans. Microwave Th. and Tech.*, **MTT 35**, 96 (1987).

40. A. Perrenoud, M.Q. Tran, B. Isaak, A. Alberti, and P. Muggli, *Int. J. Infrared and Millimeter Waves* **7**, 1813 (1986).
41. A. Perrenoud, T.M. Tran, M.Q. Tran, C. Rieder, M. Schleipen, and A. Bondeson, *Int. J. Elec.* **57**, 985 (1984).

TABLE I
Resonator Parameters for the 150 kW QOG Experiment at NRL

Frequency (f)	120 GHz		
Wavelength (λ)	0.25 cm		
Mirror Diameter ($2a$)	5.0 cm		
Radius of Curvature (R_c)	38.7 cm		
Mirror Separation (d)	20	24	28 cm
Longitudinal Mode Spacing ($\Delta f/f$)	0.63	0.52	0.45%
Radiation Waist Radius (w_o)	1.16	1.19	1.22 cm
w_o/λ	4.6	4.8	4.9
μ ($E = 70$ keV, $\alpha = 1.0$)	9.8	10.1	10.3
Transmission Coefficient (T , round trip)	0.4	1.5	2.3%
Diffraction Quality Factor (Q_d)	257,000	83,000	62,000
Ohmic Quality Factor (Q_o)	462,000	554,000	647,000
Total Quality Factor (Q)	165,000	72,000	57,000
Fresnel Number ($a^2/\lambda d$)	1.25	1.04	0.89
g ($1 - d/R_c$)	0.48	0.38	0.28

TABLE II

Design Parameters of the Current QOG Experiment at NRL

Frequency (f)	120 GHz		
Wavelength (λ)	0.25 cm		
Electron Energy	80 keV		
Electron Current	50 A		
Output Power	0.5-1 MW		
Mirror Diameter ($2a$)	4.5 cm		
Radius of Curvature (R_c)	38.7 cm		
Mirror Separation (d)	20	24	28 cm
Longitudinal Mode Spacing ($\Delta f/f$)	0.63	0.52	0.45%
Number of Interacting Modes	~ 5	~ 5	~ 6
Radiation Waist Radius (w_o)	1.16	1.19	1.2 cm
w_o/λ	4.6	4.8	4.9
Normalized Interaction Length (μ)	10-17	10-17	10-18
Transmission Coefficient (T , round trip)	2.2	4.9	6.0%
Diffraction Quality Factor (Q_d)	45,000	24,700	25,000
Ohmic Quality Factor (Q_o)	540,000	648,000	756,000
Total Quality Factor (Q)	41,500	23,800	24,200
Fresnel Number ($a^2/\lambda d$)	1.01	0.84	0.72
$g (1 - d/R_c)$	0.48	0.38	0.28
Normalized Electric Field (F)	0.12		
Peak Ohmic Heating Density	890	830	760 W/cm ²
Total Ohmic Power (per mirror)	2.5	2.6	2.7 kW

TABLE III

Design Parameters for 1 MW CW QOGs at 120, 280, and 560 GHz

Frequency (f)	120	280	280	560 GHz
Wavelength (λ)	2.5	1.1	1.1	0.54 mm
Harmonic Number	1	1	2	2
Electron Energy	80	80	80	80 keV
Electron Current	54	54	48	48 A
Velocity Pitch Ratio (α)	1.0	1.0	1.5	1.5
Output Power	1	1	1	1 MW
Electronic Efficiency	23	23	26	26%
Output Efficiency	47	47	37	37%
Peak Ohmic Heating Density	500	500	500	500 W/cm ²
Total Ohmic Power (per mirror)	4.1	6.3	9.2	13.1 kW
Normalized Electric Field (F)	0.22	0.22	0.07	0.07
Normalized Interaction Length (μ)	10	10	18	18
Mirror Diameter ($2a$)	8.6	11	13	16 cm
Mirror Separation (d)	58	80	97	116 cm
Radius of Curvature (R_c)	37	41	49	58 cm
$g(1 - d/R_c)$	-0.539	-0.945	-0.962	-0.993
Output Coupling (T , round trip)	7.1	7.1	4.9	4.9%
Radiation Waist Radius (w_o)	1.12	0.48	0.48	0.24 cm
w_o/λ	4.5	4.5	4.5	4.5
Longitudinal Mode Spacing ($\Delta f/f$)	0.22	0.067	0.055	0.023%
Number of Interacting Modes	~ 18	~ 59	~ 56	~ 135

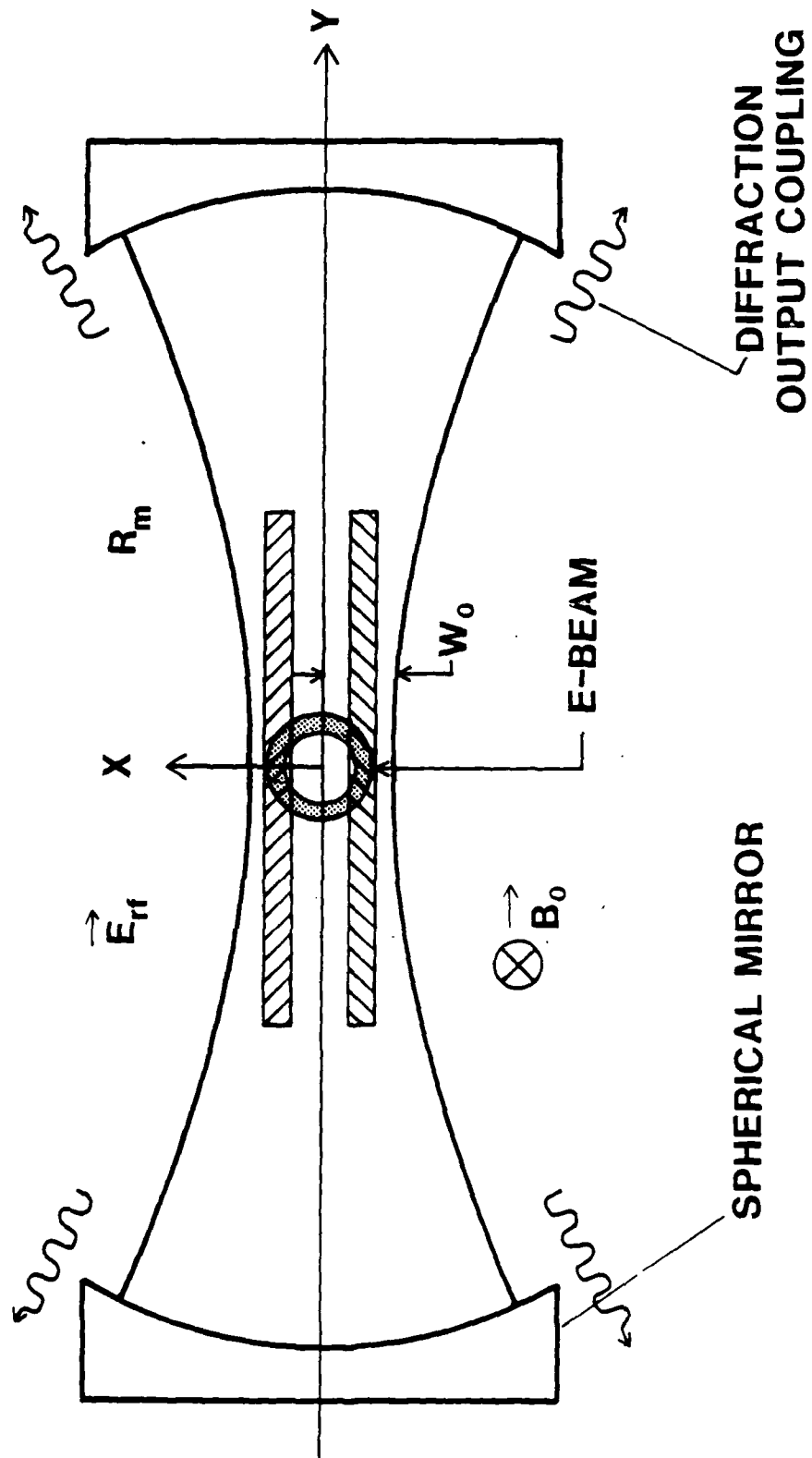


Figure 1. The quasi-optical gyrotron resonator showing the geometry of the external magnetic field (\vec{B}_0), the RF electric field (\vec{E}_{rf}), and the electron beam. Both the annular electron beam and the double sheet beam are indicated.

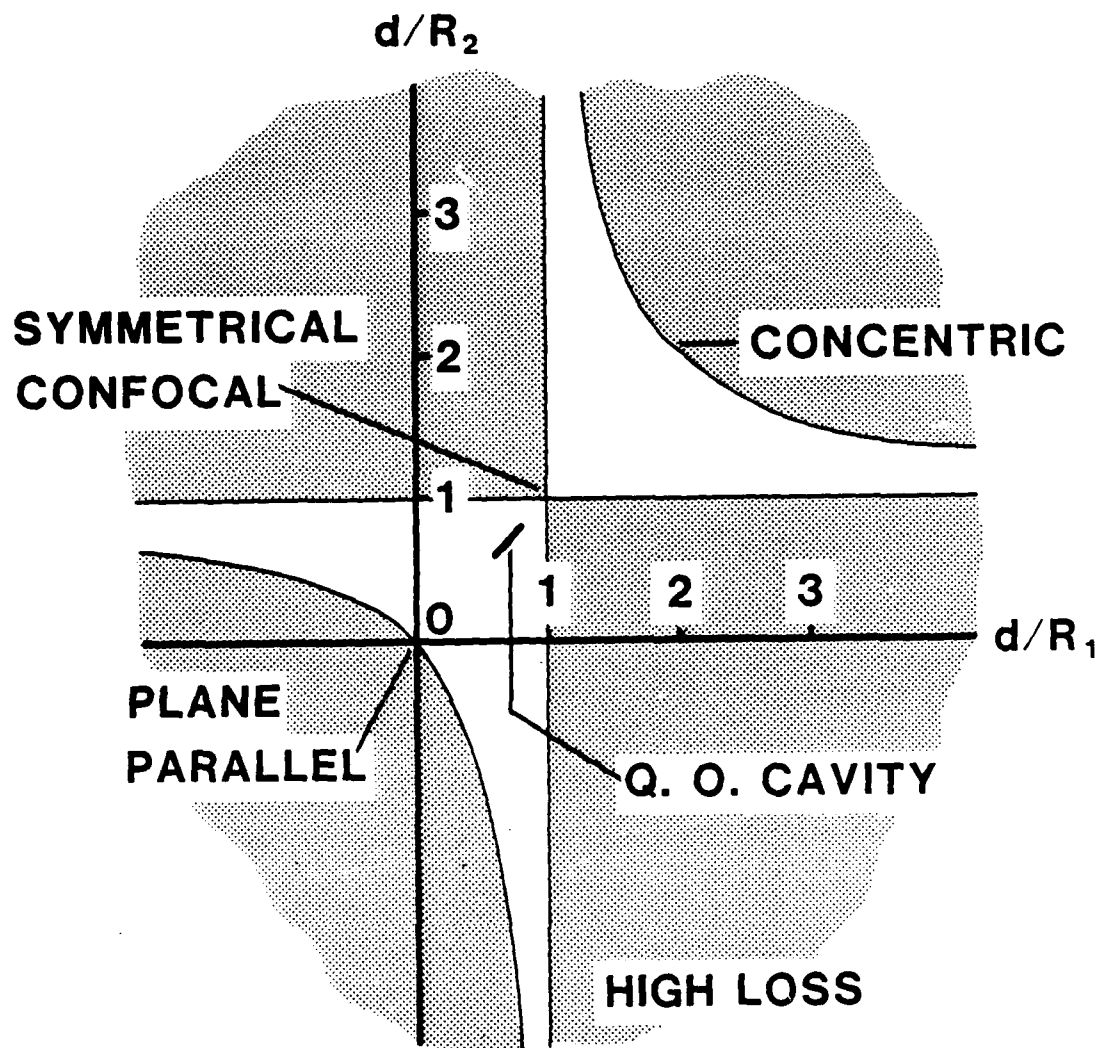


Figure 2. Open resonator stability diagram. The shaded (high-loss) areas are those in which the stability criterion $(0 \leq (1 - d/R_1)(1 - d/R_2) \leq 1)$ is not satisfied. Note that the experimental design of the recently completed NRL experiment lies well within the stable region.

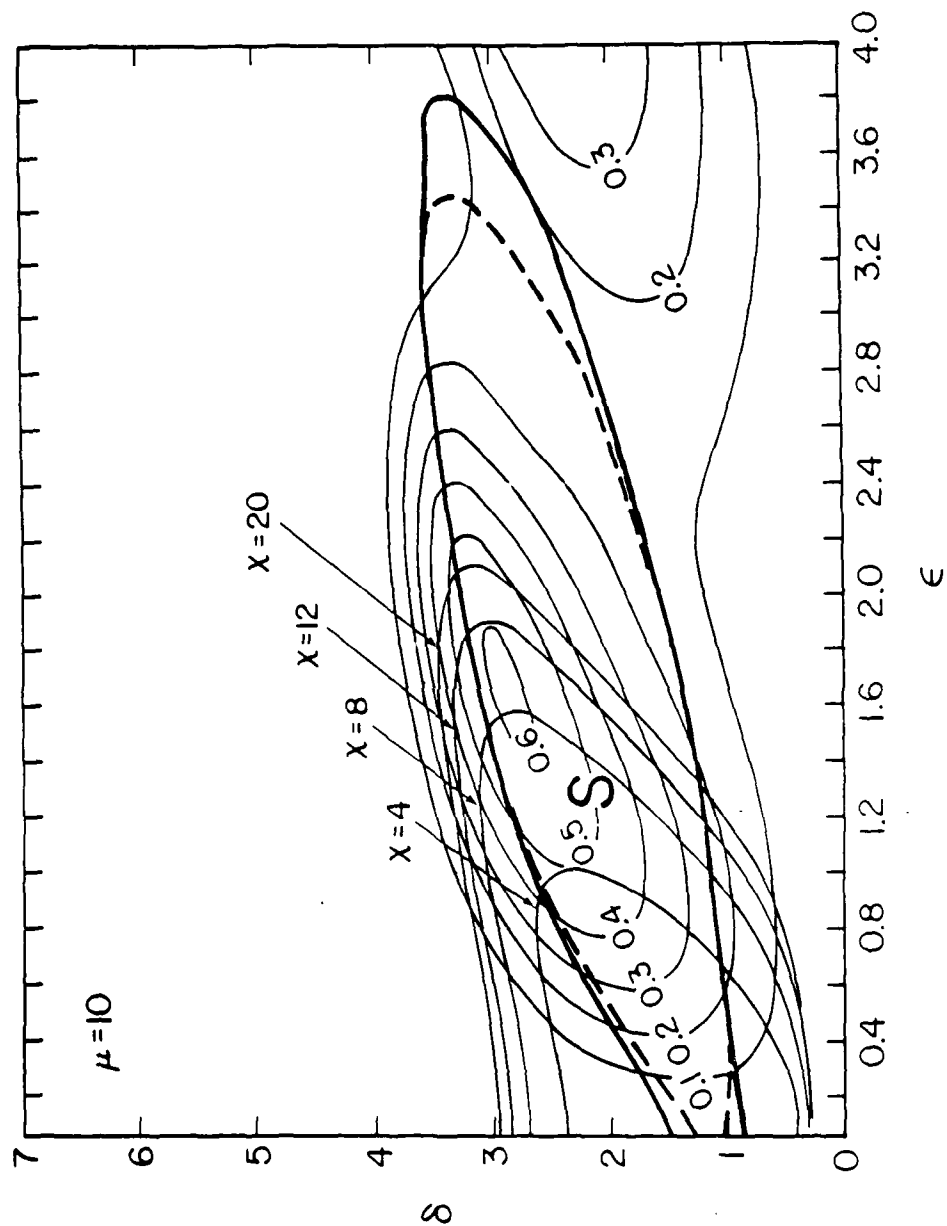


Figure 3. $\epsilon - \delta$ plot calculated by Antonsen et al.⁽⁷⁾ of QOG single mode transverse efficiency, η_1 for a pencil electron beam and $\mu = 10$. The region of stable single mode equilibria for $\xi = 10$ is indicated by the heavy solid curve, and the region for $\xi = 50$ is indicated by the heavy dashed curve.

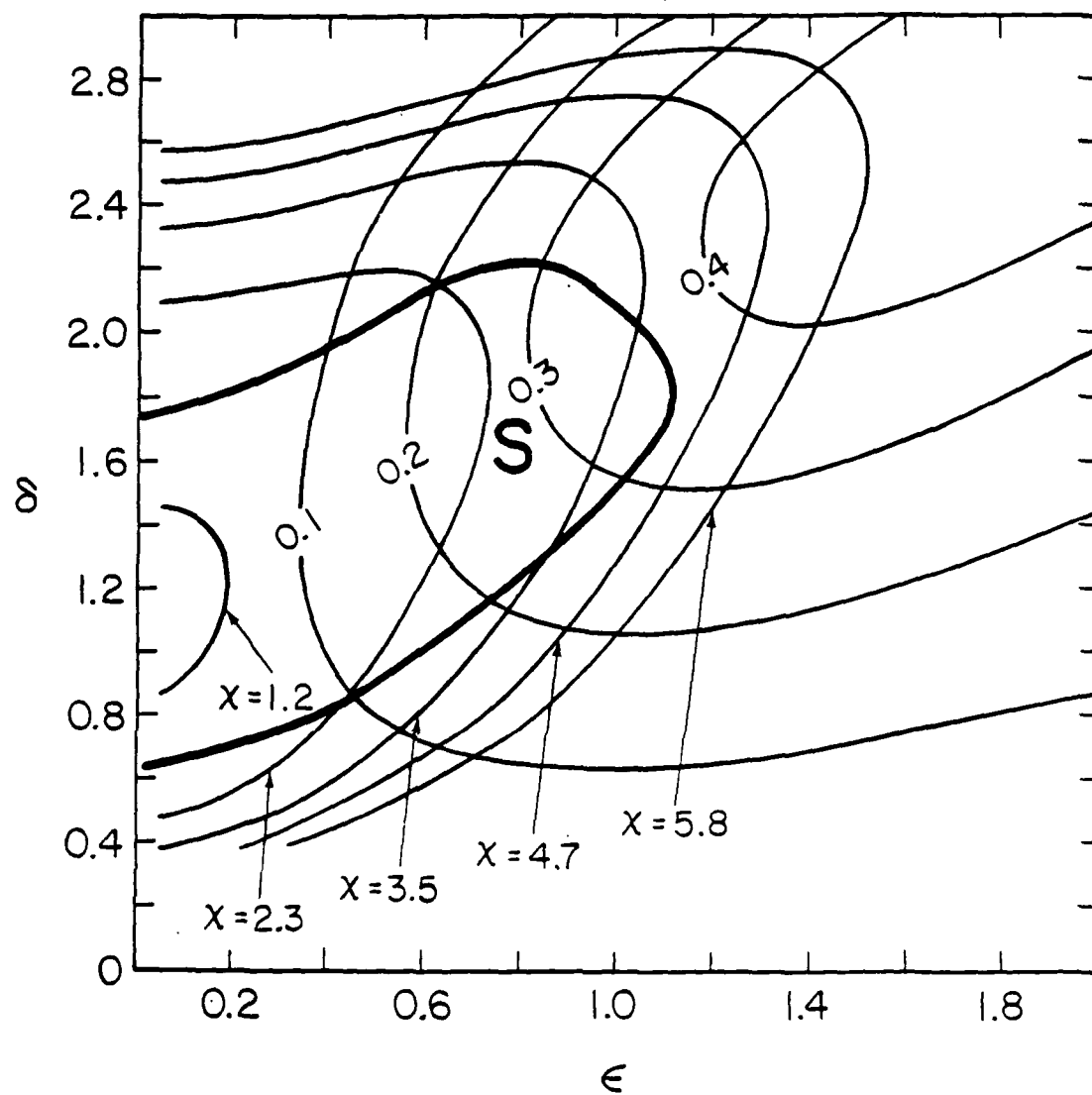


Figure 4. $\epsilon - \delta$ plot calculated by Antonsen et al.⁽⁷⁾ of QOG single mode transverse efficiency, η_{\perp} for an annular electron beam, $\mu = 10$, and perpendicular electron beam and resonator axes. The region of stable single mode equilibria is indicated by the heavy solid curve.

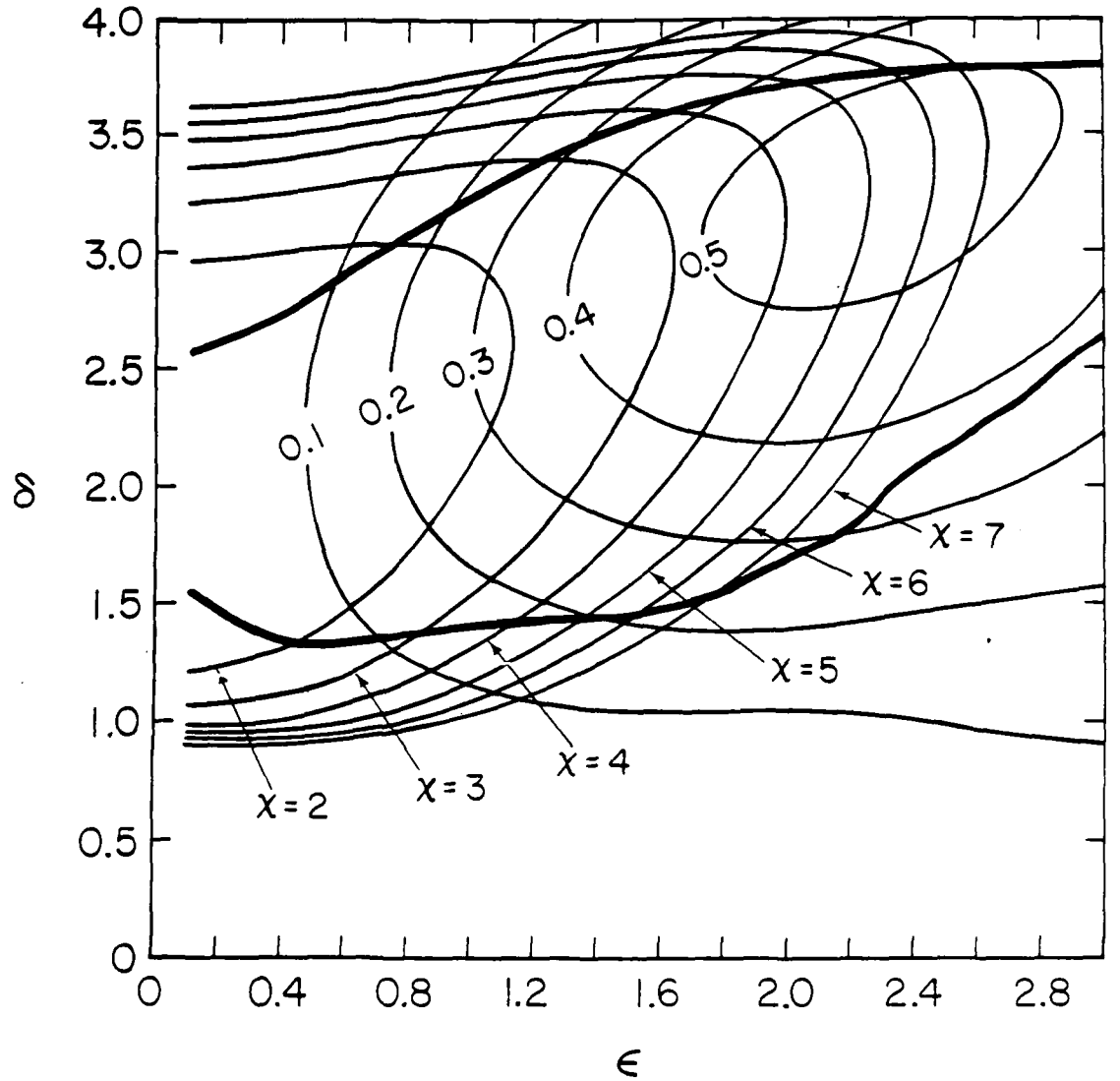


Figure 5. $\epsilon - \delta$ plot calculated by Antonsen et al.⁽⁷⁾ of QOG single mode transverse efficiency, η_{\perp} for an annular electron beam and $\mu = 10$. The electron beam axis is tilted by a small angle ($\theta' = 1$) from the direction perpendicular to the resonator axis. The region of stable single mode equilibria is indicated by the heavy solid curve.

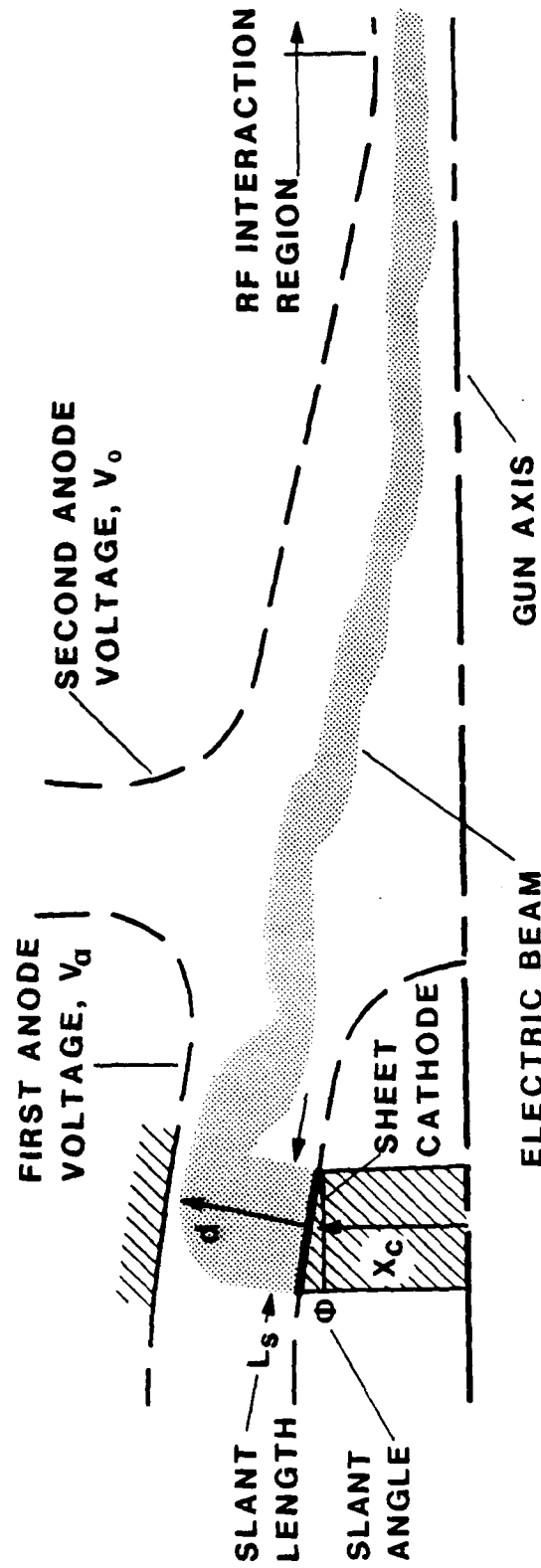


Figure 6. Schematic of MIG-type sheet-beam electron gun. The configuration is assumed to be symmetric about the plane containing the gun axis.

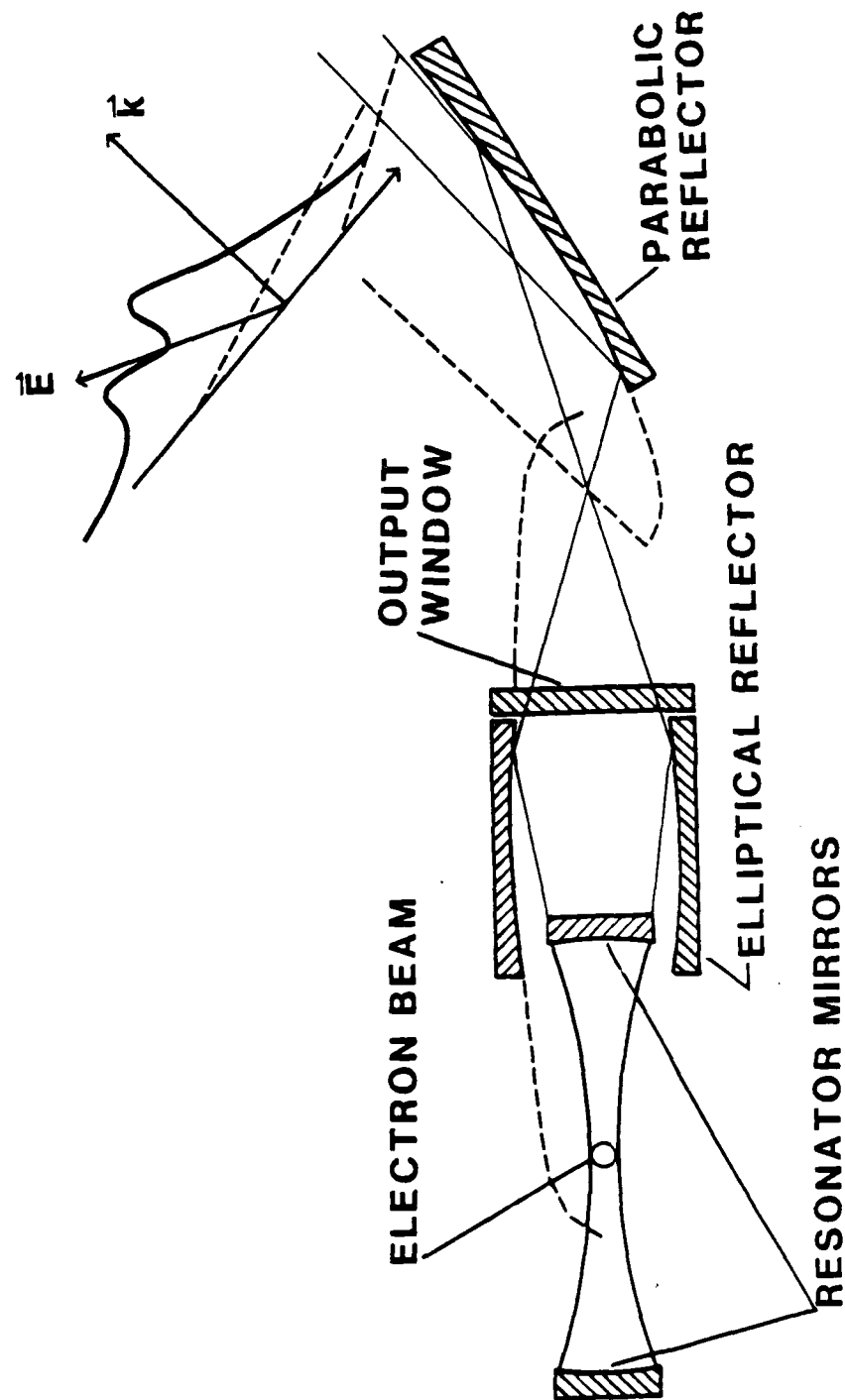


Figure 7. Conceptual design of a quasi-optical gyrotron output coupling system. The resonator output radiation is converted into a parallel beam by means of elliptic and parabolic reflectors.

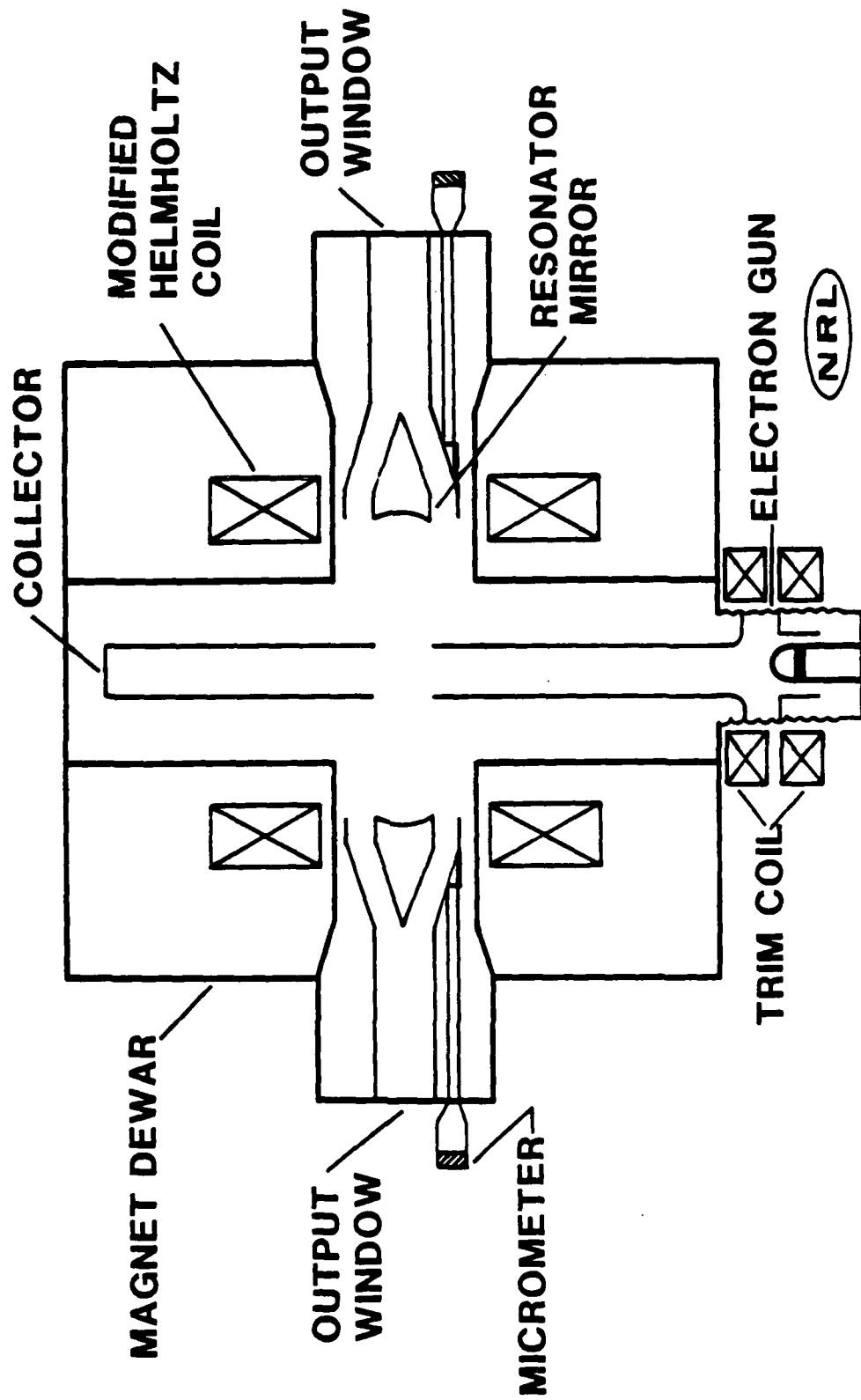


Figure 8. Schematic diagram of the recent 120 GHz, 150 kW NRL quasi-optical gyrotron experiment.

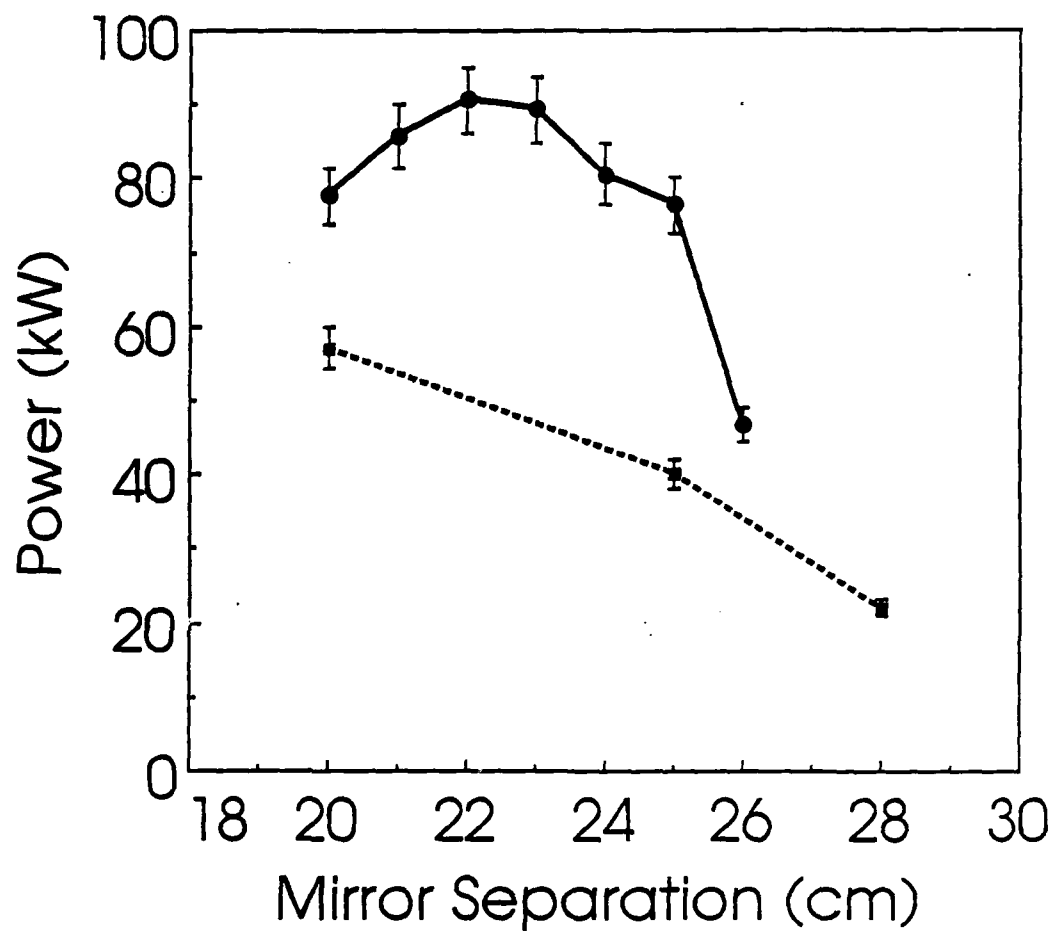


Figure 9. Output power vs. mirror separation for a 50 kG magnetic field. The solid square data corresponds to a gun voltage of $V = 66.7$ kV and a beam current of 8 A. The solid dot data corresponds to a gun voltage of $V = 71.5$ kV and a beam current 13.5 A.

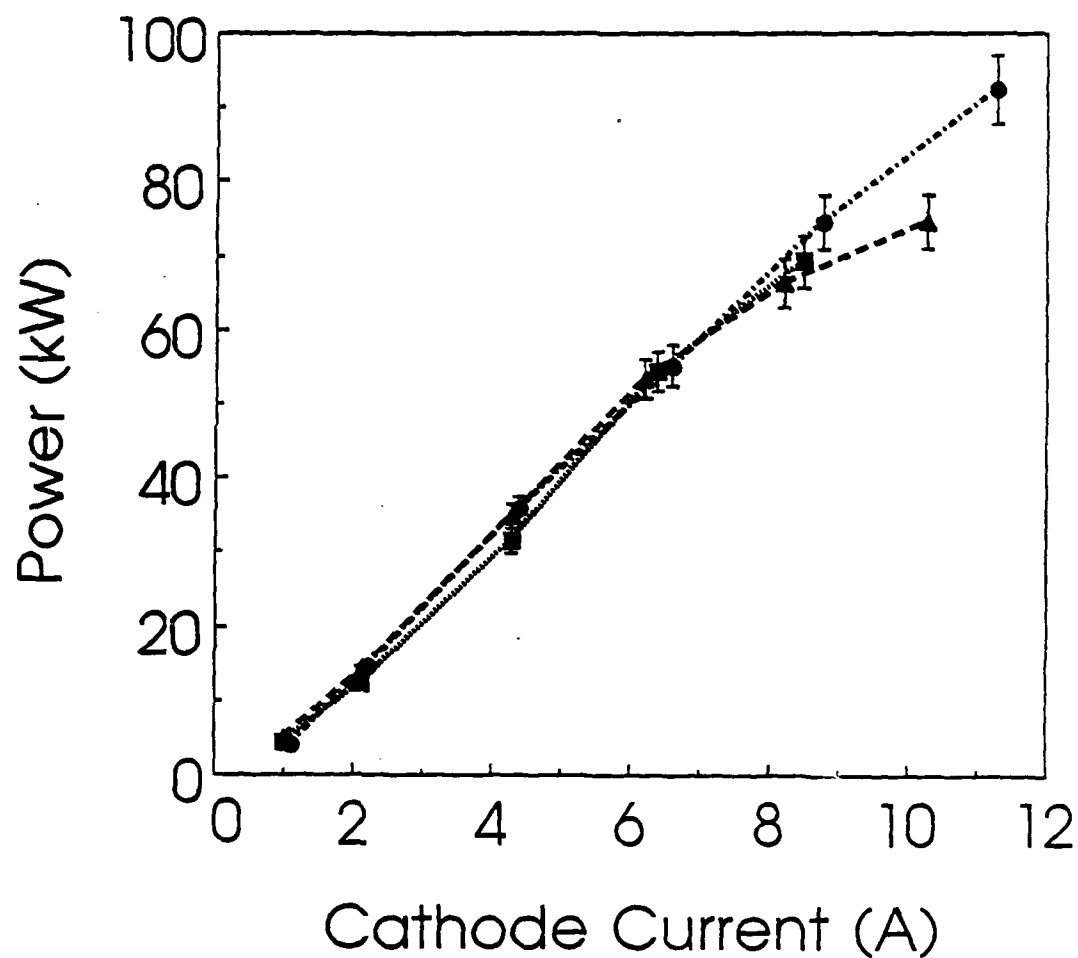


Figure 10. Output power vs. beam current for 20 cm mirror separation and a gun voltage of 71.5 kV. The magnetic field is 44, 47, and 50 kG for the solid square, solid dot, and solid triangle data, respectively.

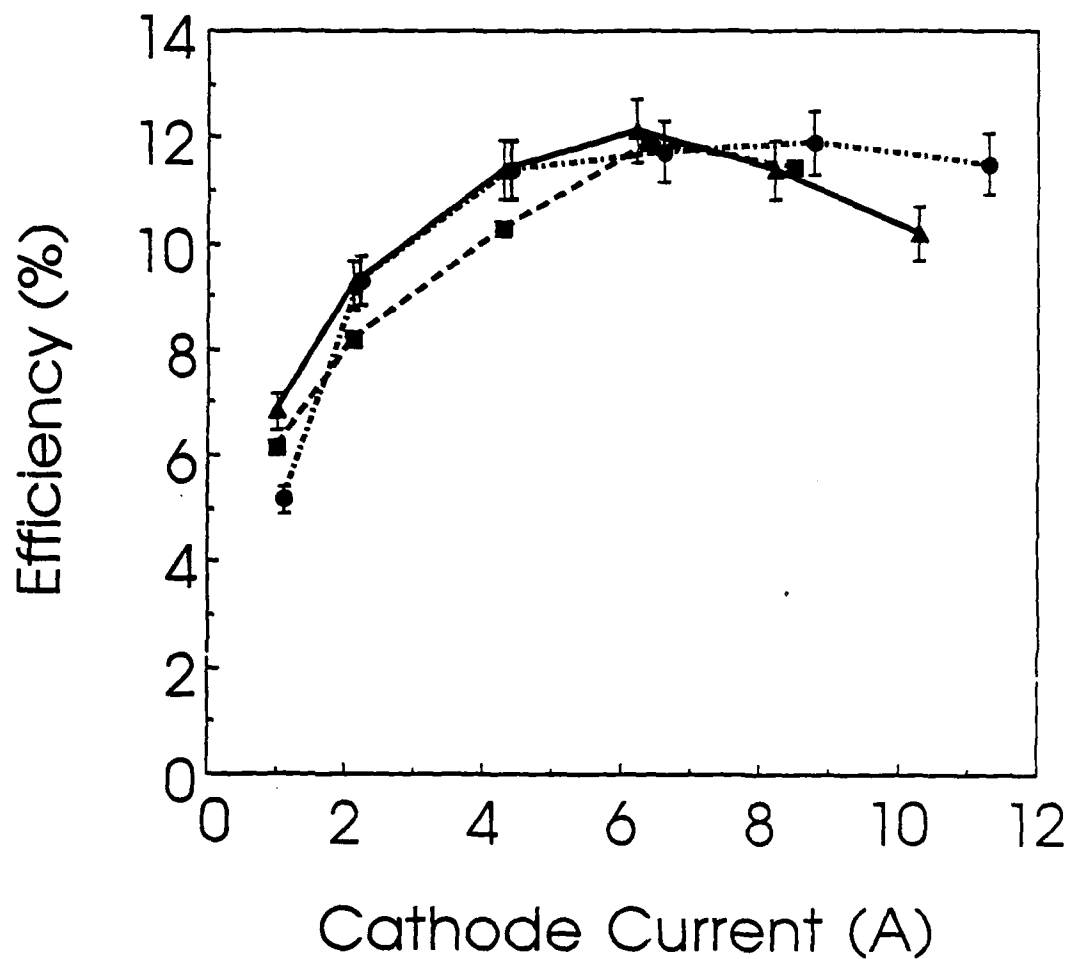


Figure 11. Output efficiency vs. beam current for 20 cm mirror separation and a gun voltage 71.5 kV. The magnetic field is 44, 47, and 50 kG for the solid square, solid dot, or solid triangle data, respectively.

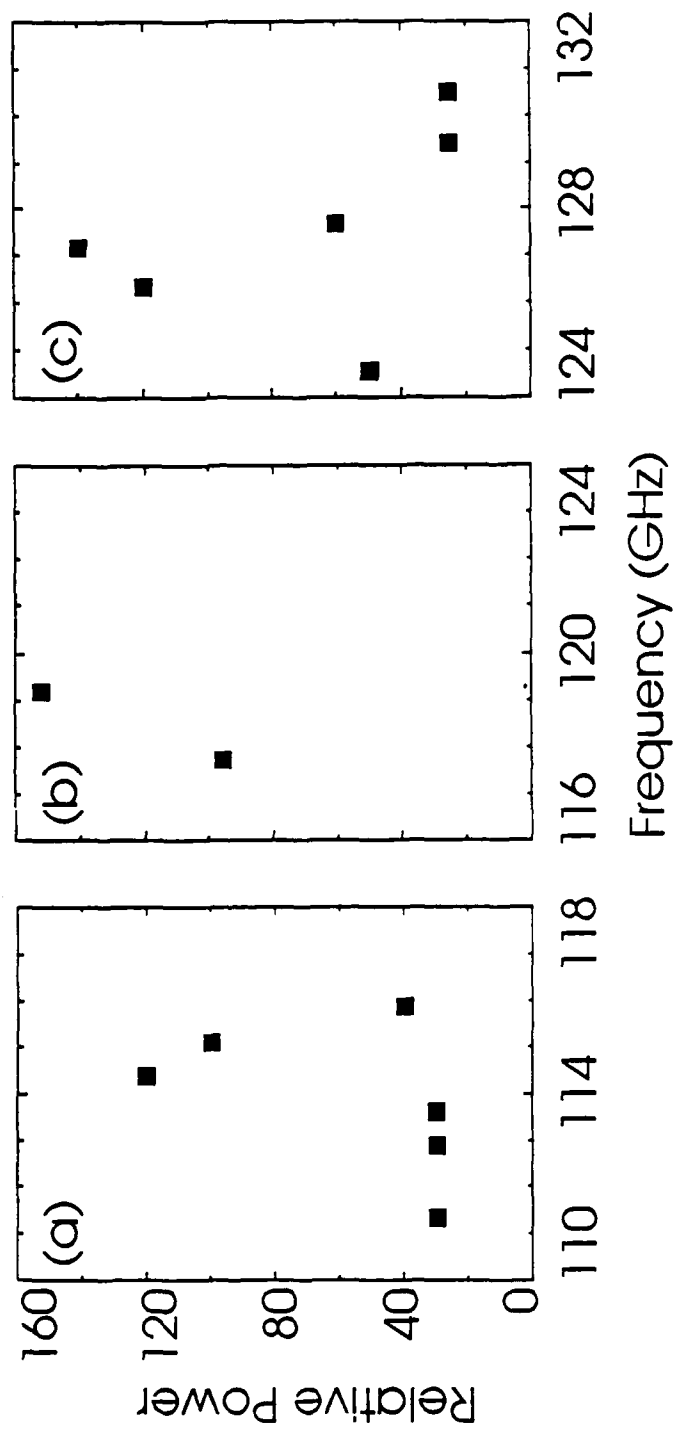


Figure 12. Typical multimode frequency spectra for a mirror separation of 20 cm and a gun voltage of 71.5 cm. (a): $B = 44$ kG, $I = 8$ A; (b): $B = 47$ kG, $I = 14$ A; (c): $B = 50$ kG, $I = 8$ A.

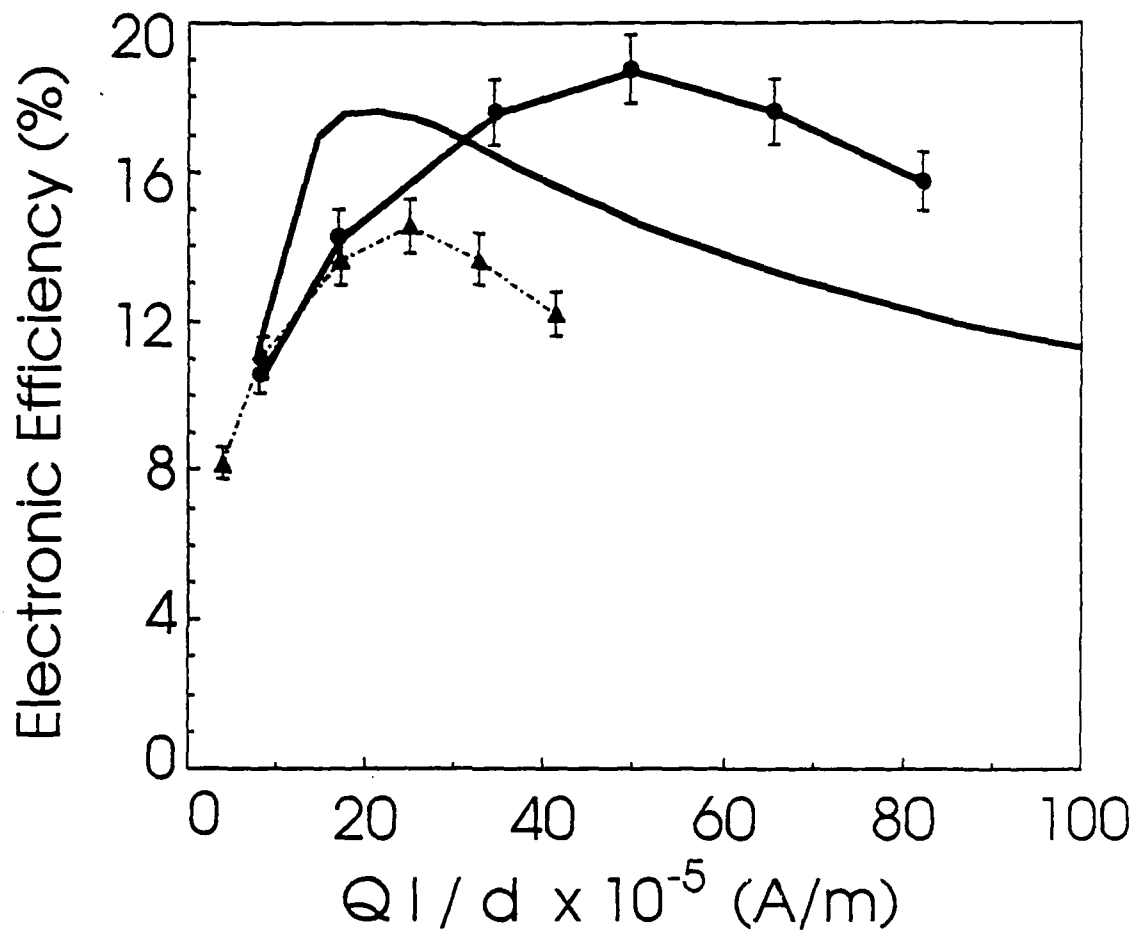


Figure 13. Electronic efficiency vs. QI/d . The solid curve shows results from a multimode, annular beam simulation. The solid dots and triangles show the estimated electronic efficiency for the 50 kG power data shown in Figure 10. The solid dots are based on the diffraction Q obtained from scalar diffraction theory, and the solid triangles are based on the Q inferred from the threshold current data.

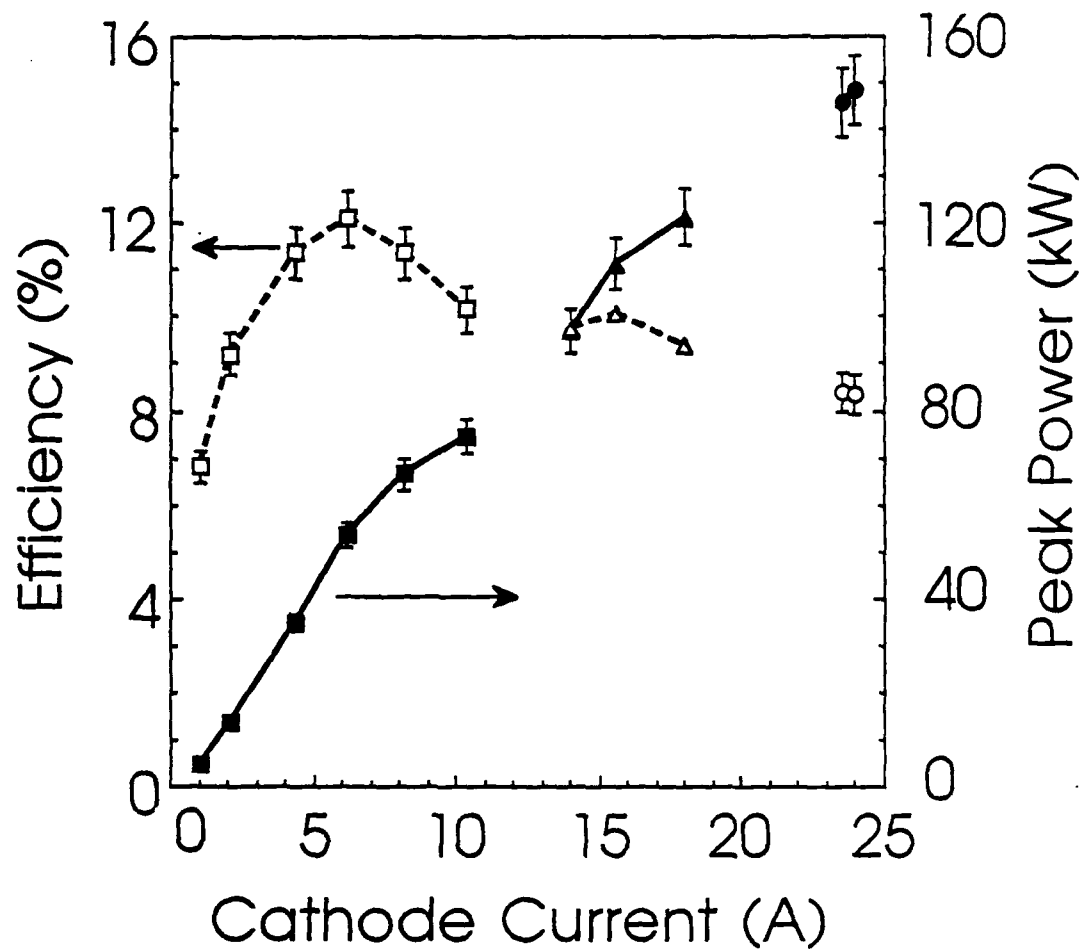


Figure 14. Output power and efficiency operation with a 50 kG resonator magnetic field and gun voltages of 71-74 kV. The mirror separation for the data shown by the solid and open squares is 20 cm, and is 23 cm for the data shown by the solid and open circles and triangles. The resonator magnetic field has a 2% negative taper for the data shown by the solid and open circles.

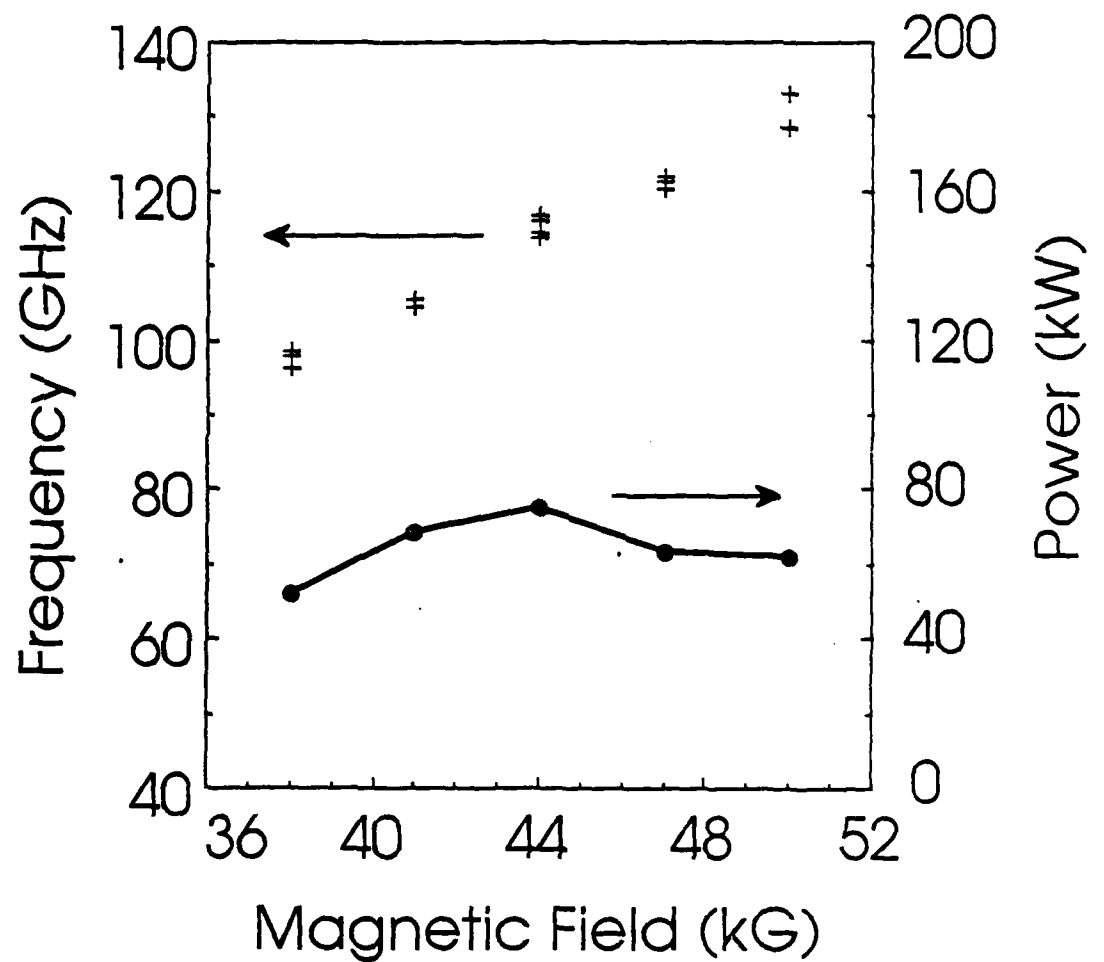


Figure 15. Frequency tuning by magnetic field variation. The oscillation frequencies are shown by + signs and the output power is shown by the solid dots. The gun voltage and beam current are 66.7 kV and 12 A, respectively, and the mirror separation is 20 cm.

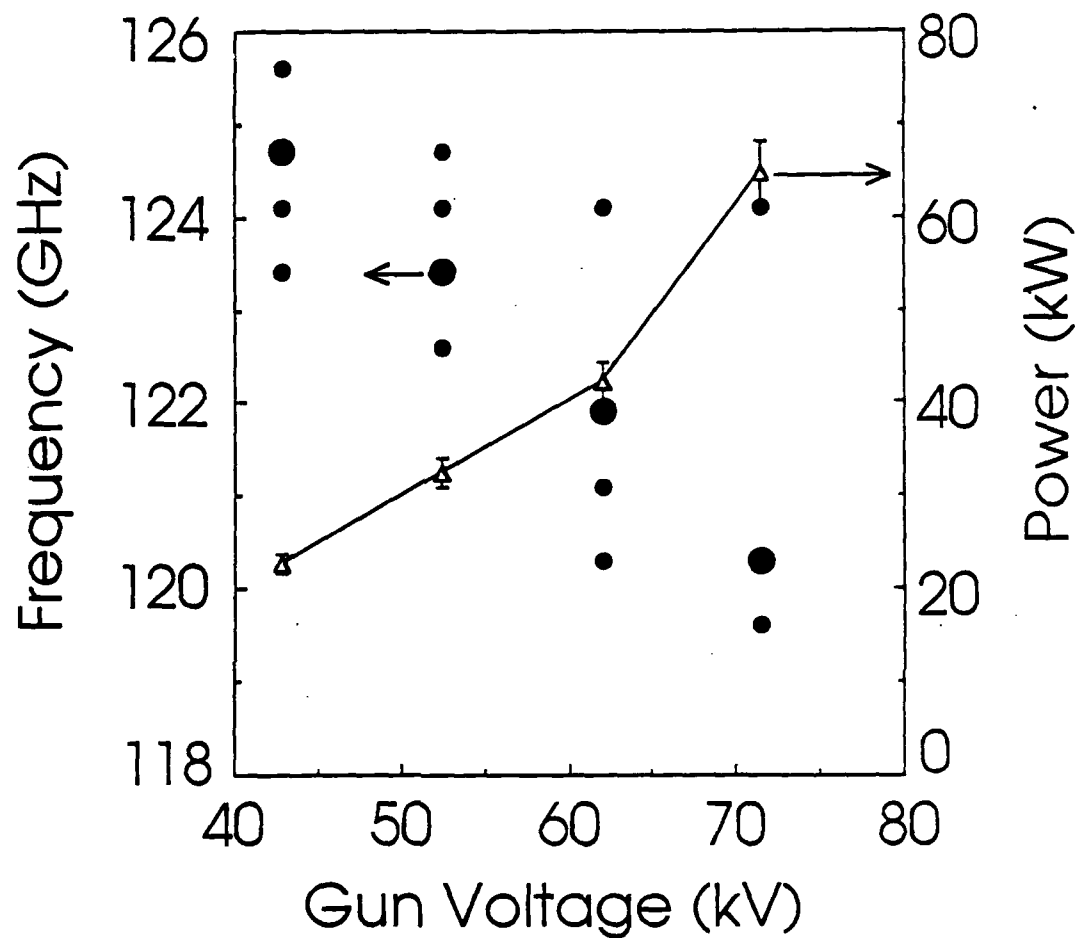


Figure 16. Frequency tuning with gun voltage variation for a magnetic field of 50 kG, a current of ~ 10 A and a 20 cm mirror separation. The oscillation frequencies are shown by the solid dots and the large dots indicate the dominant mode.

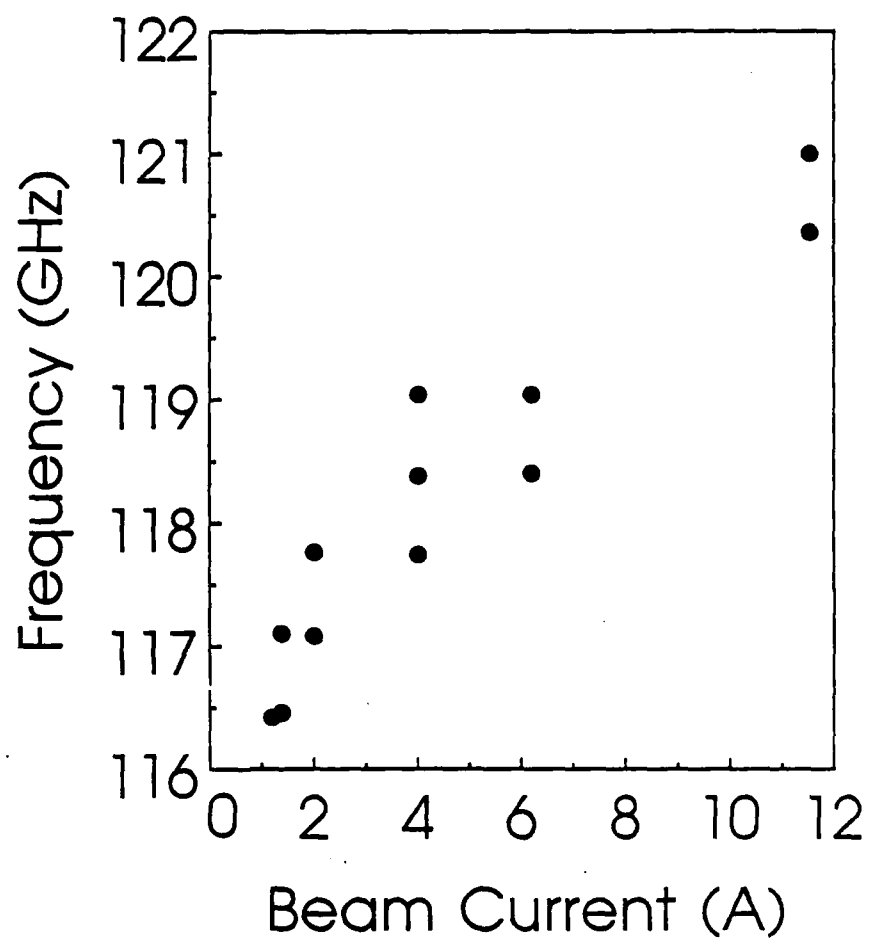


Figure 17. Mode frequencies as a function of current for a magnetic field of 47 kG with a 2% negative taper, a fixed voltage of 71.5 kV, and a 23 cm mirror separation.

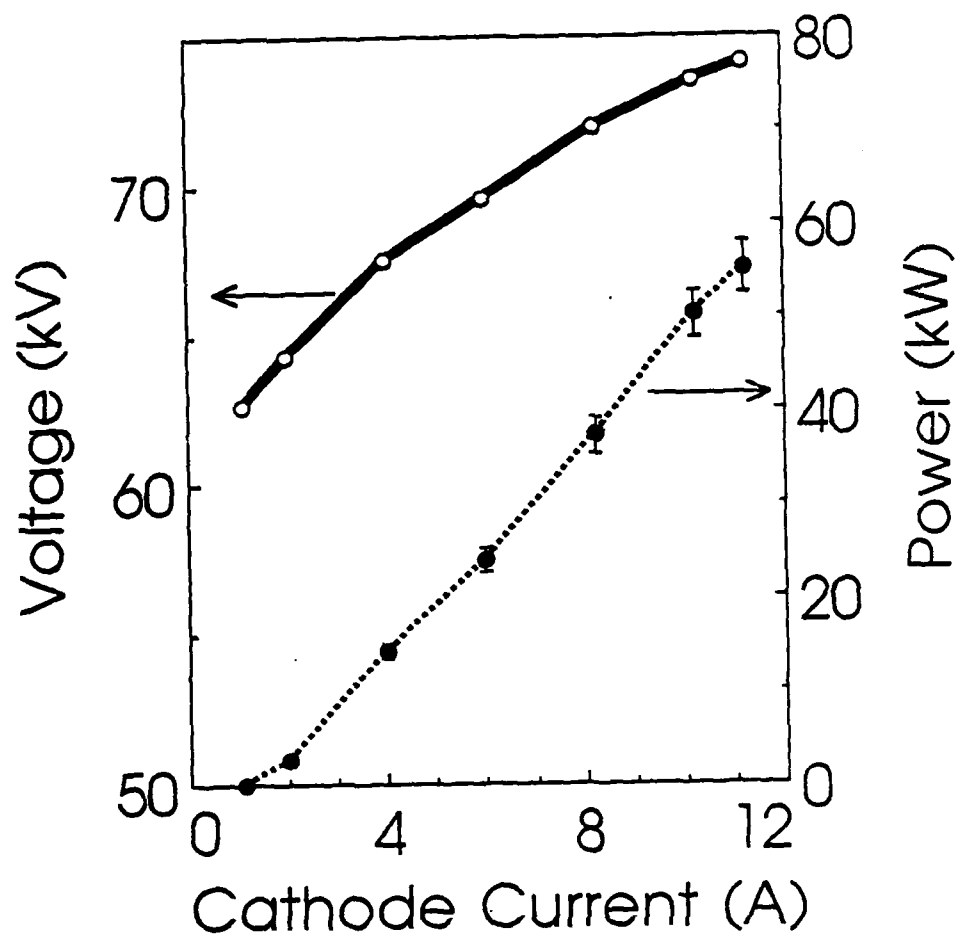


Figure 18. A region of single-mode operation in $V - I$ space. The magnetic field is 47 kG and the frequency is 119 GHz.

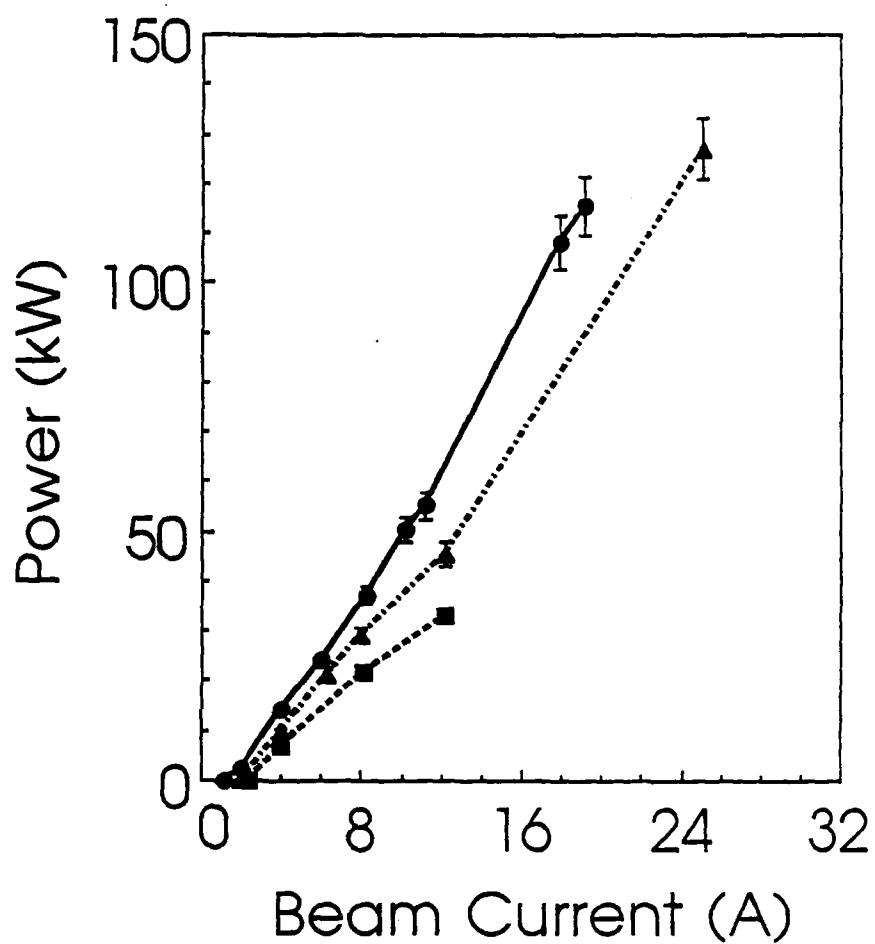


Figure 19. Output power for single-moded or near-single-moded operation for a magnetic field of 47 kG and frequencies of 119–120 GHz. The mirror separation is 23, 25.5 and 28 cm for the solid dots, triangles, and squares, respectively.

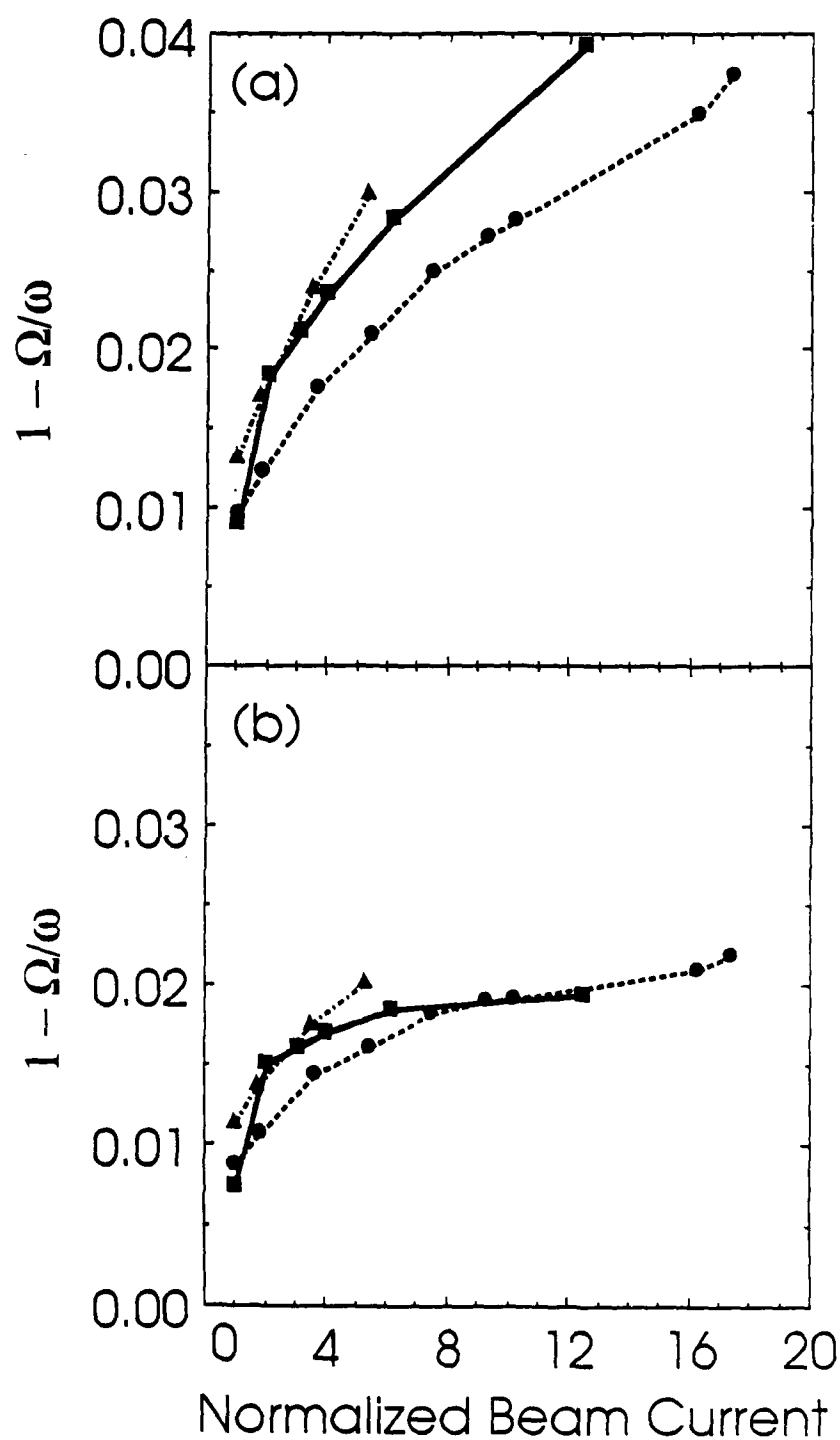


Figure 20. Resonance detuning dependence on beam current normalized to the threshold current. The detuning in (a) is uncorrected for space-charge effects; the data in (b) includes a space-charge correction. The solid dots, triangles, and squares correspond to the data shown in Figure 19.

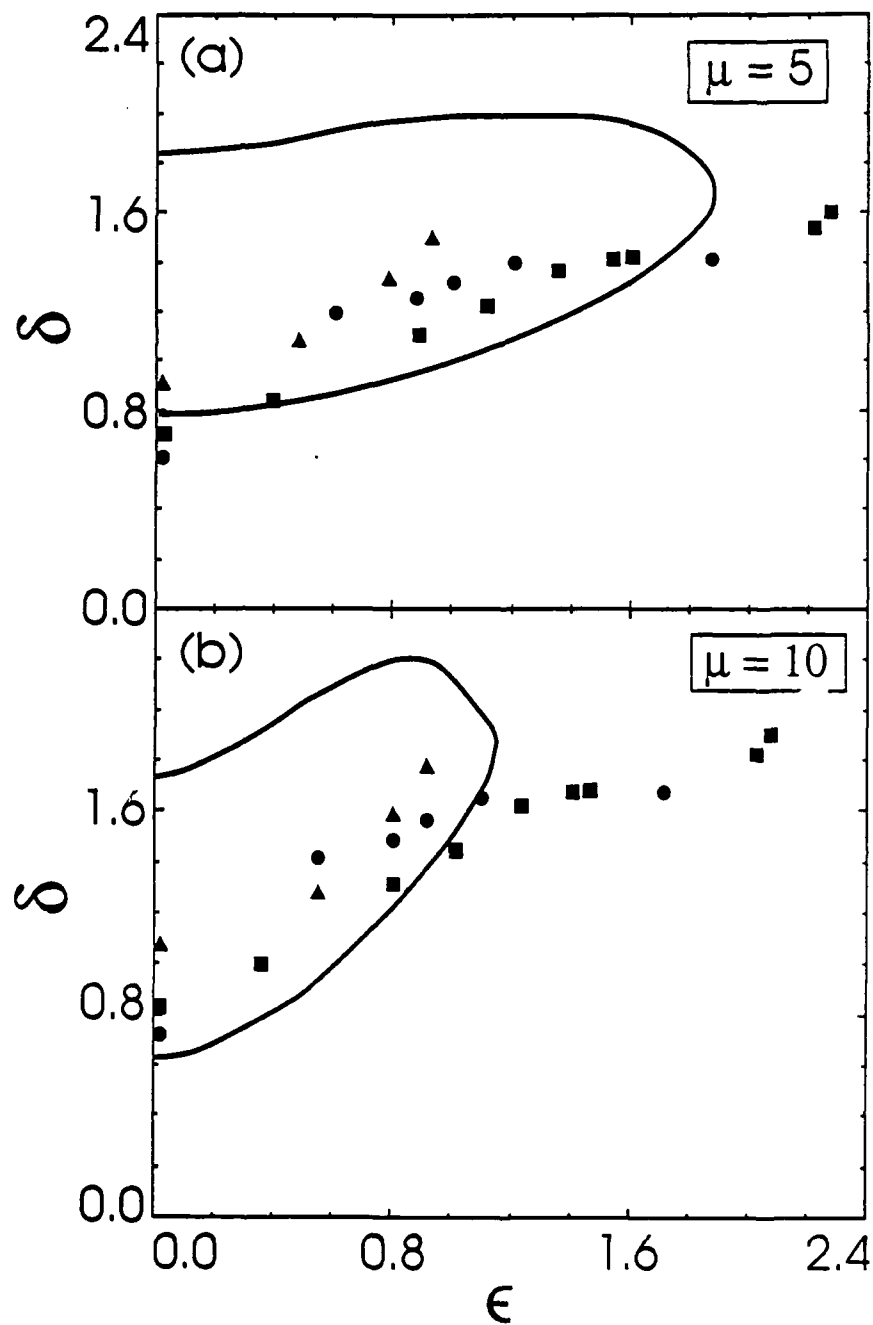


Figure 21. QOG normalized operating parameter space for (a): $\mu = 5$ ($\alpha = 0.65$) and (b): $\mu = 10$ ($\alpha = 1$). The solid dots, triangles, and squares correspond to the data shown in Figure 19. The solid curves indicate the boundary of the predicted region of stable operation.

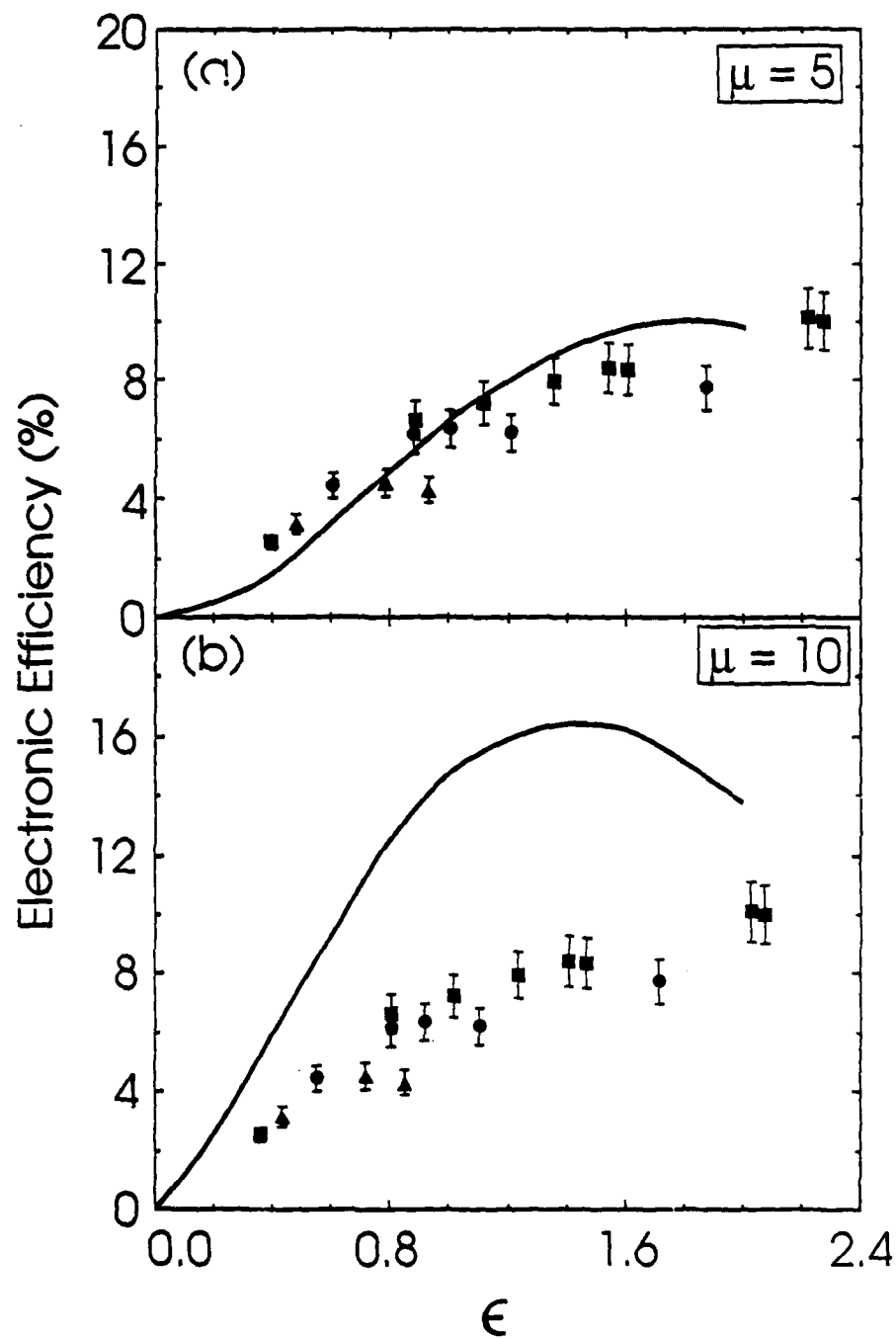


Figure 22. Comparison of theoretical and experimental electronic efficiencies for (a) $\mu = 5$ ($\alpha = 0.65$) and (b) $\mu = 10$ ($\alpha = 1$). The solid dots, triangles, and squares correspond to the data shown in Figure 19.

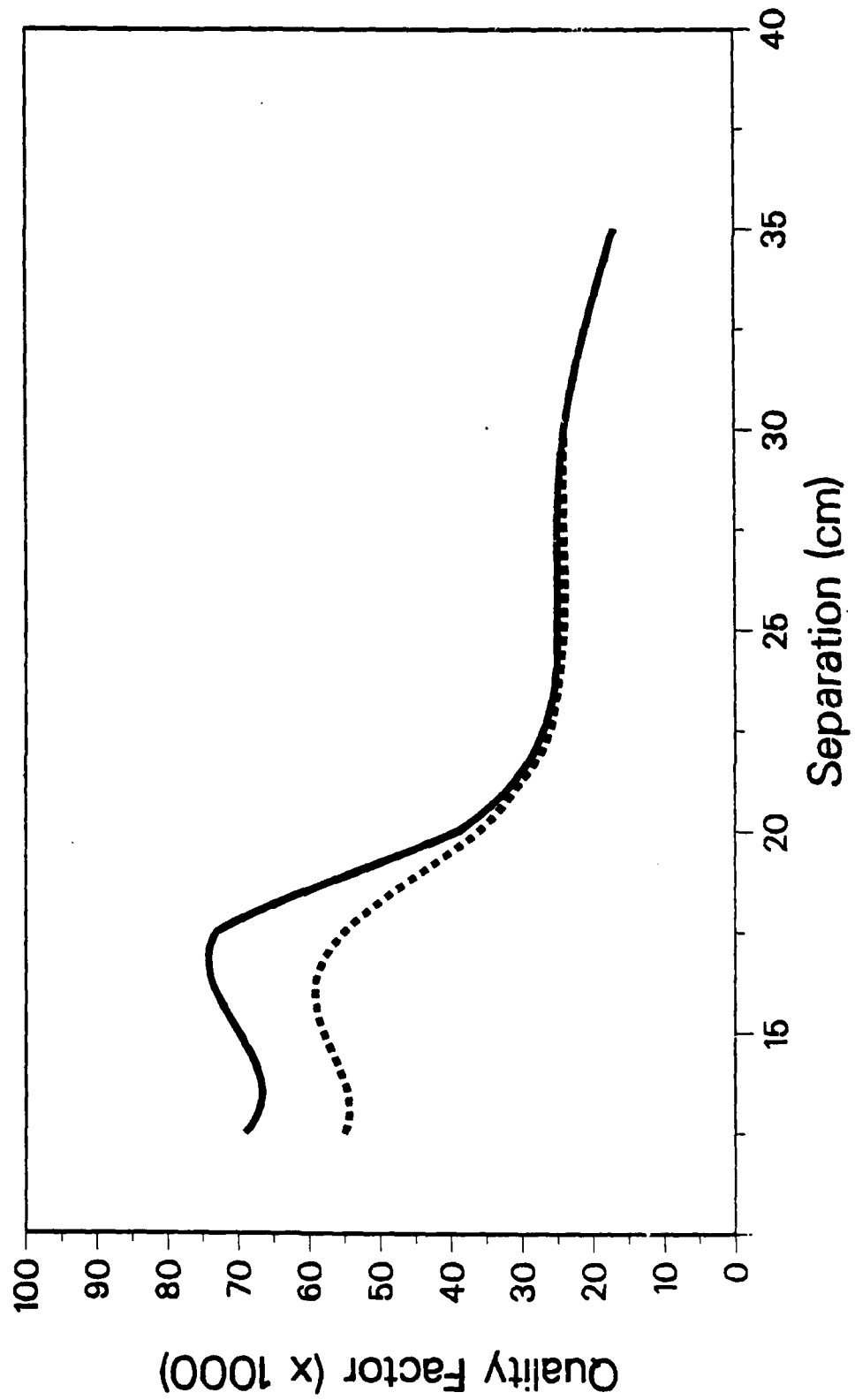


Figure 23. The calculated effect of a coupling hole on the resonator Q. The solid curve is the resonator without the hole; the dashed curve is for a resonator with a 0.76 mm diameter coupling hole (frequency = 120 GHz, mirror diameter = 4.5 cm, radius of

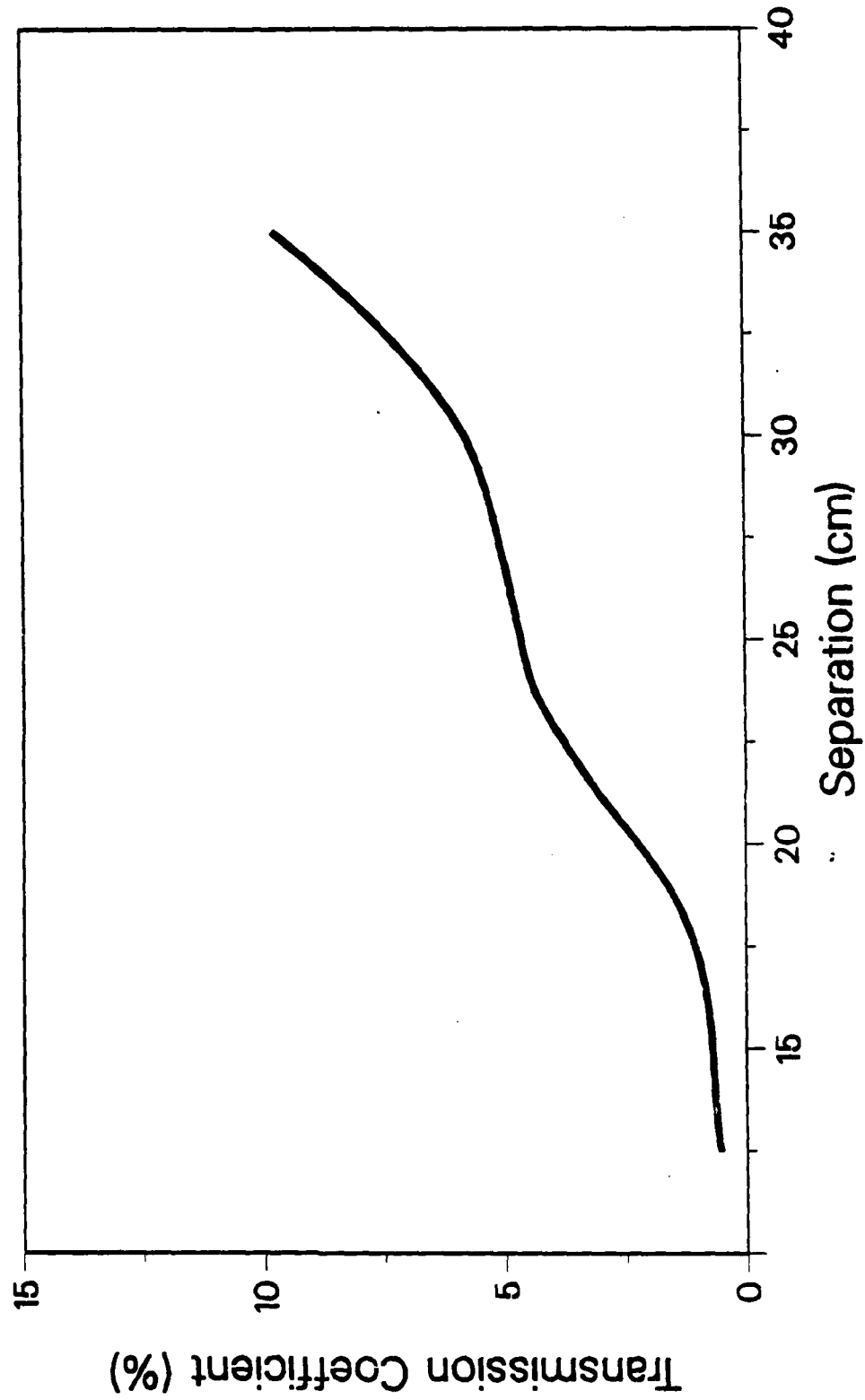


Figure 24. Round-trip transmission coefficient versus mirror separation (frequency = 120 GHz, mirror diameter = 4.5 cm, radius of curvature = 38.7 cm). The separation is typically varied between 20 and 28 cm in the QOG.

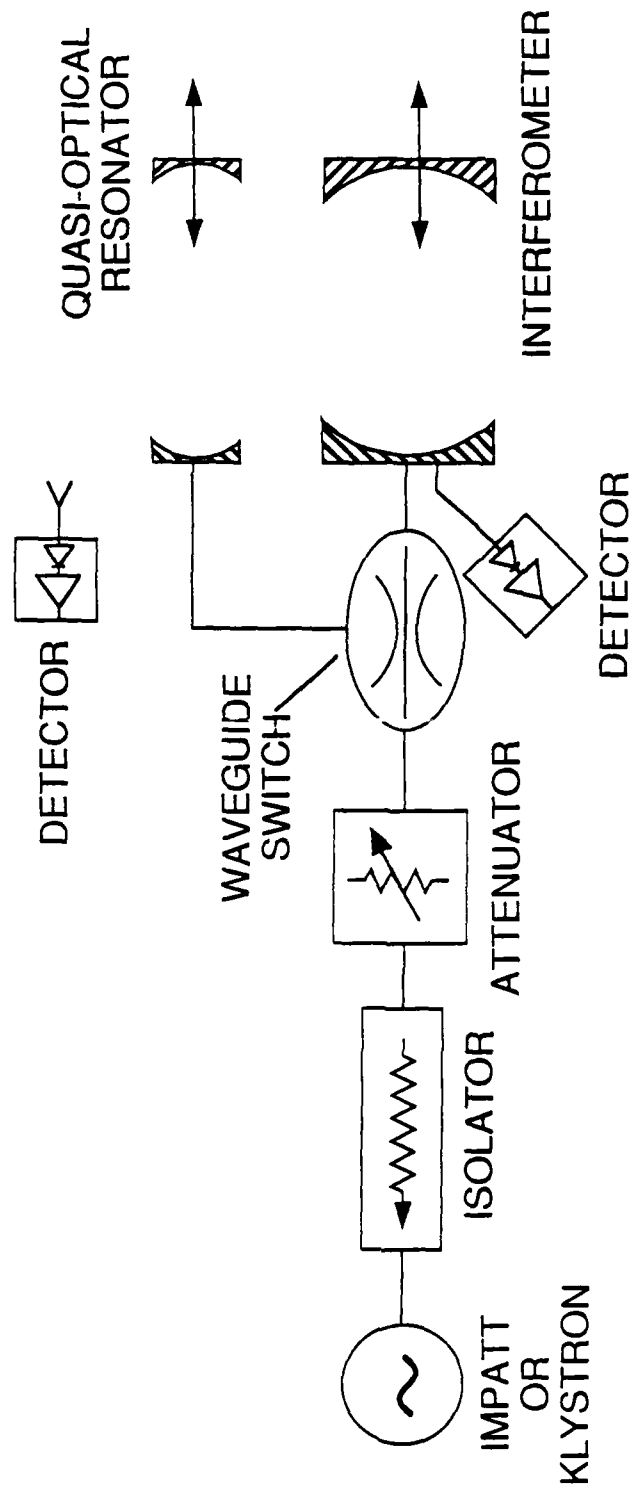


Figure 25. Schematic diagram of the cold test apparatus. Output is collected as diffraction around one of the quasi-optical mirrors.

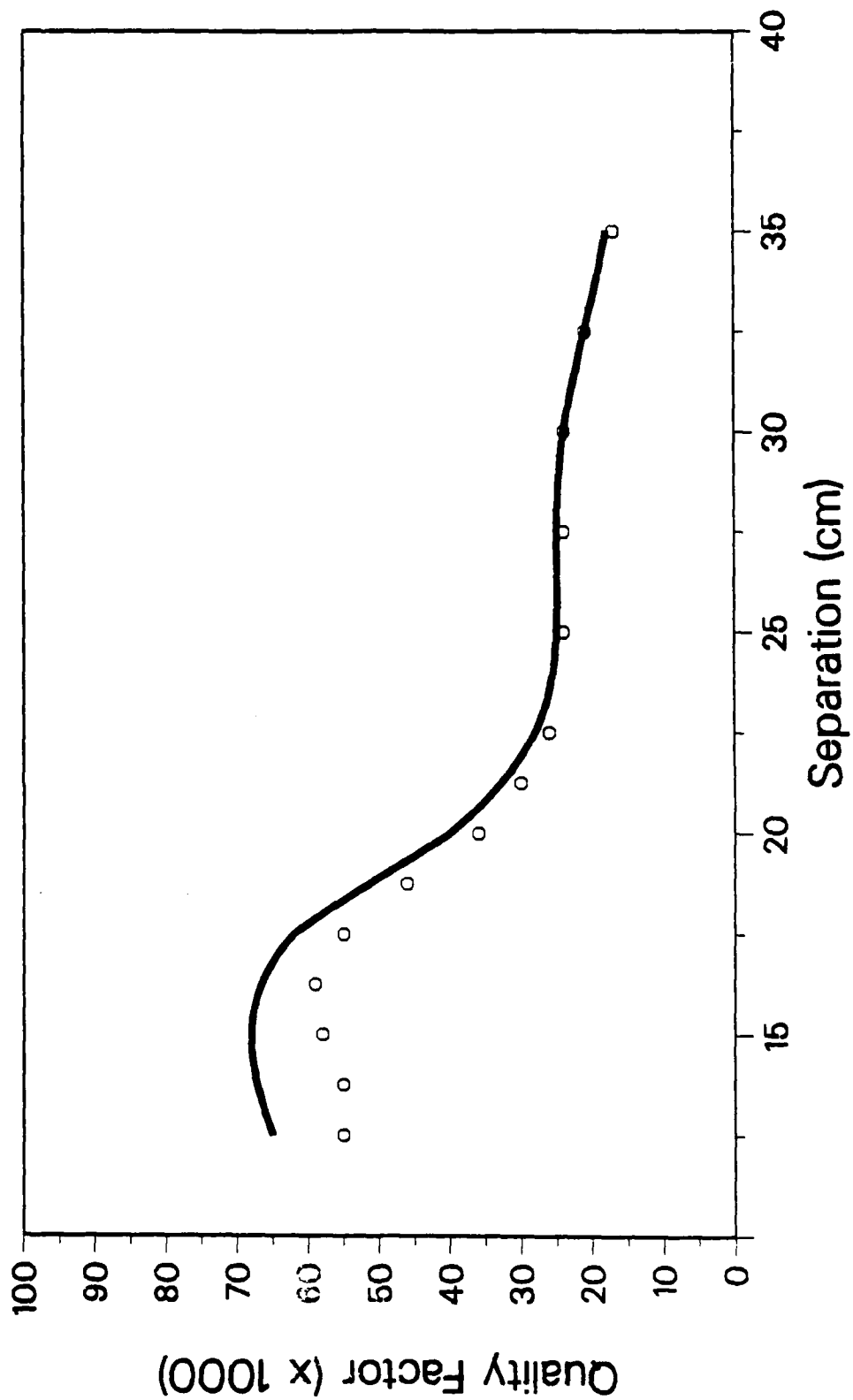


Figure 26. Measured (open dots) and theoretical values (solid curve) of resonator Q versus mirror separation (frequency ≈ 120 GHz, mirror diameter ≈ 4.5 cm, radius of curvature ≈ 38.7 cm, hole diameter ≈ 0.76 mm).

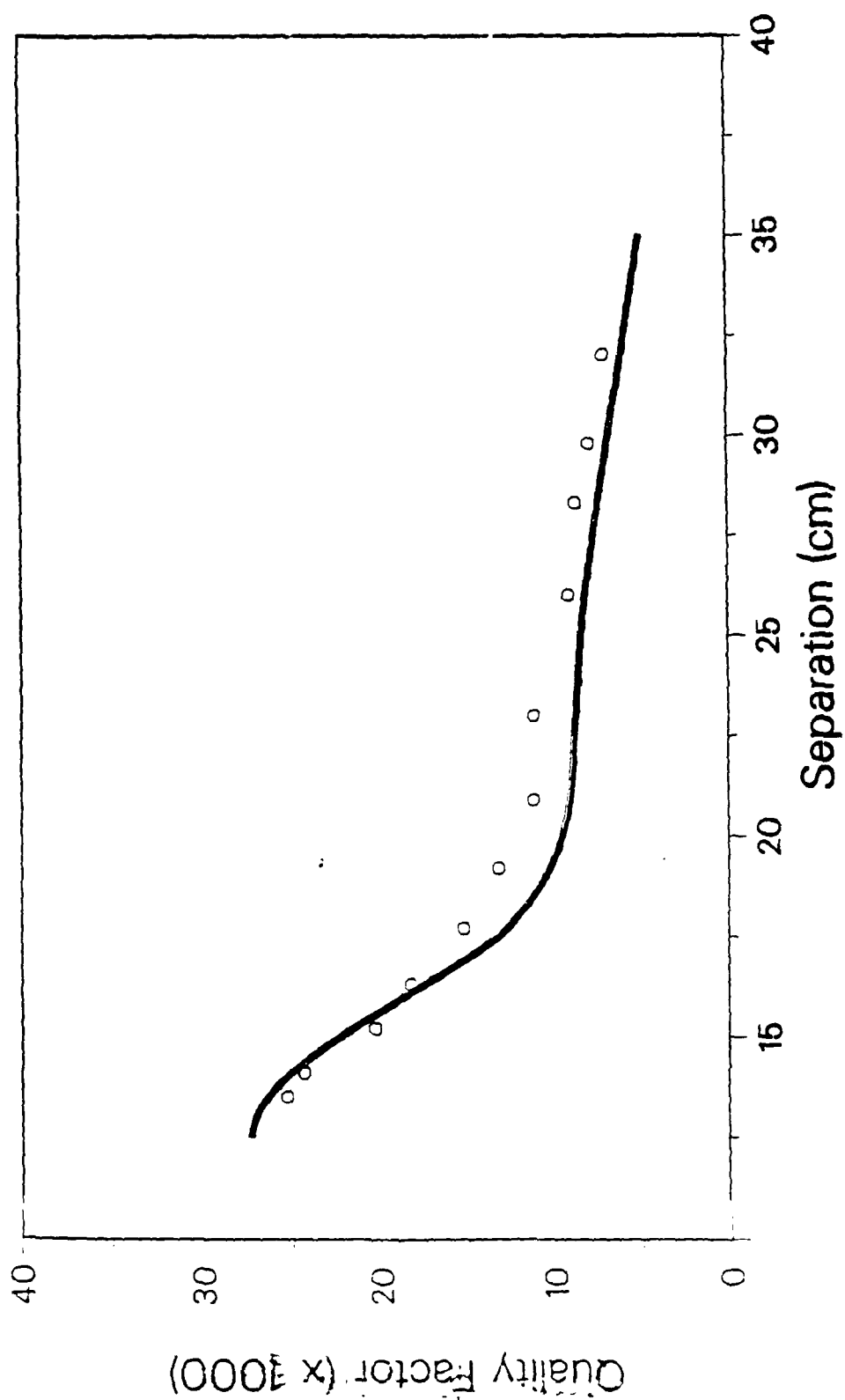


Figure 27. Measured (open dots) and theoretical values (solid curve) of resonator Q versus separation (frequency = 94 GHz, mirror diameter = 4.5 cm, radius of curvature = 38.7 cm, hole diameter = 0.76 mm).

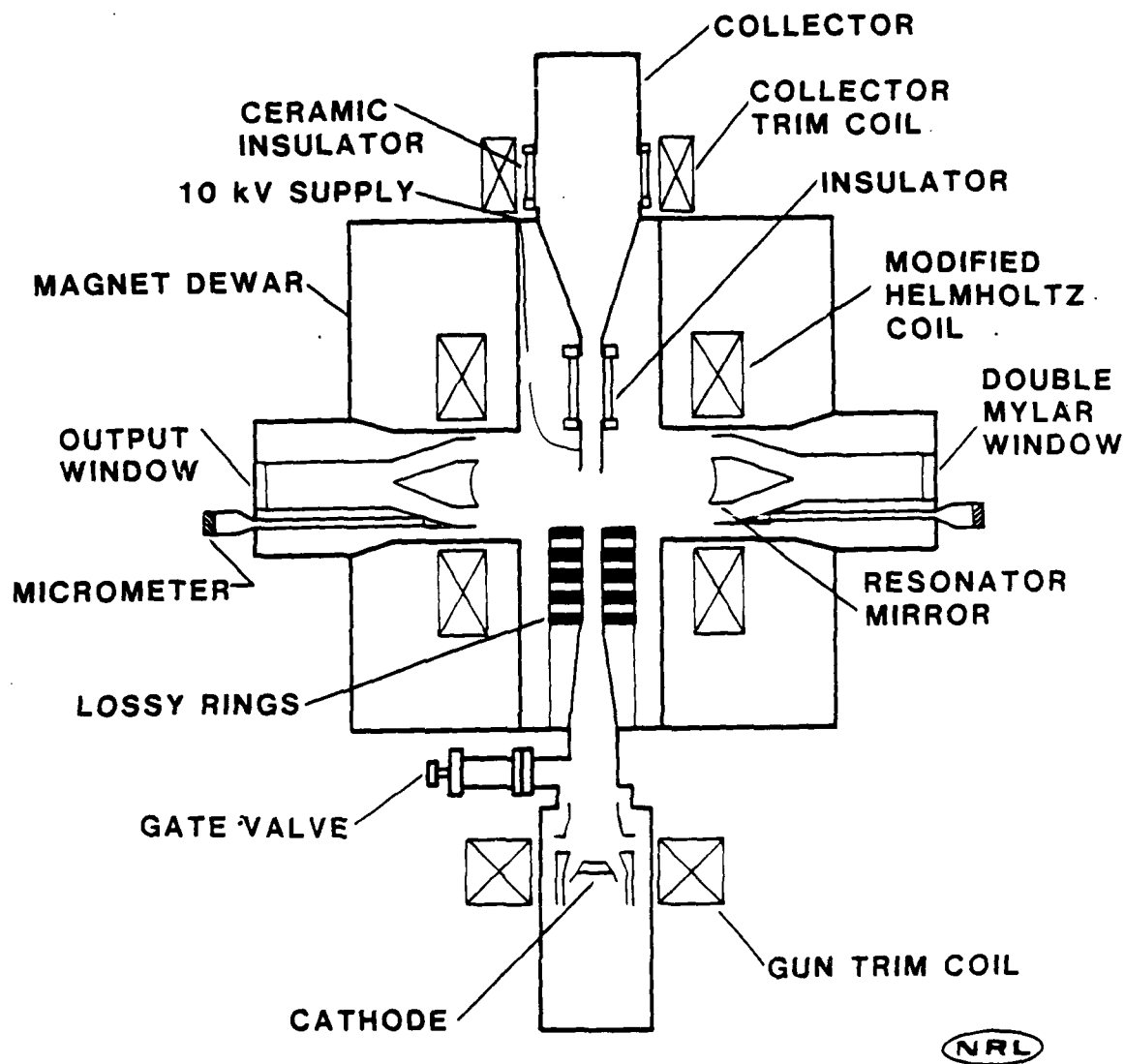


Figure 28. A schematic diagram of the 0.5-1 MW, 120 GHz QOG experiment at NRL.

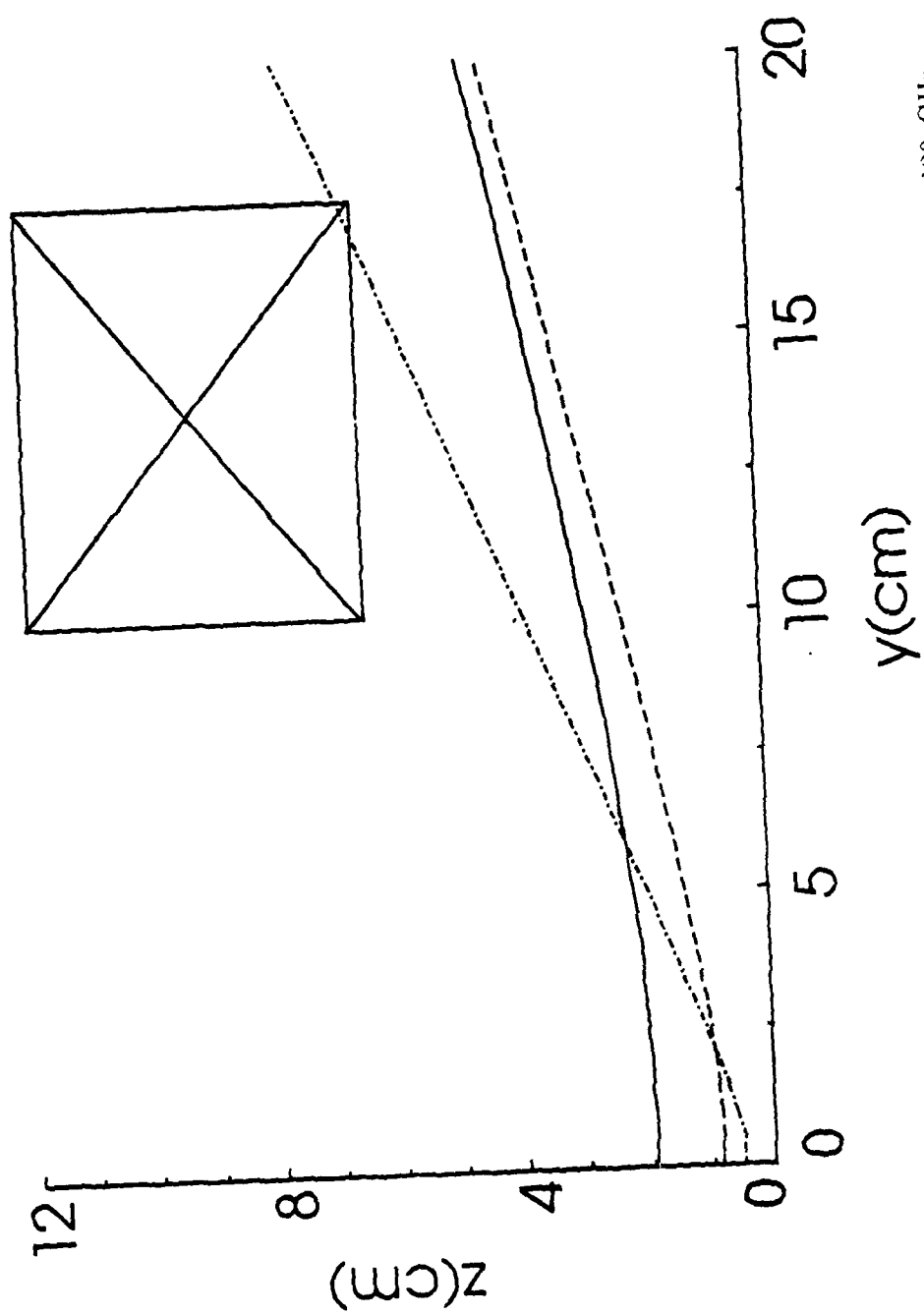


Figure 29. Curves showing the minimum crossbore radius $(3w(y))$. Solid curve: 120 GHz, $w_0/\lambda = 4.5$, dot-dashed curve: 280 GHz, $w_0/\lambda = 4.5$, dash curve: 280 GHz, $w_0/\lambda = 2.5$. The coil position of the NRL 5 T superconducting magnet is indicated by the

4793/4 DISTRIBUTION LIST

Air Force Avionics Laboratory AFWAL/AADM-1 Wright/Patterson AFB, OH 45433 Attn: Walter Friez	1 copy
Air Force Office of Scientific Research Bolling AFB Washington, D.C. 20332 Attn: H. Schlossberg	1 copy
Air Force Weapons Lab Kirkland AFB Albuquerque, NM 87117 Attn: Dr. Williar Baker Dr. A.H. Guenter	2 copies 1 copy
Bhabha Atomic Research Center Laser Division Bombay, India 400085 Attn: T.S. Shirsat	1 copy
Columbia University 520 West 120th Street Department of Electrical Engineering New York, NY 10027 Attn: Dr. S.P. Schlesinger A. Sen	1 copy 1 copy
Columbia University 520 West 120th Street Department of Applied Physics and Nuclear Engineering New York, NY 10027 Attn: T.C. Marshall R. Gross	1 copy 1 copy
Cornell University School of Applied and Engineering Physics Ithica, NY 14853 Attn: Prof. Hans H. Fleischmann John Nation R. N. Sudan	1 copy 1 copy 1 copy
Creol-FEL Research Pavillion 12424 Research Parkway, Suite 400 Orlando, FL 32826 Attn: Dr. Luis R. Elias Dr. I. Kimel	1 copy 1 copy

Dartmouth College 18 Wilder, Box 6127 Hanover, NH 03755 Attn: Dr. John E. Walsh	1 copy
Defense Advanced Research Project Agency/DEO 1400 Wilson Blvd. Arlington, VA 22209 Attn: Dr. L. Buchanan	1 copy
Defense Communications Agency Washington, D.C. 20305 Attn: Dr. Pravin C. Jain Assistant for Communications Technology	1 copy
Defense Nuclear Agency Washington, D.C. 20305 Attn: Mr. J. Farber Dr. Leon Wittwer (RAAE)	1 copy 5 copies
Defense Technical Information Center Cameron Station 5010 Duke Street Alexandria, VA 22314	2 copies
Department of Energy Div. of Advanced Energy Projects Washington, DC 20545 Attn: Dr. R. Gajewski	1 copy
Department of Energy Office of Energy Research Washington, D.C. 20545 Attn: C. Finfgeld/ER-542, GTN T.V. George/ER-531, GTN D. Crandall/ER-54, GTN Dr. David F. Sutter/ER-224, GTN	1 copy 1 copy 1 copy 1 copy
Director of Research U. S. Naval Academy Annapolis, MD 21402-5021	2 copy
General Atomics 13-260 Box 85608 San Diego, CA 92138 ATTN: Dr. J. Doane Dr. C. Moeller	1 copy 1 copy

Georgia Tech. EES-EOD Baker Building Atlanta, GA 30332 Attn: Dr. James J. Gallagher	1 copy
Hanscomb Air Force Base Stop 21, MA 01731 Attn: Lt. Rich Nielson/ESD/INK	1 copy
Hughes Aircraft Co. Electron Dynamics Division 3100 West Lomita Boulevard Torrance, CA 90509 Attn: J. Christiansen J. Tancredi	1 copy 1 copy
Hughes Research Laboratory 3011 Malibu Canyon Road Malibu, CA 90265 Attn: Dr. R. Harvey Dr. R.W. Schumacher	1 copy 1 copy
KMS Fusion, Inc. 3941 Research Park Dr. P.O. Box 1567 Ann Arbor, MI 48106 Attn: S.B. Segall	1 copy
Lawrence Berkeley Laboratory University of California 1 Cyclotron road Berkeley, CA 94720 Attn: Dr. A.M. Sessler	1 copy
Lawrence Livermore National Laboratory P.O. Box 808 Livermore, CA 94550 Attn: Dr. D. Prosnitz Dr. T.J. Orzechowski Dr. J. Chase Dr. W.A. Barletta Dr. D.L. Bix Dr. R. Briggs Dr. E.T. Scharlemann	1 copy 1 copy 1 copy 1 copy 1 copy 1 copy 1 copy
Litton Electron Devices 960 Industrial Road San Carlos, CA 94070 Attn: Library	1 copy

Los Alamos National Scientific Laboratory
P.O. Box 1663, MSJ 564
Los Alamos, NM 87545
Attn: Dr. Brian Newman 1 copy

Los Alamos Scientific Laboratory
P.O. Box 1663, AT5-827
Los Alamos, NM 87545
Attn: Dr. T.J.T. Kwan 1 copy
Dr. L. Thode 1 copy
Dr. C. Brau 1 copy
Dr. R. R. Bartsch 1 copy

Massachusetts Institute of Technology
Department of Physics
Cambridge, MA 02139
Attn: Dr. G. Bekefi/36-213 1 copy
Dr. M. Porkolab/NW 36-213 1 copy
Dr. R. Davidson/NW 16-206 1 copy
Dr. A. Bers/NW 38-260 1 copy
Dr. K. Kreischer 1 copy
Dr. B. Danby 1 copy
Dr. G.L. Johnston 1 copy

Massachusetts Institute of Technology
167 Albany St., N.W. 16-200
Cambridge, MA 02139
Attn: Dr. R. Temkin/NW 14-4107 1 copy

Mission Research Corporation
8560 Cinderbed Road, Suite 700
Newington, VA 22122
Attn: Dr. M. Bollen 1 copy
Dr. Tom Hargreaves 1 copy
Dr. J. Pasour 1 copy

Naval Research Laboratory
Addressee: Attn: Name/Code
Code 0124 - ONR 1 copy
Code 1000 - Commanding Officer 1 copy
Code 1001 - T. Coffey 1 copy
Code 1003.9A - Computer Resources Architect 1 copy
Code 1005 - Head, Office of Mgt. & Admin. 1 copy
Code 1005.1 - Deputy Head, Off. of Mgt. & Admin. 1 copy
Code 1005.6 - Head, Directives Staff 1 copy
Code 1200 - Capt. M.A. Howard 1 copy
Code 1201 - Deputy Head, Command Support Division 1 copy
Code 1220 - Security 1 copy
Code 2000 - J. Brown 1 copy
Code 2604 - NRL Historian 1 copy
Code 2628 - TID Distribution 22 copies
Code 2634 - Cindy Sims 1 copy
Code 3000 - R. Doak 1 copy

Code 4000 - W. Ellis	1 copy
Code 4000 - D. Nagel	1 copy
Code 4700 - S. Ossakow	26 copies
Code 4700.1 - A. Ali	1 copy
Code 4790 - Branch Office	25 copies
Code 4790 - W. Black	1 copy
Code 4790 - G. Cooperstein	1 copy
Code 4790 - A. Fliflet	1 copy
Code 4790 - S. Gold	1 copy
Code 4790 - C. Hui	1 copy
Code 4790 - C. Kapetanakos	1 copy
Code 4790 - A. Kinhead	1 copy
Code 4790 - Y. Lau	1 copy
Code 4790 - W. Manheimer	1 copy
Code 4790 - M. Rhinewine	1 copy
Code 4790 - P. Sprangle	1 copy
Code 5700 - L. Cosby	1 copy
Code 6840 - S. Ahn	1 copy
Code 6840 - A. Ganguly	1 copy
Code 6840 - R. Parker	1 copy
Code 6840 - N. Vanderplaats	1 copy
Code 6850 - L. Whicker	1 copy
Code 6875 - R. Wagner	1 copy

Naval Sea Systems Command
 Department of the Navy
 Washington, D.C. 20362
 Attn: Commander, PMS 405-300 1 copy

Northrop Corporation
 Defense Systems Division
 600 Hicks Rd.
 Rolling Meadows, IL 60008
 Attn: Dr. Gunter Dohler 1 copy

Oak Ridge National Laboratory
 P.O. Box Y
 Mail Stop 3
 Building 9201-2
 Oak Ridge, TN 37830
 Attn: Dr. A. England 1 copy

Office of Naval Research
 800 N. Quincy Street
 Arlington, VA 22217
 Attn: Dr. C. Roberson 1 copy

Office of Naval Research
 1012 W 36th Street, Childs Way Bldg.
 Los Angeles, CA 90089-1022
 Attn: Dr. R. Behringer 1 Copy

Optical Sciences Center University of Arizona Tucson, AZ 85721 Attn: Dr. Willis E. Lamb, Jr.	1 copy
Physical Sciences, Inc. 635 Slaters Lane #G101 Alexandria, VA 22314-1112 ATTN: Dr. M.E. Read	1 copy
Physics International 2700 Merced Street San Leandro, CA 94577 Attn: Dr. J. Benford	1 copy
Princeton Plasma Plasma Physics Laboratory James Forrestal Campus P.O. Box 451 Princeton, NJ 08544 Attn: Dr. H. Hsuan Dr. D. Ignat Dr. H. Furth Dr. P. Efthimion Dr. F. Perkins	2 copies 1 copy 1 copy 1 copy 1 copy
Raytheon Company Microwave Power Tube Division Foundry Avenue Waltham, MA 02154 Attn: N. Dionne	1 copy
Sandia National Laboratories ORG. 1231, P.O. Box 5800 Albuquerque, NM 87185 Attn: Dr. Thomas P. Wright Mr. J.E. Powell Dr. J. Hoffman Dr. W.P. Ballard Dr. C. Clark	1 copy 1 copy 1 copy 1 copy 1 copy
Science Applications, Inc. 1710 Goodridge Dr. McLean, VA 22102 Attn: Adam Drobot P. Vitello D. Bacon C. Menyuk	1 copy 1 copy 1 copy 1 copy
Science Research Laboratory 15 Ward Street Somerville, MA 02143 Attn: Dr. R. Shefer	1 copy

SPAWAR Washington, D.C. 20363 Attn: E. Warden, Code PDE 106-3113 Capt. Fontana, PMW 145	1 copy 1 copy
Spectra Technologies 2755 Northup Way Bellevue, WA 98004 Attn: Dr. J.M. Slater	1 copy
Stanford University Dept. of Electrical Engineering Stanford, CA 94305 Attn: Dr. J. Feinstein	1 copy
Stanford University High Energy Physics Laboratory Stanford, CA 94305 Attn: Dr. T.I. Smith	1 copy
Stanford University SLAC Stanford, CA 94305 Attn: Dr. Jean Labacqz	1 copy
TRW, Inc. One Space Park Redondo Beach, CA 90278 Attn: Dr. H. Boehmer Dr. T. Romisser Dr. Z. Guiragossian	1 copy 1 copy 1 copy
University of California Physics Department Irvine, CA 92717 Attn: Dr. G. Benford Dr. N. Rostoker	1 copy 1 copy
University of California Department of Physics Los Angeles, CA 90024 Attn: Dr. A.T. Lin Dr. N. Luhmann Dr. D. McDermott	1 copy 1 copy 1 copy
University of Maryland Department of Electrical Engineering College Park, MD 20742 Attn: Dr. V. L. Granatstein Dr. W. W. Destler	1 copy 1 copy

University of Maryland
Laboratory for Plasma and Fusion
Energy Studies

College Park, MD 20742

Attn: Dr. Tom Antonsen	1 copy
Dr. John Finn	1 copy
Dr. Jhan Varyan Hellman	1 copy
Dr. W. Lawson	1 copy
Dr. Baruch Levush	1 copy
Dr. Edward Ott	1 copy
Dr. M. Reiser	1 copy

University of New Mexico
Department of Physics and Astronomy
800 Yale Blvd, N.E.

Albuquerque, NM 87131

Attn: Dr. Gerald T. Moore	1 copy
---------------------------	--------

University of Tennessee
Dept. of Electrical Engr.

Knoxville, TN 37916

Attn: Dr. I. Alexeff	1 copy
----------------------	--------

University of Utah
Department of Electrical Engineering
3053 Merrill Engineering Bldg.

Salt Lake City, UT 84112

Attn: Dr. Larry Barnett	1 copy
Dr. J. Mark Baird	1 copy

U. S. Army

Harry Diamond Labs

2800 Powder Mill Road

Adelphi, MD 20783-1145

Attn: Dr. Howard Brandt	1 copy
Dr. Edward Brown	1 copy
Dr. Stuart Graybill	1 copy
Dr. A. Kehs	1 copy
Dr. J. Silverstein	1 copy

Varian Associates

611 Hansen Way

Palo Alto, CA 94303

Attn: Dr. H. Huey	1 copy
Dr. H. Jory	1 copy
Dr. Kevin Felch	1 copy
Dr. R. Pendleton	1 copy
Dr. A. Salop	1 copy

Varian Eimac San Carlos Division

301 Industrial Way

San Carlos, CA 94070

Attn: C. Marshall Loring	1 copy
--------------------------	--------

WL/CA
Kirtland AFB, NM 87117-6008
Attn: Mr. Brendan B. Godfrey

1 copy

Yale University
Applied Physics
Madison Lab
P.O. Box 2159
Yale Station
New Haven, CN 06520
Attn: Dr. I. Bernstein

1 copy

Ken Busby

1 copy

Naval Research Laboratory
Washington, DC 20375-5000
Code 2630
Timothy Calderwood